SANDIA REPORT

SAND2004-4791
Unlimited Release
Printed September 2004

High Fidelity Frictional Models for MEMS

E. D. Reedy, Jr., M. P. de Boer, A. D. Corwin, M. J. Starr, F. Bitsie, H. Sumali, J. M. Redmond, R. E. Jones, B. R. Antoun, G. Subhash, R. W. Carpick, E. E. Flater, M. D. Street, W. R. Ashurst

Prepared by
Sandia National Laboratories
Albuquerque, New Mexico 87185 and Livermore, California 94550

Sandia is a multiprogram laboratory operated by Sandia Corporation,
a Lockheed Martin Company, for the United States Department of Energy's
National Nuclear Security Administration under Contract DE-AC04-94AL85000.

Issued by Sandia National Laboratories, operated for the United States Department of Energy by Sandia Corporation.

Available to DOE and DOE contractors from
U.S. Department of Energy
Office of Scientific and Technical Information
P.O. Box 62
Oak Ridge, TN 37831

Telephone: (865)576-8401
Facsimile: (865)576-5728
E-Mail: reports@adonis.osti.gov
Online ordering: http://www.doe.gov/bridge

Available to the public from
U.S. Department of Commerce
National Technical Information Service
5285 Port Royal Rd
Springfield, VA 22161

Telephone: (800)553-6847
Facsimile: (703)605-6900
E-Mail: orders@ntis.fedworld.gov
Online order: http://www.ntis.gov/help/ordermethods.asp?loc=7-4-0#online

High Fidelity Frictional Models for MEMS

E. D. Reedy, Jr.
Materials Mechanics Department

M. P. de Boer and A. D. Corwin
Radiation and Reliability Physics Department

M. J. Starr, F. Bitsie, H. Sumali, and J. M. Redmond
Structural Dynamics Research Department

R. E. Jones
Science-Based Materials Modeling Department

B. R. Antoun
Microsystems and Materials Mechanics Department

Sandia National Laboratories
P. O. Box 5800
Albuquerque, NM 87185-0893

G. Subhash
Michigan Technological Institute
Houghton, MI 49931

R. W. Carpick, E. E. Flater, and M. D. Street
University of Wisconsin
Madison, WI 53706-1609

W. R. Ashurst
Auburn University
Auburn, Alabama 36849

SAND2004-4791
Unlimited Release
Printed October 2004

Abstract

The primary goals of the present study are to: 1) determine how and why MEMS-scale friction differs from friction on the macro-scale, and 2) to begin to develop a capability to perform finite element simulations of MEMS materials and components that accurately predicts response in the presence of adhesion and friction.

Regarding the first goal, a newly developed nanotractor actuator was used to measure friction between molecular monolayer-coated, polysilicon surfaces. Amontons' law does indeed apply over a wide range of forces. However, at low loads, which are of relevance to MEMS, there is an important adhesive contribution to the normal load that cannot be neglected. More importantly, we found that at short sliding distances, the concept of a coefficient of friction is not relevant; rather, one must invoke the notion of "pre-sliding tangential deflections" (PSTD). Results of a simple 2-D model suggests that PSTD is a cascade of small-scale slips with a roughly constant number of contacts equilibrating the applied normal load.

Regarding the second goal, an Adhesion Model and a Junction Model have been implemented in PRESTO, Sandia's transient dynamics, finite element code to enable asperity-level simulations. The Junction Model includes a tangential shear traction that opposes the relative tangential motion of contacting surfaces. An atomic force microscope (AFM)-based method was used to measure nano-scale, single asperity friction forces as a function of normal force. This data is used to determine Junction Model parameters. An illustrative simulation demonstrates the use of the Junction Model in conjunction with a mesh generated directly from an atomic force microscope (AFM) image to directly predict frictional response of a sliding asperity.

Also with regards to the second goal, grid-level, homogenized models were studied. One would like to perform a finite element analysis of a MEMS component assuming nominally flat surfaces and to include the effect of roughness in such an analysis by using a homogenized contact and friction models. AFM measurements were made to determine statistical information on polysilicon surfaces with different roughnesses, and this data was used as input to a homogenized, multi-asperity contact model (the classical Greenwood and Williamson model). Extensions of the Greenwood and Williamson model are also discussed: one incorporates the effect of adhesion while the other modifies the theory so that it applies to the case of relatively few contacting asperities.

1. Introduction

Microelectromechanical systems (MEMS) technology utilizes efficient fabrication techniques to produce cost effective components with enhanced performance and functionality. Allowing contact between MEMS surfaces significantly broadens the design space to include components with gears, guides, linear racks, pin-in-maze, etc. Indeed, polysilicon MEMS are being considered for demanding applications at Sandia that involve contacting and sliding surfaces. Examples include microengines, nanotractor actuators, nonvolatile memories, discriminating microswitches, and microrelays. The performance and reliability of such MEMS devices depend on understanding and controlling contact and frictional interactions between the asperities found on polysilicon surfaces. The primary goals of the present study are to: 1) determine how MEMS-scale friction differs from friction on the macro-scale, and 2) to begin to develop a capability to perform finite element simulations of MEMS materials and components that accurately predicts response in the presence of adhesion and friction. The development of predictive modeling capability will help enable the cost-effective development of new applications of polysilicon MEMS.

There are three major elements in this study. The first element is to measure friction between polysilicon surfaces on the MEMS-scale (*i.e.*, micron-scale). In particular, we wanted to measure friction on typical self-assembled monolayer (SAM)-coated polysilicon surfaces since such protective and lubricating coatings are usually applied to the surfaces of MEMS components. We anticipated that in at least some circumstances MEMS-scale friction would differ from that found on the macro-scale. On the micron scale, there could be relatively few contacting asperities compared to the large number of contacting asperities that generate frictional behavior on the macro-scale. Furthermore, adhesion between contacting surfaces can become important on the micron-scale. To make these measurements, we used a newly developed nanotractor actuator as a MEMS-scale friction tester. This device is distinguished by its ability to generate both very low and very high forces in both the tangential and normal directions. Increasingly sensitive metrology was developed during the course of this work, with an ultimate, Moiré-based capability to measure in-plane displacements with an accuracy of ±1 nm. This capability enabled us to discover an entirely new phenomenon that cannot be described by a classical coefficient of friction (Pre-sliding Tangential Deflections, Section 2.1.7-2.1.9).

The second major element of this study was the development of an initial capability to perform asperity-level finite element simulations. An Adhesion Model and a Junction Model were implemented in PRESTO, Sandia's transient dynamics, finite element code. The Junction Model enhances the Adhesion Model with a tangential-velocity dependent, shear traction (junction strength) that opposes the relative tangential motion of the surfaces when they are in contact. An AFM-based method was used to measure nano-scale, single asperity friction forces as a function of normal force. This data, in conjunction with detailed finite element analysis of the contact response of SAM-coated surfaces, can be used to determine Junction Model parameters. The ultimate goal is to perform asperity-level simulations that include all the relevant physics while using a mesh generated directly from an atomic force microscope (AFM) image to produce a

detailed description of surface topography. Such simulations would directly predict friction forces. This capability can also provide a more fundamental understanding of the effect of surface coatings on asperity contact and frictional forces and the origin and mechanisms of wear in contacting and sliding polysilicon surfaces.

The final element of this study is to develop homogenized, grid-scale models for contacting and sliding polysilicon surfaces. One would like to perform a finite element analysis of a component assuming nominally flat surfaces. The goal is to include the effect of roughness in such an analysis by using homogenized contact and friction models that depend on only on a few input parameters. AFM measurements were made to determine statistical information on the distribution of asperity summits, density of summits, and average radius of curvature of summits for polysilicon surfaces with different roughness. This type of information is used in homogenized models like the classical Greenwood and Williamson model (see section 4.3). Extensions of the Greenwood and Williamson model are also discussed: one incorporates the effect of adhesion while the other modifies the theory so that it applies to the case of relatively few contacting asperities.

Some of the work described in this report has been previously published in journal and conference proceedings papers. Citations for these papers are listed in Appendix A.

2. MEMS-scale Friction

2.1 Nanotractor device description and test methods and results

2.1.1 Background

As recently summarized by Gao and coworkers [2.1], early studies of friction include the work of da Vinci (1452-1519), Amontons (1663-1706) and Coulomb (1736-1806). They observed empirically that the friction force between two surfaces is proportional to normal force, i.e.,

$$\mu = \frac{\text{tangential (friction) force}}{\text{normal (externally applied) load}} = \frac{F_T}{F_N}, \qquad (2.1)$$

and this is often called Amontons' Law. They also noted that the friction force is independent of the area and they distinguished between static and dynamic coefficients of friction. Coulomb observed that the static friction can increase logarithmically with time, but that the dynamic coefficient is independent of velocity. Today, it is well known that these "laws" are not valid if the force or velocity is extended over a sufficiently wide range, or if the nominal and real contacting areas are the same (as in friction force microscopy or surface force apparatus measurements). However, because of its simplicity and because it is a surprisingly good description over a broad range of contact

parameters, many mechanics models of friction include only static and dynamic coefficients.

One goal of this work was to determine the laws of friction for MEMS surfaces. This work was enabled by the use of a newly developed nanotractor actuator as a friction test structure. Experimentally, we found that Amontons' law does indeed apply over a wide force range. As might be expected, we also found that dynamic friction is lower than static friction. However, at low loads, which are of relevance to MEMS, there is an important adhesive contribution to the normal load that cannot be neglected. Also, we found that at short sliding distances, the concept of a coefficient of friction is not relevant; rather, one must invoke the notion of "pre-sliding tangential deflections" (PSTD). In the following sections, we will discuss the high-performance characteristics of the nanotractor actuator, its use as a model friction test structure, advanced metrology methods we developed to measure both static and dynamic friction, new software for automated MEMS metrology, the importance of PSTD in describing the detailed nanotractor operation, detailed measurements of PSTD and studies of wear of polysilicon surfaces using the nanotractor.

2.1.2 Device Description

Accurately measuring friction over a wide pressure and velocity range in MEMS is a non-trivial task. This is because conventional MEMS actuators, such as comb drives, develop a small force of about 10 μN. Furthermore, spring forces act in series with the friction force, and are difficult to calibrate. Because the friction force measured with conventional MEMS test structures is a difference of two small numbers, calibration errors can result. Also, because of the low force, the study of the coefficient of friction, μ, can be made only over a small force range.

A recently-developed MEMS actuator called the "nanotractor" takes advantage of friction to realize a high-performance bidirectional linear actuator. It delivers up to 2.5 mN of force (250 times more than a conventional comb drive), can travel from 0 to 4 mm/second, has a ± 100 μm range and is capable of high-precision positioning (40 nm). See ref. [2.2] for a detailed description of this device. The nanotractor was also designed with a mind towards measuring friction over a wide normal force and velocity range in MEMS. However, it had not yet been proven to be sensitive to friction at the beginning of the study. Our early work showed that the nanotractor coefficient of friction is sensitive to different monolayer coatings and can be used to study MEMS friction over a wide normal force range. Hence, the first major experimental result of the project was that the nanotractor serves as an improved MEMS friction test structure.

The nanotractor design principle is as follows. An electrostatically actuated plate of length L_P spans friction clamps of length L_c. For actuation, the plate deflects out-of-plane with an amplitude A to induce in-plane motion, as seen in Fig. 2.1. The normal force that is applied to deflect the plate generates a tangential force that is approximately a factor of 10 higher. Signals to the leading and trailing clamps and to the actuation plate

must be phased to achieve motion, as shown in Fig. 2.2. One such cycle results in a 40 nm step, which can be repeated over and over for large travel distances. With appropriate sequencing, forward or reverse motion of up to ± 100 μm is achieved. An SEM of the nanotractor is shown in Fig. 2.3. The reader will note that it is attached to Load Springs A and B. Load Spring A is a weak linear load spring that serves to keep the nanotractor on its track, while Load Spring B is a strong non-linear load spring used for friction testing. Also, note the displacement gauge, which will be discussed below.

A cross-sectional schematic of the nanotractor friction clamps, through the dotted line YY- indicated in Fig. 2.3, is shown in Fig. 2.4. The clamps are on each side of the actuation plate and consist of two sections. At the center of each clamp is a friction foot, which bears both normal and tangential loads. The clamp, the friction foot and the friction foot counterface are electrically grounded. Clamp electrodes adjacent to each friction clamp attract the clamp "wings" to generate normal force. During locomotion, a voltage of typically 150 V is sequentially applied to the clamps to "lock" them in place. If the clamps are of length L_c=200 um, this results in a normal force of ~2 mN. If the clamps are L_c=600 μm long, a force of ~6 mN is generated. Figure 2.4(b) shows a cross-sectional SEM of an actual nanotractor clamp, and a close-up of the friction foot is shown in Fig. 2.4(c). It should be noted that the foot is not quite flat. However, the foot can and has been made nominally flat in a subsequent design. The friction counterfaces are not atomically smooth but reflect the roughness of the polysilicon surfaces, which ranges from 2 to 10 nm root mean square (rms), depending on the processing lot. The real contact areas are estimated to be several orders of magnitude below the apparent contact areas.

2.1.3 Static Friction and Adhesion Force Measurement and Results

During locomotion as described in the previous section, the nanotractor works against a load spring. It may be attached to Load Spring A only, or it may be attached to Load Springs A and B. In the latter case, the effect of Load Spring A on the total load is insignificant. Load Spring B is useful for measuring μ over a wide normal force range, while Load Spring A is useful for quantifying the effect of adhesion on friction and also in making dynamic friction measurements.

A static friction measurement is schematically represented in Fig. 2.5. To carry out a static friction test we first walk the nanotractor out against the suspension spring to some large distance, say 10 to 50 μm. We then clamp the leading clamp with a large voltage (i.e., a large normal force), and release the trailing clamp and actuation plate. This locks the device in position. We now step down the force in the leading clamp while recording the position of the nanotractor. In this configuration, applied normal forces ranging from 1 μN (V_c=1.9 V, L_c=600 μm) to 10.6 mN (V_c=200 V, L_c=600 μm) are possible. (These loads are calculated from a simple parallel plate law and the fringing field is assumed to be negligible). As long as the frictional force generated at the clamp is large enough to hold off the tangential force of the load spring, we expect the nanotractor to remain in

place. We expect the static friction force to be surmounted and for the nanotractor to start sliding when the frictional force just drops below the tangential force.

Figure 2.6 shows the results of a measurement of position as a function of normal force for a nanotractor coated with FOTAS, an 8-carbon chain monolayer lubricant [2.3]. As the data in Fig. 2.6 is from a nanotractor attached to Load Spring A with a linear in-plane spring constant calculated to be 4.5 N/m [2.4], the position data is directly related to the tangential force. We observe that the nanotractor remains fixed in position until the normal force is sufficiently low that a jump occurs. At that point, the tangential force exactly balances the frictional force, and we can infer a coefficient of static friction, μ_s. From Fig. 2.6, each point just before a jump can be fit to a modified version of Amontons' Law if we include a surface attraction term (F_{adh}),

$$F_s = \mu_s F_N + \mu_s F_{adh} \tag{2.2}$$

Here, the applied normal force F_N includes not only the clamping force F_c due to voltage loading but also an out-of-plane restoring force from the suspension spring ($k_z z$) and a gravitational mass term (mg), i.e.,

$$F_N = F_c + mg - k_z z \tag{2.3}$$

Thus, we can determine both the coefficient of static friction and the contribution of adhesion. For this coating we find a static coefficient of friction of 0.31 ± 0.01 (from the slope), and an adhesion force of 1nN/μm^2 (from the non-zero y-axis intercept). More details on the static friction technique can be found in [2.2] and [2.5].

The friction coefficient itself depends on many factors. These include, but are not limited to, the type of lubricant, the velocity, the environment, the surface roughness and the history of the surfaces (i.e., wear). One of the strongest factors is the monolayer lubricant, whose structure is described in more detail in Appendix C. In Fig. 2.7, we show that the static friction depends strongly on the lubricant. The different monolayers in Fig. 2.7 are an 18-carbon chain octyldecyltrichlorosilane ($CH_3(CH_2)_{17}SiCl_3$, OTS) [2.6], an 18-carbon chain octadecene ($C_{16}H_{33}CH{=}CH_2$, 1-octadecene) [2.7] and a branched single-carbon chain dichlorodimethylsilane (DDMS) [2.8] which was applied in the vapor phase following critical point drying [2.9, 2.10]. The fourth treatment was critical point drying, followed by exposure to a three watt, downstream oxygen plasma, which generates a clean, thin oxide surface. These coatings were chosen because of the range of friction coefficient previously measured using a beam-on-post configuration (from 0.1 to 1.0) [2.7, 2.8], and because of their demonstrated compatibility with surface micromachining. By calculating the load-displacement characteristic of Load Spring B and knowing the normal load, the friction force can be determined. The data in Fig. 2.7 was taken using Load Spring B and therefore the static friction was tested over a wide force range. The data from the OTS and DDMS-coated devices is recast versus load in Fig. 2.8 and it is observed that the coefficient of friction does not show a strong dependence on normal

force, in agreement with Amontons' Law. This is the first time this law has been shown to be valid over such a wide force range (factor of 30) in MEMS.

2.1.4 Metrology

The data in Figs. 2.7 and 2.8 was taken using optical magnification of the displacement gauge and was limited by human vision to ~0.5 μm resolution. On the other hand, the data shown in Fig. 2.6 was taken at a later time after we had applied a machine-based image analysis routine using sub-pixel resolution. This gave us approximately ±10 nm resolution of in-plane (tangential) displacement, with a marked corresponding improvement in force resolution. We have also more recently developed an optical Moiré metrology that gives us approximately ±1 nm resolution [2.11]. In this latter case, a grating of 2.5 μm-pitch is directly attached to the nanotractor clamps, and its phase is measured to 1 part in 4000. In fact, in Fig. 2.6, both the sub-pixel and the Moiré are simultaneously used. This averts a problem with the Moiré - although it gives very high resolution, it has a phase problem in that increments of 2.5 μm cannot be distinguished. Hence, by using a combination of the two techniques, we maintain a metrology with ±1 nm resolution over a ±30 μm range.

Another important metrology innovation we made in this work is to develop a computer-based MEMS actuation scripting language, now entitled "MEMScript" [2.12]. As schematically represented in Fig. 2.9a, MEMScript integrates application of voltages (to MEMS actuators and metrology tools), image analysis, and decision making to make a powerful testing platform for MEMS. It also automates data analysis

The use of MEMScript enabled us to overcome one initial limitation in the friction testing. Namely, in the data of Figs. 2.7 and 2.8, we reduced the voltage by 5 V intervals because of software limitations we had when that data was taken. As the normal force is proportional to the square of the clamping voltage (V_c^2) this made for a fairly large uncertainty in μ_s especially at low force levels, and this likely is the reason for the large scatter in the data in Fig. 2.7 and 2.8. With MEMScript, the voltage is reduced by much smaller intervals -- on the order of 100 mV. Using this automated data-taking method, we can infer that μ_s is independent of normal load all the way down to 1 μN. Hence, it appears that μ_s describes MEMS friction over a very wide force range (from 1 μN to 1 mN), as long as we take the adhesive force into account. (More data is currently being taken on a recently processed experiment to determine how far this range extends).

As part of the project, we also constructed a high-resolution probe station to minimize vibration noise in our experiments, as shown in Fig. 2.9b. This probe station microscope was built with rigid supports and without any motorized control (unlike commercial probe stations). It also incorporates long-working distance interferometry so that simultaneous nanometer-scale measurements are possible in three dimensions. A distinct advantage of the construction is that because of our familiarity with it, we can trace and replace components that may be causing measurement distortions. For example, one

issue with the Moiré technique we have found is that it is sensitive to focus control. If focus drifts, the resolution is compromised. This issue limits resolution when we are looking for frictional creep on the order of minutes. The problem has been traced to thermal expansion of the aluminum support rails in our test system and we are looking to actively control their temperature.

2.1.5 Calibration of Load Springs

One important advantage of the nanotractor friction test methodology over conventional MEMS friction testing is that the force during the friction measurement is supplied only by the loaded spring, and not also by an actuator. Therefore, obtaining accurate tangential force information requires knowing only the spring characteristics and the spring displacement. In this section, we discuss methods to calibrate the load springs.

We have two basic nanotractor device types that we work with: those with linear suspension springs, and those with linear suspension springs plus a strong non-linear load cell. The linear suspension springs offer two independent methods of calibration, and are described first. We started by calculating the spring constant of the folded suspension based on the known geometry, nominal line width (2 μm), and assumed Young's modulus for polysilicon (164.8 GPa). With these values we calculated a spring constant of 0.55 N/m. We improved this computation by using a focused ion beam (FIB) to make a cross section cut through the suspension spring. This allowed us to use actual values for line widths (typically about 1.8 μm) instead of assuming the nominal process value. With this measured line width value we calculated the spring constant to be 0.40 N/m.

Because of our ability to make true time dependent measurements (see dynamic friction section 2.1.6), we were also able to directly measure the resonant frequency of the nanotractor. The resonant frequency is related to both the mass, m, and the spring constant, k, as

$$\omega = \sqrt{k/m} \tag{2.4}$$

We can estimate the mass of the nanotractor from the AutoCAD design files and assuming the density of polysilicon is 2300 kg/m^3, i.e., the same as silicon. Since the largest contribution of mass is from large continuous volumes of material, the uncertainty due to line-width variations is relatively small. Thus, a variation in nanotractor mass between lots is expected to be small. We estimate the nanotractor mass to be 2.25 ± 0.15 nanograms. Typical resonant frequencies are about 13000 rad/sec. yielding k=0.38 ± 0.03 N/m. Given the uncertainties, this is in good agreement with the analytic calculation. Because the analytical calculation of spring constant is sensitive to lot-to-lot line width variations, we fixed our calibration using the resonant frequency and the assumed nanotractor mass. As long as variation in mass between lots is small (which is what we expect), the relative values of the spring constant should be fairly accurate. Even if our mass estimate is systematically high for all devices, we will end up with only a shift in all

spring constants. That is, relative values of μ_s and μ_d between different lots are can be compared very well if the mass of the nanotractor is consistent from lot-to-lot.

Calibration of the non-linear load cell is done solely by an analytic calculation based on geometry, Young's modulus, and line width. However, the line widths are larger for this load cell, and thus less sensitive to process variations. If we assume that devices with the non-linear load cell should yield the same value of friction as a linear-suspension only device located on the same module, we can test the goodness of our non-linear load cell calibration. We find good agreement between the two load cell types, demonstrating that we have a good non-linear load cell calibration.

2.1.6 True Dynamic Friction Measurement

One technique for obtaining the dynamic friction coefficient in MEMS is to use the data at the stopping point after a static friction event. Two methods of analysis have been used by other MEMS researchers. In one, the energy dissipated (the difference in the spring potential energy) is equated to the dynamic friction force times the distance traveled. In the second, a simple force balance at the point of stopping is assumed. Although reasonable values result, the methods are not completely satisfying because neither inertia nor air damping is taken into account in the analysis methods.

We also developed a method to obtain a true dynamic coefficient of friction. To do this, we realized an experimental configuration in which a 1-D mechanical oscillator was subject to friction, air damping and inertial forces. By measuring the position of the nanotractor at some 50 points per oscillation cycle, and by comparing the data to the 1-D oscillator equation, we could quantify the friction as well as the air damping. Using the linear Load Spring A, such data and results are shown in Fig. 2.10 for the case of zero applied voltage. Considering that Load Spring A also imparts a small negative normal force, the analysis indicates that there is friction under tensile load. In Fig. 2.11, we show the results of the dynamic friction force versus various applied loads. The fit to all the data is linear. This is the first direct observation of friction under tensile load in a MEMS device. Details of this technique are given in ref. [5]. Our results indicate that for the FOTAS film used here, μ_d=0.28 while μ_s=0.34. In both cases the adhesive force is the same and is 1 nN/ μm^2. More recently, the dynamic coefficient of friction test has been improved so that fewer data points are required to quantitatively assess μ_d. This reduces the time to make the measurement and also reduces any possible wear processes.

2.1.7 Indirect Observations of Pre-Sliding Tangential Deflections (PSTD)

Since the nanotractor can accurately measure static and dynamic friction coefficients μ_s and μ_d, we were motivated to determine if these measurements could describe the operational characteristics of the actuator. This work is more fully described in ref. [2.13] and is briefly reviewed next.

We performed the following test to determine the applicability of μ_s and μ_d to the nanotractor operation:

(1) Clamp the leading clamp at 1.2 mN. Clamp the trailing clamp at a small voltage, from zero to 0.5 mN. (The trailing clamp load is no more than 40% of the leading clamp load).

(2) Actuate the plate.
(3) Release the leading clamp.
(4) Repeat (1)-(3) many times and measure the average step size.

In Step (2), the leading clamp is more heavily loaded than the trailing clamp. If μ_s and μ_d govern the nanotractor performance, we expect that the trailing clamp would slide forward in Step (2), while the leading clamp would stay in place. Also, as the trailing clamp load is increased in Step (1), we would expect the step size to decrease. Indeed, the data in Fig. 2.12 might indicate that these expectations are met, in that the step size decreases as the trailing clamp load increases. Knowing the plate modulus, μ_s and μ_d (as measured on a nearby nanotractor that received the same processing), we can also model the data. The model is also indicated in Fig. 2.12, and appears to agree reasonably well with the data.

We note here that the step size observed in Fig. 2.12 is much smaller than the typical 40 nm nanotractor step size. This is because the device design was changed in this experiment to address a modeling concern. In the standard nanotractor, the actuation electrode extends under the entire plate. This gives rise to a rapid transient phenomenon known as "pull-in". We were concerned that inertial forces associated with pull-in might be important but would be difficult to model. Therefore, we changed the plate actuation configuration to a scheme known as "leveraged-bending" in this work. With leveraged bending, we could avoid the pull-in transient, and still obtain sufficient actuation amplitude to get motion of the device. However, the plate actuation amplitude is not as large as the standard design. Hence, the step size in Fig. 2.12 is a maximum of only 13 nm compared to the typical 40 nm nanotractor step size.

Although the inertial transient is eliminated, there remains an important unknown in the modeling. That is, to reasonably assess the force that the plate can develop, we must assume that there is some compliance in the elastic hinge connection between the plate and the clamp. This compliance will lower the force that the plate can deliver. Although it is difficult to measure the hinge compliance, we can estimate it reasonably well using finite element models. When we used a reasonable value of the hinge compliance to model the data in Fig. 2.12, the model significantly over-predicted the step size at large trailing clamp voltages. That is, the model predicts the actuator will continue stepping at much larger trailing clamp voltages than were observed experimentally. To obtain the model/data agreement in Fig. 2.12, we required an axial compliance 50 times larger than our estimate. This implies that something about the model is incorrect.

The model assumes that the leading clamp is fixed. We devised a test to check this assumption. In the test, we now varied the *leading* clamp load. Because it is still significantly higher than the trailing clamp load, we expect no effect on the results. However, as seen in Fig. 2.13, the results actually do depend on the leading clamp load. This implies that even though the leading clamp static friction force is not surmounted, the leading clamp is slipping backward. The observation that there are small-scale deflections before the static friction event has previously been made in the tribology literature, and has been termed "pre-sliding tangential deflections" (PSTD) [2.14-2.17]. The phenomenon is usually reported for metals that are heavily deformed at their contacting asperity junctions. The stable tangential deflections are thought to be associated with increasing contact area before the static friction limit is reached [2.14]. At sufficiently small displacements, the number of contacting asperities governs reversible "elastic" tangential compliance [2.15] while a much longer "plastic" regime exists before the static friction limit is reached [2.16]. Such μm-scale deflections have also been observed for ceramic materials such as ZrO_2, Al_2O_3 and SiC [2.17].

In the case of the nanotractor, it turns out that this *pre-sliding is very important because the step size is so small*. Better understanding PSTD thus became an important focus of this project. In the following section, we describe experiments to characterize PSTD in more detail.

2.1.8 Direct observations of PSTD

If the circled data in Fig. 2.6 is magnified, we see direct evidence of PSTD, as shown in Fig. 2.14. This data is for a FOTAS monolayer. We observe that substantial slipping (170 nm) occurs before the gross sliding event. For this coating we find a static coefficient of friction of 0.31 ± 0.01 and a dynamic coefficient of friction of 0.265 ± 0.005. The difference between static and dynamic friction leads to the emergence of a few large gross slip events (of many μm) as seen in Figure 2.6, and allow a clear separation of the gross slip and the much smaller PSTD events. We can thus unambiguously attribute the fine structure seen in Figure 2.14 to PSTD.

Interestingly, the frictional characteristics depend on the monolayer used. We have made similar static friction measurements on an OTS-coated nanotractor. Figure 2.15(a) shows the complete friction test curve for one such measurement. As can be seen by comparing to Fig. 2.6, the OTS coating behaves very differently from the FOTAS coating. For this coating we find a static coefficient of friction of 0.102 ± 0.002 and a dynamic coefficient of friction of 0.10 ± 0.01. This small difference in μ_s versus μ_d leads to the almost continuous sliding seen in Figure 2.15a, and makes the separation between gross sliding and PSTD less clear. However, as seen in Figure 2.15b showing a magnified portion of the OTS curve, we can still pick out individual PSTD events, also revealing PSTD on the order of 200 nm. This work is described in more detail in [2.4]. As it turns out much of this slipping appears to be related to time dependent motion as opposed to the effect as seen in the FOTAS. This is described later in this section.

These direct measurements confirm that PSTD is the phenomenon responsible for the data in Figs. 2.12 and 2.13, giving strong evidence to the assertion that the leading clamp slippage plays an important role in the experimental data. Also, because the nanotractor step size of 10-40 nanometers is so much smaller than the characteristic PSTD lengths, it is clear that PSTD and not the coefficients of friction dominate the operational performance of the nanotractor.

We are now intensively studying the detailed characteristics of the PSTD for various monolayers. One long-term goal is to use these characteristics to show that we can predict the step size in the operational tests as shown in Figs. 2.12 and 2.13. Another long-term goal is to understand what phenomena are responsible for these characteristics. Some progress on this understanding will be described next.

We have looked for reversibility of PSTD for FOTAS-coated surfaces. We do this by first stepping down the clamping voltage until we observe PSTD. After slipping approximately 100 nm, we stop ramping down the voltage, and begin ramping up. If PSTD is reversible we would expect the nanotractor position to move back out as clamping force is reapplied. Instead, as seen in the sequence of plots in Fig. 2.16, the position of the nanotractor remains fixed.

Test results are more complicated for OTS-coated surfaces. Simply performing a static friction shows what appears as an almost a constant change of position with voltage. Typical data is shown in Fig. 2.17a. This is a rather surprising result, as the normal force goes as the square of the voltage, and thus we would expect a roughly parabolic shape. As seen in Fig 2.17b, position versus force is not linear. Also, the motion seems to be almost constant sliding, with few distinguishable position plateaus. We modified the static friction test to see if this could be an effect of time dependence. We start by walking the nanotractor out some distance against the load cell. We then step down the voltage by one increment (0.2 Volts), and measure the position using the Moiré grating (identical to the regular static friction test up to this point). We then continue to measure position for the same voltage at a one second interval, and do so until the position has reached equilibrium (defined as an average motion of less than one nanometer over ten seconds). Fig. 2.18a shows the result of this measurement. For each voltage there are many points, separated in time. Fig. 2.18b shows a magnified portion of the position voltage curve near 59 volts. We see that there is a large change in position (~ 2.8 μm) for a constant voltage. In Fig. 2.19 we plot this change of position as a function of time. Clearly the OTS coated nanotractor exhibits large time dependence. Thus in the simple static friction test there is a convolution of a changing normal force with a time dependent motion. As the voltage was decreased at a rate of about two volts per second over one hundred volts (with a full test thus taking about fifty seconds), and the time dependence response is significant between tens and hundreds of seconds, the two time scales were quite similar, and thus both effects were large. Finally, we also plot the final equilibrium positions at each voltage as a function of voltage in Fig. 2.20a. Here we can observe a clear staircase pattern of position plateaus followed by position jumps. The overall shape of the curve is now parabolic, showing position changing as a function of force (voltage squared). Fig. 2.20b shows position as a function of force, and is much

more linear than that seen in Fig. 2.17b. Due to long term drift issues with our position measurements, we cannot say conclusively that we see time-independent PSTD in OTS before each large position jump, though we do believe we have some preliminary evidence of such behavior.

2.1.9 Mechanics model for PSTD

During experimental friction studies using the nanotractor, the response of the device is often non-classical. This response is characterized as a non-linear force-displacement relationship immediately preceding the displacement instability associated with exceeding the frictional strength of an interface. The response, named pre-sliding tangential deflection (PSTD), is shown in Figure 2.21. The inset of the figure shows detail of the PSTD. In this particular experiment, the deflection length is approximately 200 nm, however, it is important to note that the magnitude of the deflection is substantially larger than the length scale of the individual asperity contact radius.

Since the physics that govern PSTD are not obvious, a mechanics model was constructed to simulate the quasi-static response of the nanotractor during a friction test. PSTD, at least superficially, is reminiscent of the accumulated response curves produced by certain discrete, elastic material and joint models. Our PSTD model, in its current form, is a 2D model. It is based upon measured surface topography and utilizes Hertzian contact mechanics. This model does not include inertial effects, so it cannot realistically capture the sliding instability associated with large-scale slip. However, PSTD occurs during the stable phases of tangential displacement and that is precisely the regime in which the model is an accurate reflection of the physics. Note that the model can be easily modified to accommodate contact between coated surfaces and the existence of adhesion between adjacent surfaces.

Figure 2.4(c) shows the parts of the device that come into intimate contact. The profiles of the contacting surfaces were directly sampled from an AFM scan of a polysilicon surface. A portion of the polysilicon surface from which the contacting surfaces were sampled is shown in Figure 2.22. The full scan is 10 μm x 10 μm (1024 x 1024 pixels) with surface roughness of 2.7 nm rms. The height data has been sampled every 10 nm. A 10 μm line scan was randomly selected from the original AFM image in the scan direction and used to model the substrate. Multiple line scans of 2 μm were randomly selected orthogonal to the scan direction, brought separately into point contact with the substrate, then linked together to form the sliding counterface. In all instances, the surfaces were over-sampled by linearly interpolating between data points such that height information is given every nanometer.

In addition to the intrinsic assumptions associated with linear elastic analyses, the contact analysis also employed the standard assumptions of Hertzian contact for multiple asperities. In a departure from actual experimental conditions, the contact analysis assumed silicon-on-silicon contact, whereas the experimental trials typically involved

contact between silicon and a SAM-coated silicon substrate. The silicon properties used in the simulations were Young's modulus, E = 161 GPa and Poisson's ratio ν = 0.23.

As a demonstration of the model's ability to produce an effect that resembled PSTD, it was desired to match the material and physical parameters reflected in the experiment pictured in Figure 2.21. The junction model was used to determine the friction with a junction strength determined experimentally for silicon-on-OTS. Assuming no dependence on pressure, the junction strength of silicon-on-OTS was experimentally determined to be $\tau^* = 195$ MPa. Other than the material parameters, the model relies entirely on the elastic contact model and employs no fitting parameters within the calculations.

The sliding counterface is pressed incrementally (0.01 nm) into the substrate. At each step, local effective interpenetration and radii of curvature are calculated. If the two-dimensional contact model is used, the elastic contact radius cannot be calculated explicitly. The contact radius is determined implicitly and from this value, the local contact force at each contacting location can be determined

$$\begin{aligned} \delta' &= \frac{a^2}{4R'}\left[2\ln\left(\frac{4R'}{a}\right)-1\right] \\ P &= \frac{\pi a^2 E'}{4R'} \end{aligned} \tag{2. 5}$$

For the three-dimensional contact model, the contact radius and local contact force can be determined explicitly

$$\begin{aligned} a &= \sqrt{\delta' R'} \\ P &= \frac{4}{3}E'\sqrt{\delta'^3 R'} \end{aligned} \tag{2. 6}$$

The counterface is pressed into the substrate until the sum of the local contact forces is equivalent to a predetermined normal force. For the experiment pictured in Figure 2.21 the initial normal force was approximately 2.2 mN/nm. Once this force level is achieved, the force that can be resisted in shear can be calculated directly using the current contact area and the assumed junction strength.

$$F_{shear} = \tau^* A \tag{2. 7}$$

Consistent with the experiment, a non-linear tangential restoring force is applied to the counterface. This non-linear restoring force is developed in the device as it is displaced from its neutral position. A curve fit for this restoring force is provided by the following polynomial

$$F_{\tan}(x) = 0.5796 + 4.3572x + 0.1080x^2 + 0.0435x^3 - 0.0001x^4 \tag{2. 8}$$

where x is given in μm and F_{tan} is in μN.

The model simulation begins by comparing the junction force and the device restoring force. If the device restoring force is greater than junction force:

- The counterface is moved incrementally (1 nm) across the substrate.
- At this new location, the vertical position of the counterface is adjusted until the normal force matches that before the tangential displacement.
- The new contact area determines the updated value for the force that can be resisted in shear.
- The current value of the device restoring force is calculated.

If the device restoring force is less than the junction force:

- The counterface is displaced upward (effectively decreasing the normal force and the contact area) until the restoring force exceeds the junction force.
- The previous algorithm is applied with the reduced value of normal force.

The simulation can proceed until the length of the sampled substrate is traversed.

A representative simulation is shown in Figure 2.23. The figure contains elements that resemble the friction experiment shown in Figure 2.21. The simulation features the apparent non-classical PSTD response. Over the duration of the simulation the number of contacting asperities varied from one to six, which is expected to be considerably fewer than the number achieved during the experiment. Figure 2.24 features simulations performed to more closely match the number of contacting asperities expected in experiment. In each instance the substrate was the same, as was the counterface profile; however, the apparent contact area was varied. This was achieved by linking different numbers of the same counterface to move in unison. At the largest apparent contact area, the initial number of contacting asperities was 76, on the order of the number expected during the friction experiments. The figure shows that the response curve of each simulation was qualitatively similar; however, PSTD events did not occur in each of the simulations. A conclusion drawn from this outcome is that the occurrence of PSTD is a complex function of spatial features coupled with the local contact mechanics. Unfortunately, this appears to render determination of phenomenological parameters difficult if not impossible.

The phenomenology of the PSTD mechanism most likely cannot be determined *a priori* through independent investigation of the two intimately contacting surfaces. The simulation shown in Figure 2.23 was however interrogated in an attempt to uncover features common to PSTD events that might be used to aid the development of a phenomenological model. Figures 2.25 and 2.26 illustrate some of the characteristics that PSTD events seem to share. In both figures the blue curve is referenced to the left axis and the green curve is referenced to the right axis. The range over which PSTD occurs is indicated by pairs of dashed lines. The figures show that during PSTD, the number of contacting asperities remains constant, but perhaps more interestingly, the true contact

area also remains essentially constant. This seems to provide further evidence for a randomly occurring event. During PSTD, the applied normal force is decreasing, but the local contact parameters (effective interference and effective curvature) are evolving in such a way that contact area remains the same.

2.2 Wear of polysilicon surfaces

Friction and wear are major limiting factors for the development and commercial implementation of devices fabricated by surface micromachining techniques. The nanotractor enables us to study the wear of MEMS surfaces. This *in-situ* approach to measuring tribological properties of MEMS, combined with high-resolution atomic force microscope images of wear tracks, provides insight into the effects of processing on wear. In particular, surface monolayer coatings have a significant positive effect, while surface texturing does not strongly affect performance [2.18].

The work performed thus far indicates that the nanotractor is a promising vehicle for *in-situ* wear studies on MEMS devices. Although more experiments are needed and further development of the testing methodology is required, several conclusions can be made. First, the nanotractor device fails via interfacial seizure due to wear processes at the sliding interfaces under well-characterized loading conditions. Although it will be necessary to develop more sensitive *in-situ* tests, this is a necessary observation to justify the further development of nanotractor wear tests. Second, the tests were conducted under 44 kPa apparent pressure, and noticeable wear of the polysilicon surface was observed. With this device, it should be possible to study the onset of wear as a function of lighter loading conditions. Third, a monolayer lubricant of FOTAS significantly enhances the wear resistance of MEMS surfaces. Fourth, surface roughness does not strongly affect wear properties, based on the limited number of measurements so far. Fifth, as long as only a limited amount of friction testing is conducted, we can directly measure the friction coefficient as a function of wear. It is possible to measure friction for monolayer-coated surfaces, since not much change with number of friction tests cycles is observed. For the oxide-coated surfaces, friction tests should be performed at lower loads. Sixth, the friction coefficient can vary substantially, long before failure and before device performance (such as travel distance) is altered. Finally, AFM can be applied to study surface modification without damaging or even contacting the nanotractor device, because of the large travel distances (>20 μm) that the nanotractor undergoes during a wear test. Therefore, in future studies it should be possible to conduct wear and AFM tests sequentially on the same device to follow the evolving topography. These results are important for the understanding of MEMS device reliability. We have shown that this unique, *in-situ* method is highly revealing and holds promise for developing a more quantitative and predictive understanding of MEMS device reliability. See [2.18] for more details.

A wear study subsequent to that reported on in [2.18] was also conducted. It addressed some of the limitations from the earlier study. In particular, we were able to write test programs that showed a graceful degradation of the nanotractor, as opposed to

the abrupt degradation seen in the previous work. A manuscript describing this newer testing procedure and the results has been drafted [2.19].

2.3 Impact of nanotractor and MEMScript on Sandia National Laboratories' applications

The nanotractor has been successfully demonstrated in two of Sandia's prototype devices. In one application, it was used by Mark Polosky (Dept. 2614) to enable a countermeshing gear mechanism. In a second application, Daryl Dagel (Dept. 1769) has made use of the high force and large displacement characteristics of the nanotractor in an optical application being jointly developed with Lockheed-Martin Company. In that application, 100,000 cycles are required and nanotractor wear is an issue that requires attention.

MEMScript was built on a very general conceptual platform integrating actuation, interferometry, machine vision and easy programming. It is rapidly becoming the standard test software at Sandia for a wide range of polysilicon surface micromachined applications. These include, but are not limited to, scratch-drive actuators (the OPAL project), microengines (used as process monitors in the light lab and the fab), and in the AIM lab for interferometry and adhesion testing. We are considering marketing MEMScript software.

2.4 References

2.1. J. Gao, W. D. Luedtke, D. Gourdon, M. Ruths, J. N. Israelachvili and U. Landman, *Frictional force and Amontons' Law: From the molecular to the macroscopic scale*, J. Phys. Chem. B **108** (11), 3410 (2004).

2.2. M. P. de Boer, D. L. Luck, W. R. Ashurst, A. D. Corwin, J. A. Walraven and J. M. Redmond, *High-performance surface-micromachined inchworm actuator*, J. Microelectromech. Syst. **13** (1), 63 (2004).

2.3. M. G. Hankins, P. J. Resnick, P. J. Clews, T. M. Mayer, D. R. Wheeler, D. M. Tanner and R. A. Plass, *Vapor deposition of amino-functionalized self-assembled monolayers on MEMS*, Proceedings of the SPIE, Vol. 4980, edited by R. Ramesham and D. M. Tanner, San Francisco 2003), pp. 238-247.

2.4. A. D. Corwin, M. D. Street, R. W. Carpick, W. R. Ashurst and M. P. de Boer, *Pre-sliding tangential deflections can govern the friction of MEMS devices*, 2004 ASME/STLE Joint International Tribology Conference, G. G. Adams and L. Kogut, Long Beach, California USA (October 24-27, 2004 2004).

2.5. A.D. Corwin and M.P. de Boer, *Effect of adhesion on dynamic and static friction in surface micromachining.* Applied Physics Letters, 2004. **84**: p. 2451-2453.

2.6. U. Srinivasan, M. R. Houston, R. T. Howe and R. Maboudian, *Alkyltrichlorosilane-based self-assembled monolayer films for stiction reduction in silicon micromachines*, J. Microelectromech. Syst. **7** (2), 252 (1998).

2.7. W. R. Ashurst, C. Yau, C. Carraro, C. Lee, R. T. Howe and R. Maboudian, *Alkene based monolayer films as anti-stiction coatings for polysilicon MEMS*, Sensors and Actuators A **9** (3), 239 (2001).
2.8. W. R. Ashurst, C. Yau, C. Carraro, R. Maboudian R and M. T. Dugger, *Dichlorodimethylsilane as an anti-stiction monolayer for MEMS: A comparison to the octadecyltrichlosilane self-assembled monolayer*, J. Microelectromech. Syst. **10** (1), 41 (2001).
2.9. G. T. Mulhern, D. S. Soane and R. T. Howe, *Supercritical carbon dioxide drying of microstructures*, Proc. 7th Int. Conf. Solid-State Sensors and Actuators, Transducers '93, Yokohama, Japan (June 7-10 1993), pp. 296-299.
2.10. E. M. Russick, C. L. J. Adkins and C. W. Dyck, *Supercritical carbon dioxide extraction of solvent from micromachined structures,* in Supercritical Fluids, Extraction and Pollution Prevention; *Vol. 670 of* M. A. Abraham and A. K. Sunol (American Chemical Society, Washington, DC, 1997), pp. 255-269.
2.11. M. B. Sinclair, A. D. Corwin and M. P. de Boer, *An in-situ Moiré metrology for routine 1 nanometer displacement measurements in MEMS*, to be submitted (2004).
2.12. A. D. Corwin and M. P. de Boer, *Scripting software for MEMS automation and actuation*, to be submitted (2004).
2.13. D. L. Luck, M. P. de Boer, W. R. Ashurst and M. S. Baker, *Evidence for pre-sliding tangential deflections in MEMS friction*, Transducers 2003, Boston 2003), pp. 404-407.
2.14. J.S. Courtney-Pratt and E. Eisner, *The effect of tangential force on the contact of metallic bodies*, Proc. Roy. Soc. Lond. A. **238**, 529 (1957).
2.15. P. Berthoud and T. Baumberger, *Shear stiffness of a solid-solid multicontact interface*, Proc. Roy. Soc. Lond. A. **454**, 1615 (1997).
2.16. J. Ni and Z. Q. Zhu, *Experimental study of tangential micro deflection of interface of machined surfaces*, J. Manuf. Sci. & Eng. - Trans. ASME **123** (2), 365 (2001).
2.17. T. Fujimoto, Kagami J, T. Kawaguchi and T. Hatazawa, *Micro-displacement characteristics under tangential force*, Wear **241**, 136 (2000).
2.18. E. E. Flater, A. D. Corwin, M. P. de Boer, M. J. Shaw and R. W. Carpick, *In-situ wear studies of surface micromachined interfaces subject to controlled loading*, Wear **submitted** (2004).
2.19. G. Subhash, A. D. Corwin and M. P. de Boer, *Operational Wear and Friction in MEMS Devices*, to be submitted (2004).

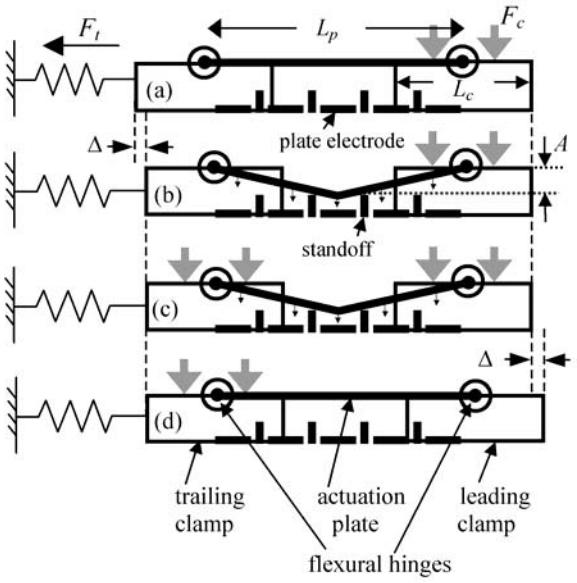

Fig. 2.1 Nanotractor schematic with signals applied to achieve motion to the right. The plate electrode is segmented by grounded standoffs that prevent electrical shorting of the plate to the plate electrode and establish amplitude *A*.

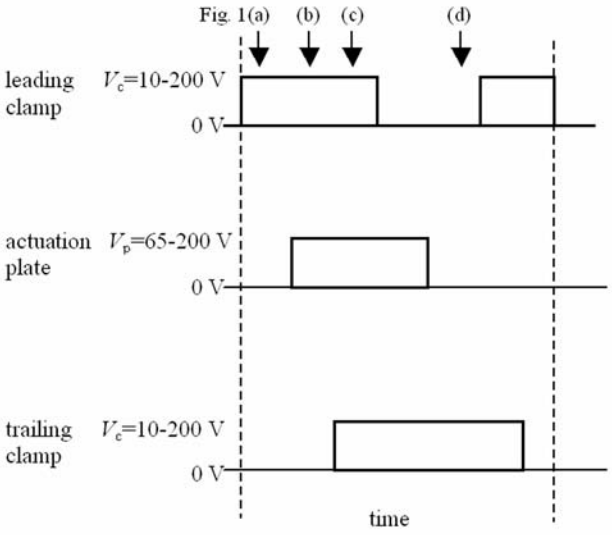

Fig. 2.2 Timing diagram for Fig. 2.1 (one cycle). Voltage ranges indicate levels over which device will operate.

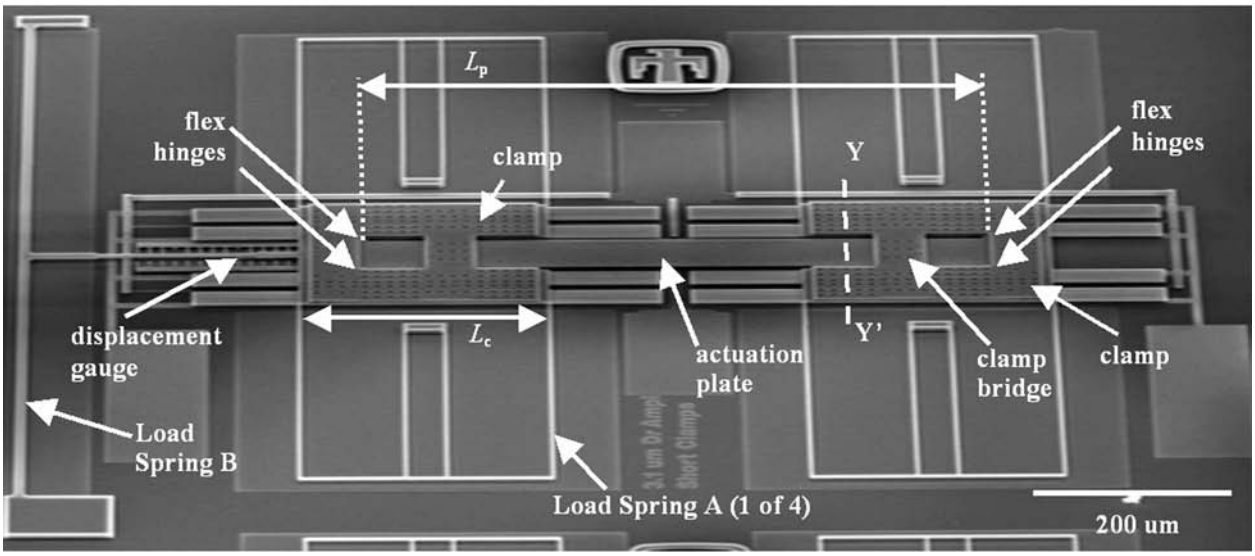

Fig. 2.3 SEM image of the nanotractor (L_c=200 μm).

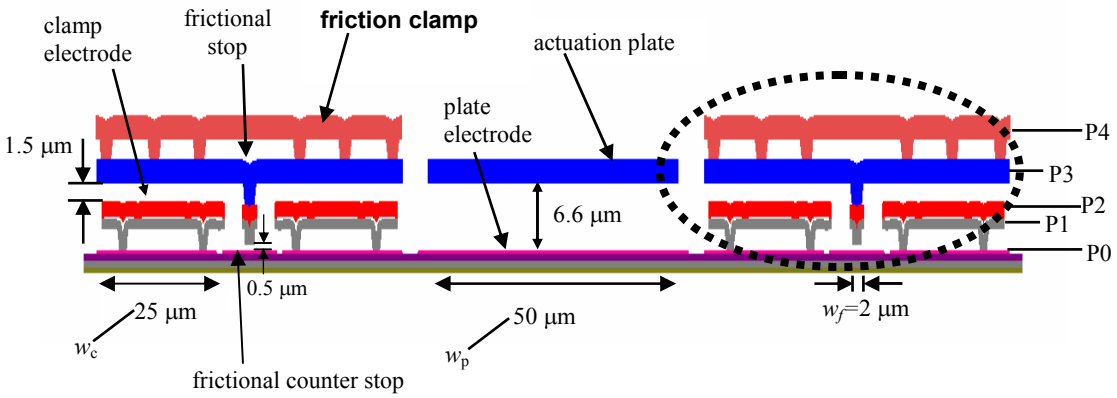

Fig. 2.4(a) A schematic cross-section at YY' as indicated in Fig. 2.3 showing the friction clamp design and actuation plate. A dual clamp design is used for electromechanical stability and the P4 layer significantly enhances the clamp bending stiffness. The actuation plate, friction clamp, friction stop and its opposing counterface are electrically grounded. Actuation is achieved via the plate and clamp electrodes. The four clamp electrodes shown are at the same potential. Grounded stops (as shown in Fig. 2.1) prevent shorting of the plate to the plate electrode. The width direction in (a) is compressed 2 times relative to the height direction. The circled area is shown in (b).

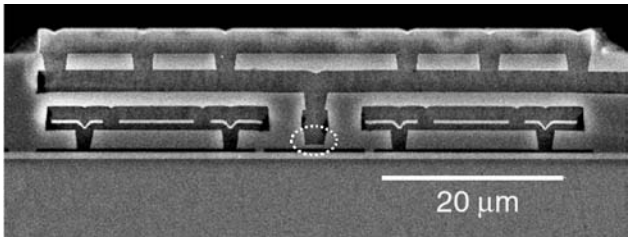

Fig. 2.4(b) SEM cross-section of right side of clamp before etch release. The circled area is shown in (c).

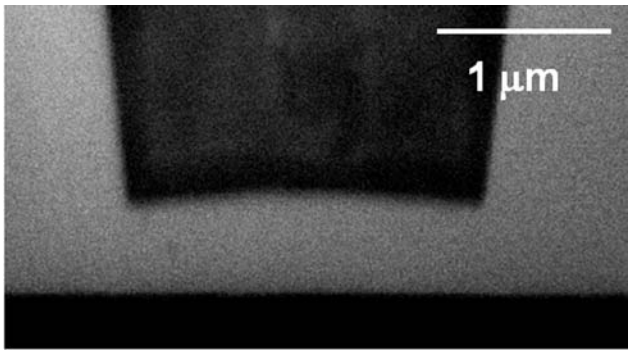

Fig. 2.4(c) SEM close-up of friction foot and the lower P0 counterface before etch release.

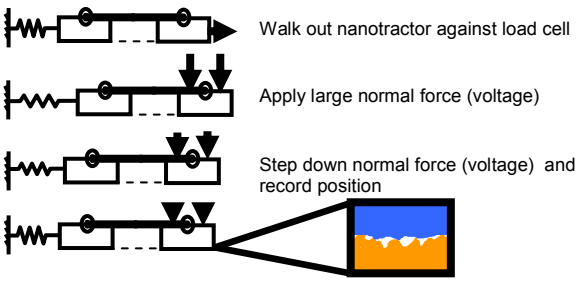

Fig. 2.5. Schematic diagram showing a nanotractor static friction test.

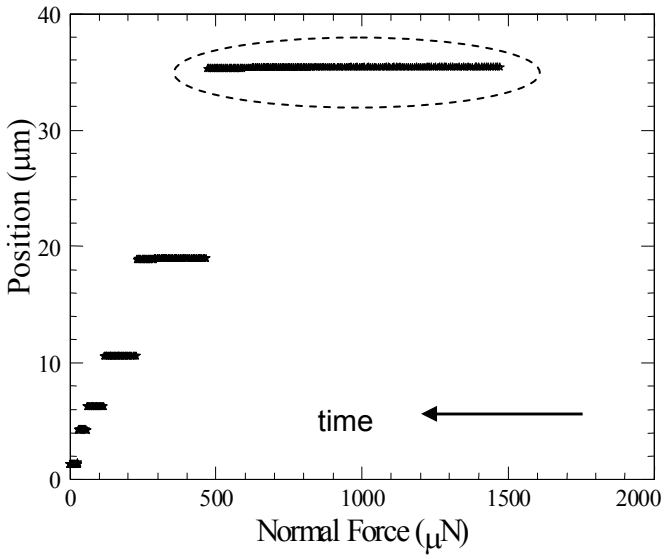

Figure 2.6. A static friction test from a FOTAS coated nanotractor. (data inside the dotted circle is magnified in Fig. 2.14)

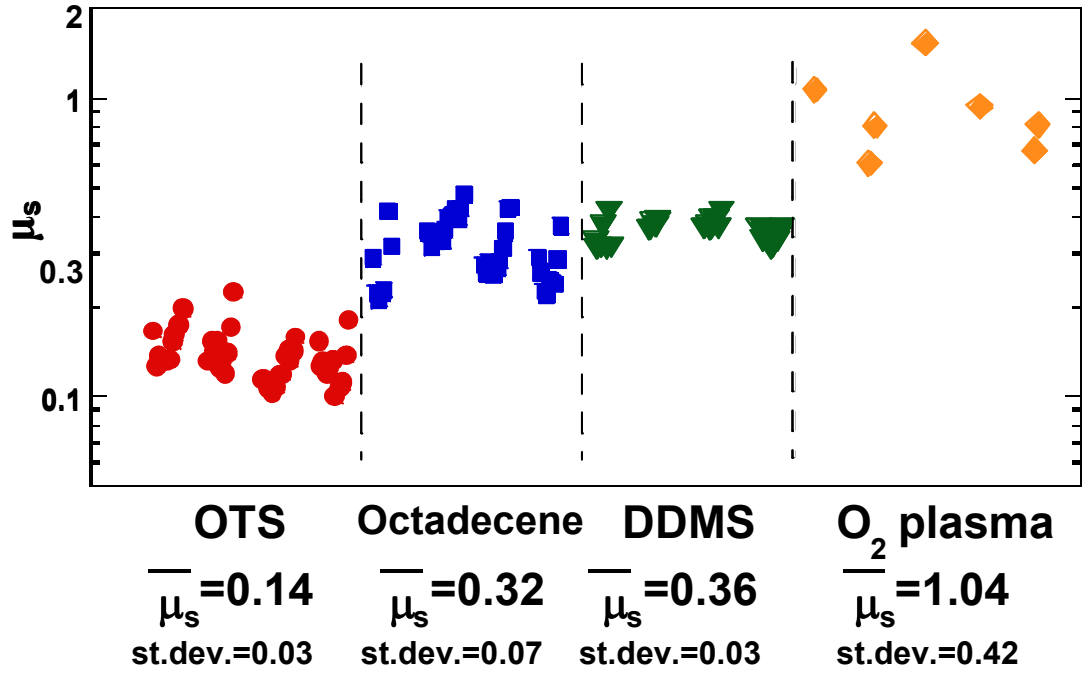

Fig. 2.7 Static coefficients of friction measured using Load Spring B as the actuator. Note the logarithmic scale for the μ_s axis. For each coating, the data is from four devices on two chips using both L_c =600 μm and L_c =200 μm. Measurements from an individual device are grouped together, and moving to the right within a group corresponds to decreasing normal load. For the O_2 plasma, data from three chips are shown because there are only one or two slip events per device.

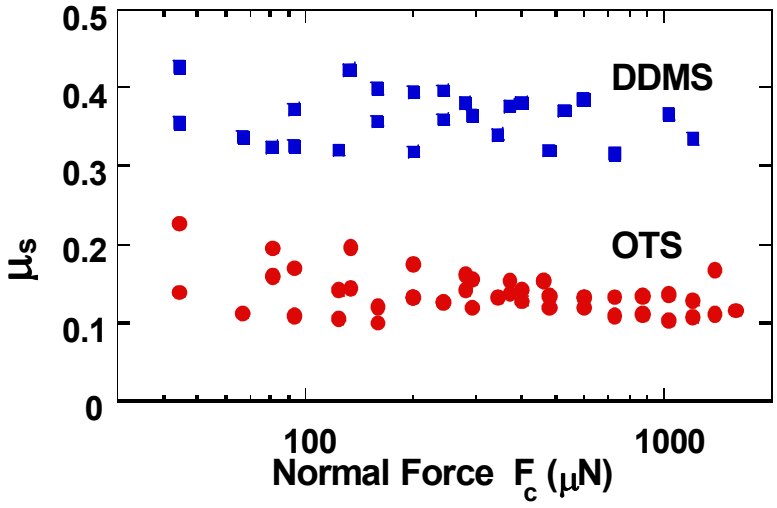

Fig. 2.8 The data of Fig. 2.7 is recast versus normal force. The static coefficients of friction are independent of normal load over 1.5 orders of magnitude, suggesting that Amontons' law is valid for MEMS surfaces at sufficiently high loads.

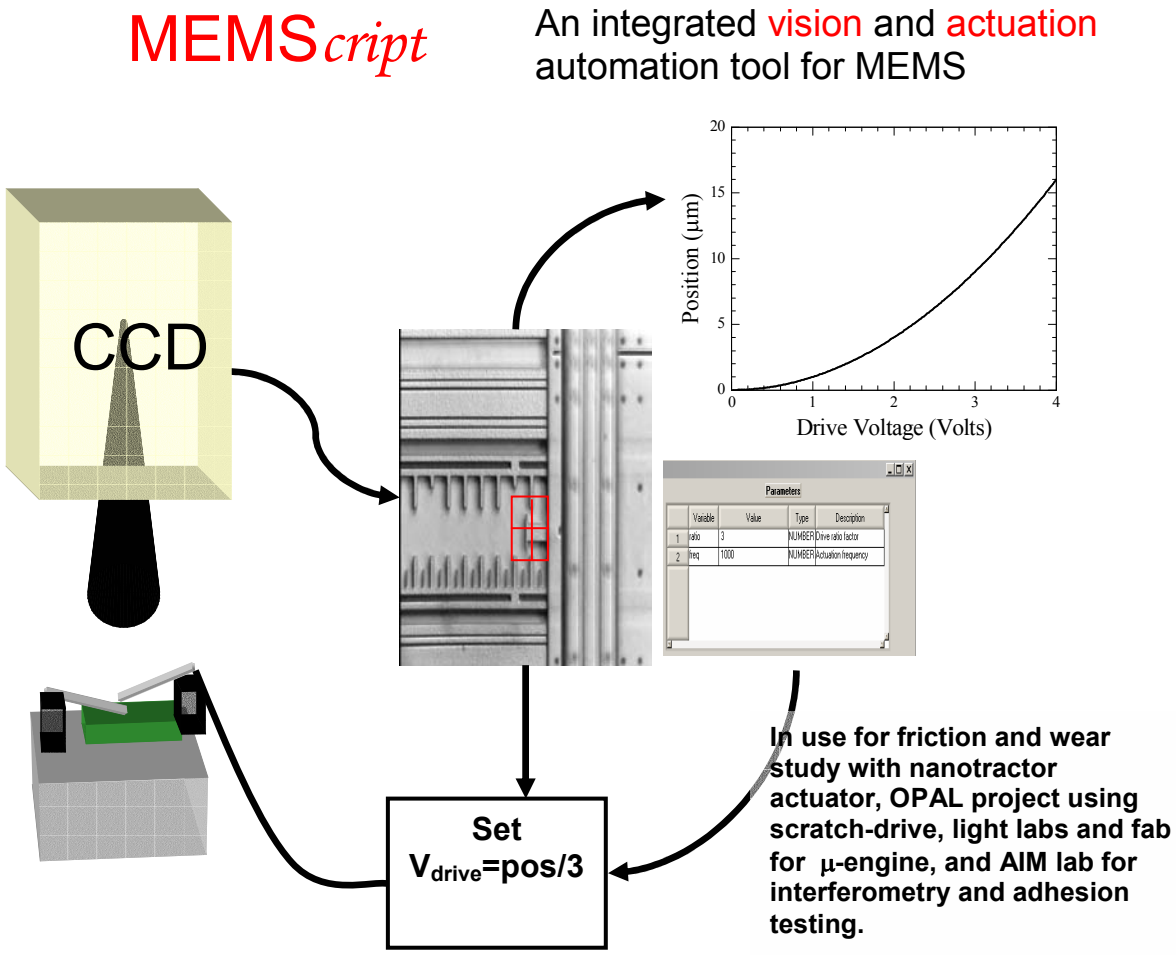

Intelligent Actuation: Combine real time in-plane, interferometric, and stroboscopic vision capabilities with full scripting power to allow actuation to respond to vision data in real time

Flexibility: Works with a variety of National Instruments image capture and digital to analog boards, as well as GPIB and serial devices. Interface to external programs via DDE (i.e. LabView)

Simplicity: Presents simple user interface to allow use without knowing scripting language

Power: Full featured scripting engine written in C includes full branching (make decisions on the fly), arithmetic function evaluation (calculate on the fly), graphing (display on the fly), file output (save data and images for further analysis/presentation)

Fig. 2.9a Schematic representation of MEMScript software.

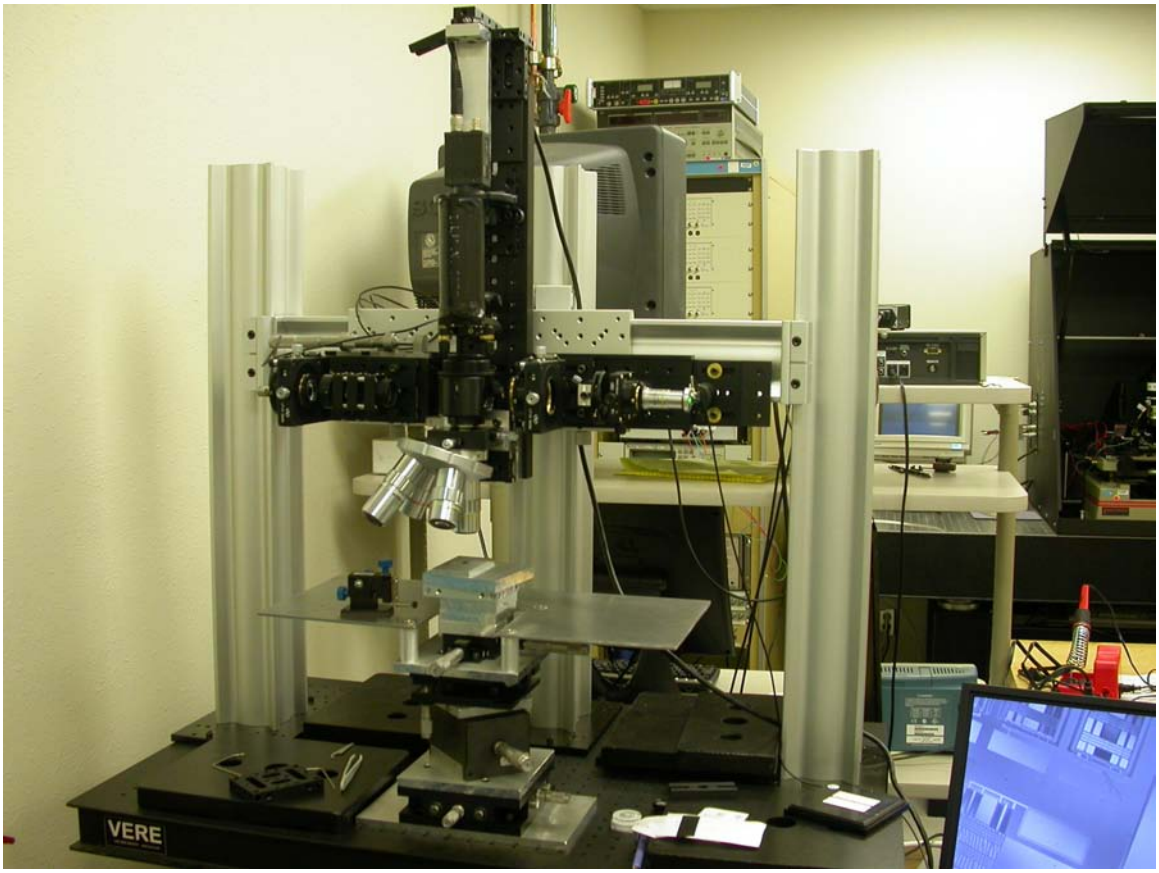

Fig. 2.9b High resolution probe station developed for resolving 1 nanometer in-plane motion detection for MEMS.

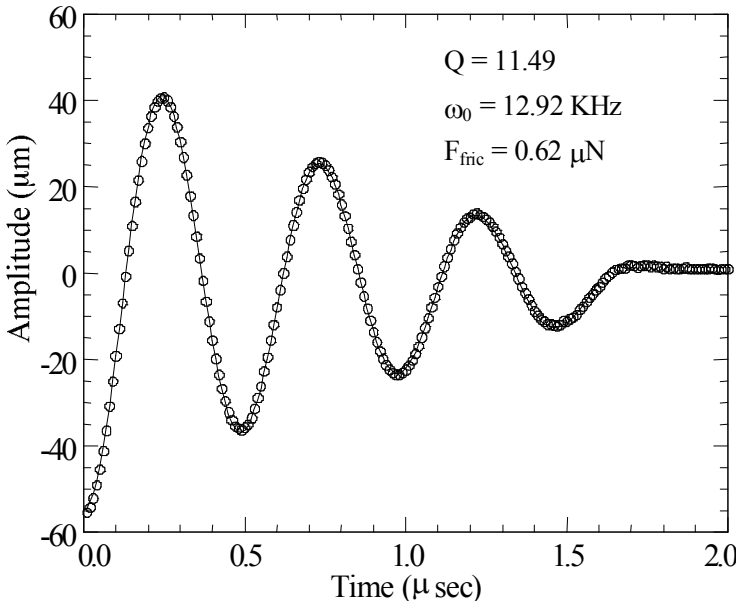

Fig. 2.10 Dynamic friction data describing the in-plane tractor tip motion after slip.

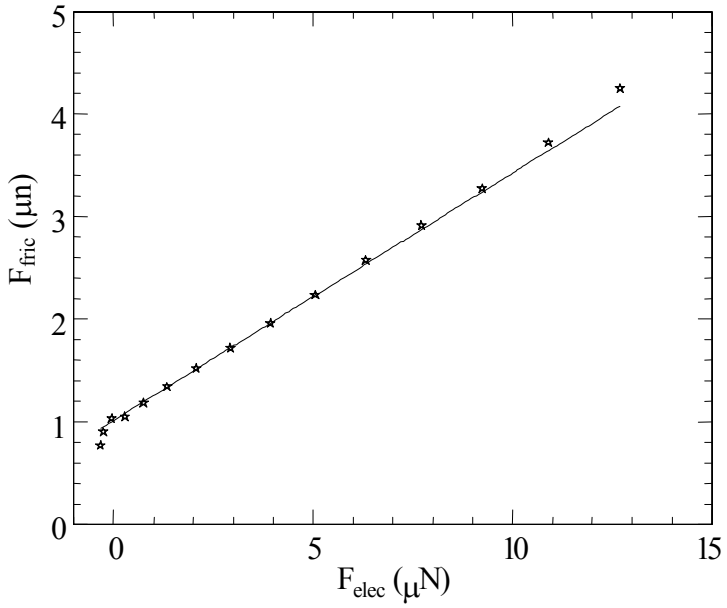

Fig. 2.11 Dynamic friction force versus applied load.

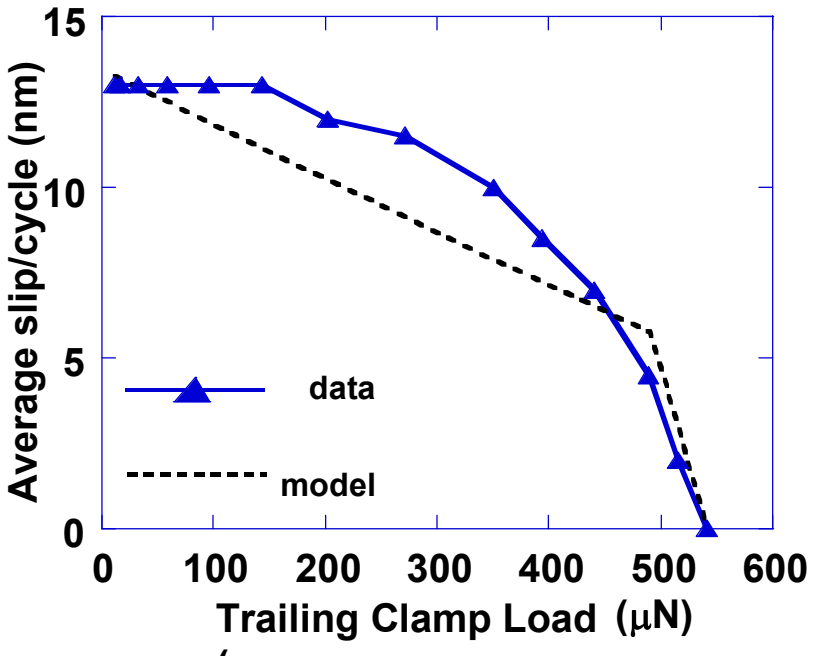

Fig.2.12 Best model fit to the data. A very large value of axial compliance $\gamma_F = 52 \bullet 10^{-6}$ μN/μm is needed to fit the endpoint at large trailing clamp load.

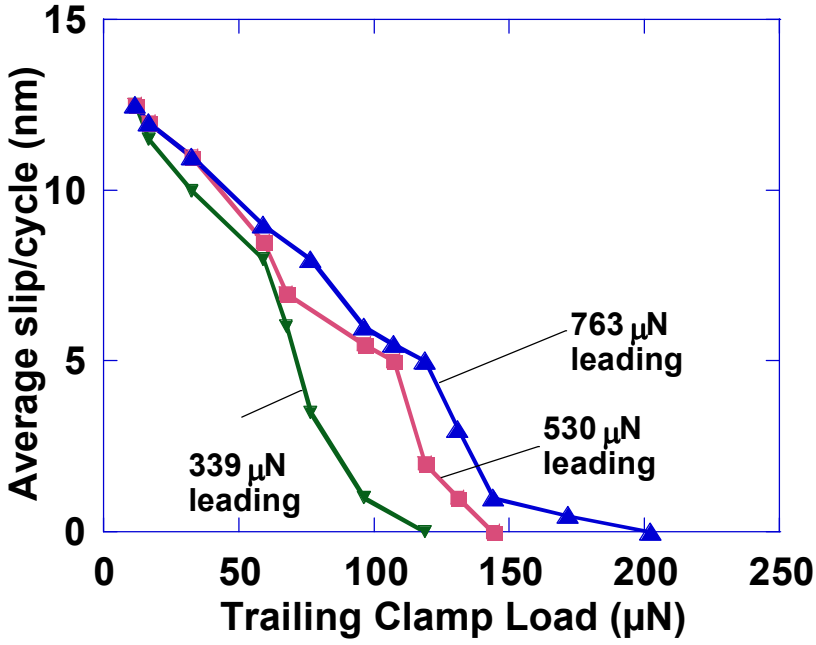

Fig. 2.13 Slip/cycle for a PF8TAS-coated inchworm for three different leading clamp loads. Plate actuator voltage V_P = 105 V, cycle frequency is 400Hz.

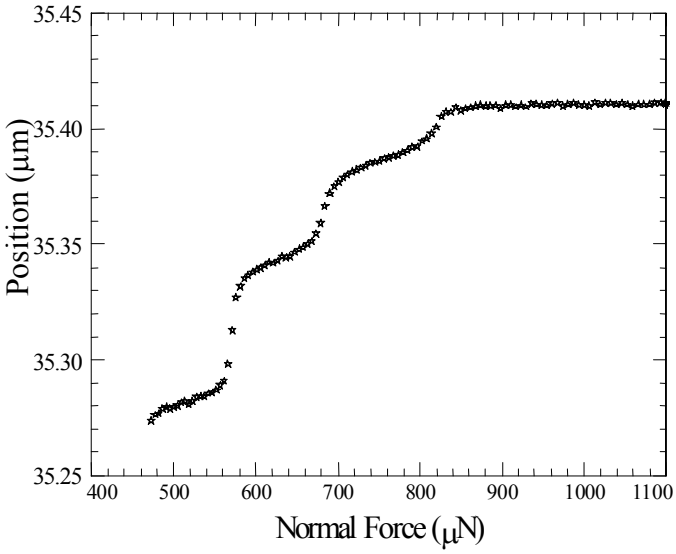

Fig. 2.14 A magnified portion (the dotted circle of Fig. 2.6) from a FOTAS-coated nanotractor.

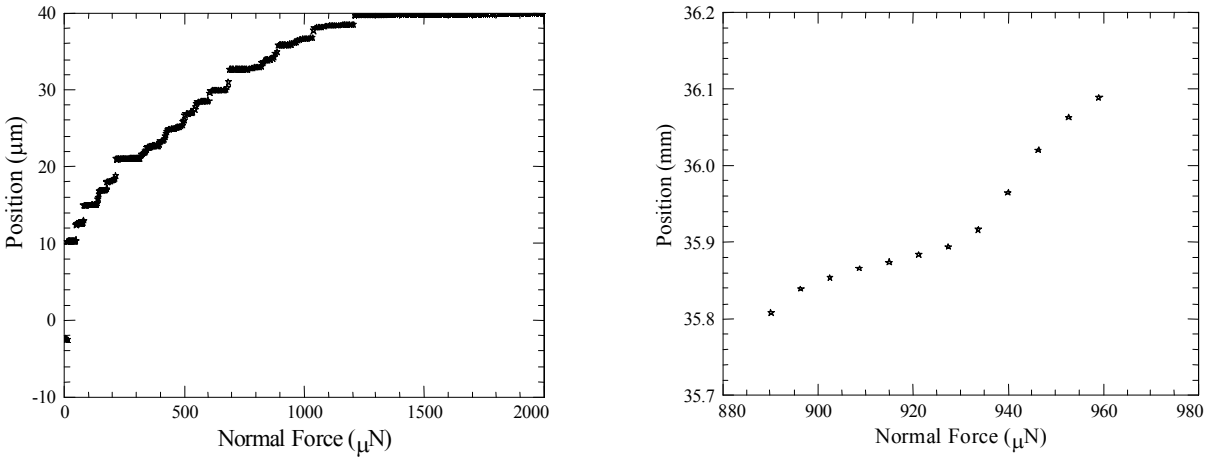

(a) (b)

Fig. 2.15(a) A static friction test from an OTS coated nanotractor, (b) A magnified portion of a static friction test from an OTS coated nanotractor.

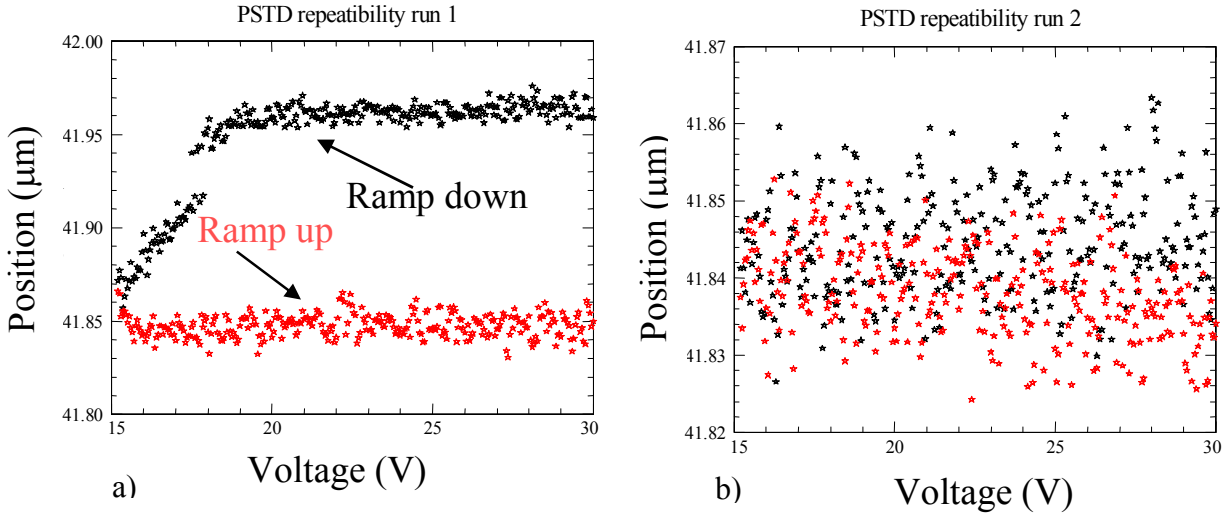

Fig. 2.16 PSTD reversibility test. a) After partially traversing a PSTD event, ramp up the voltage showing that the slip tangential deflection is not recovered. b) Ramp voltage down (black) and then back up again (red) with no change in position within measurement resolution.

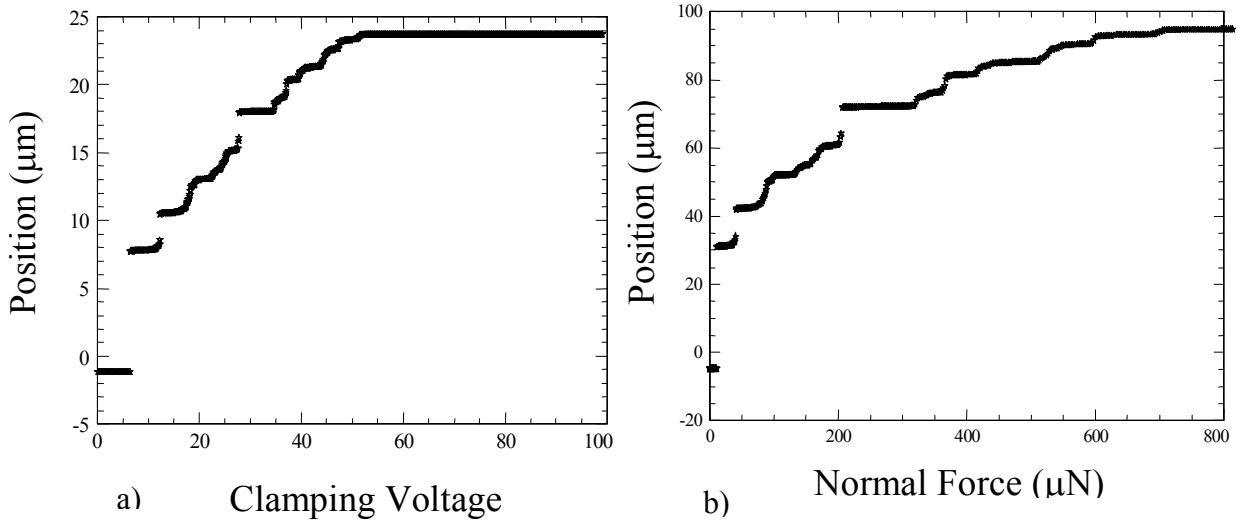

Fig. 2.17 Static friction test performed on with OTS coated nanotractor. a) Position as a function of voltage. Note the almost linear change in position as a function of voltage (voltage ramped down at 2 Volts/sec) b) Position as a function of normal force.

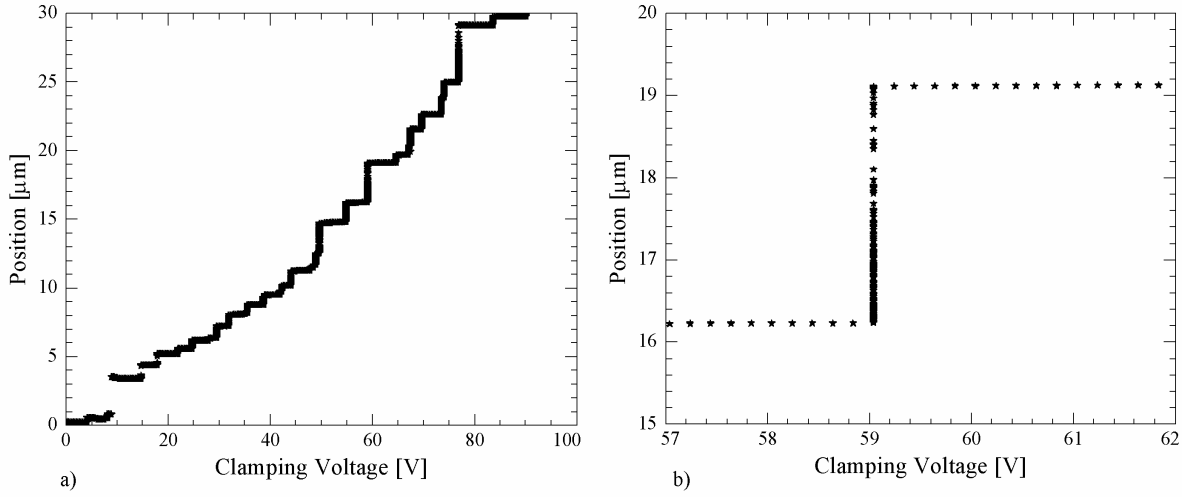

Fig. 2.18 Modified static friction test. At each voltage, data is taken until the position stops changing with time. a) Position as a function of voltage over full voltage range. b) Position as a function of voltage for a magnified portion, showing that multiple points are taken for each voltage.

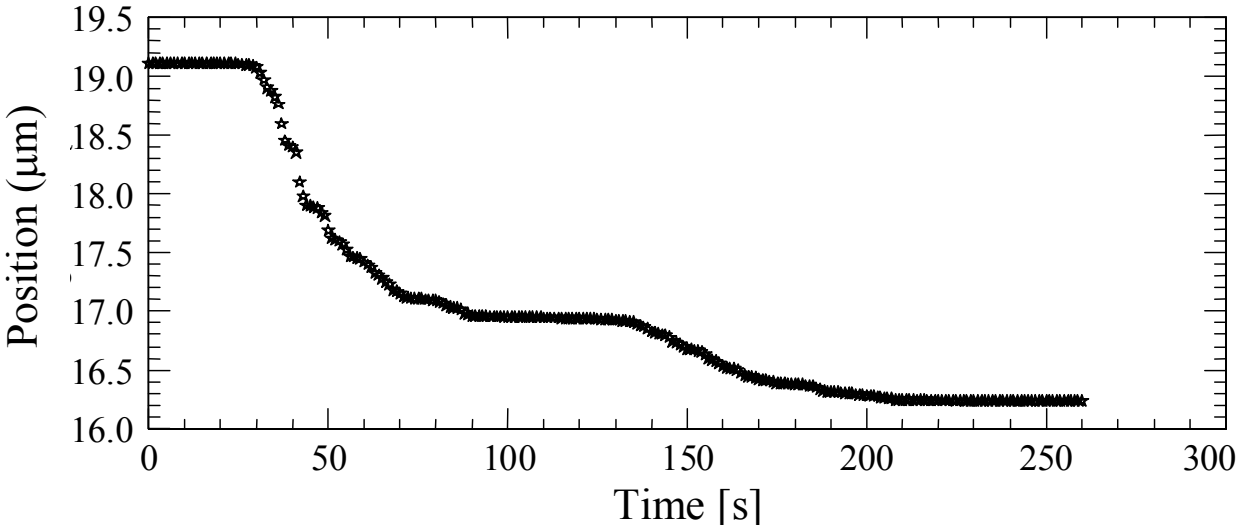

Fig. 2.19 Time dependence of data from Fig. 2.16 at 59 volts.

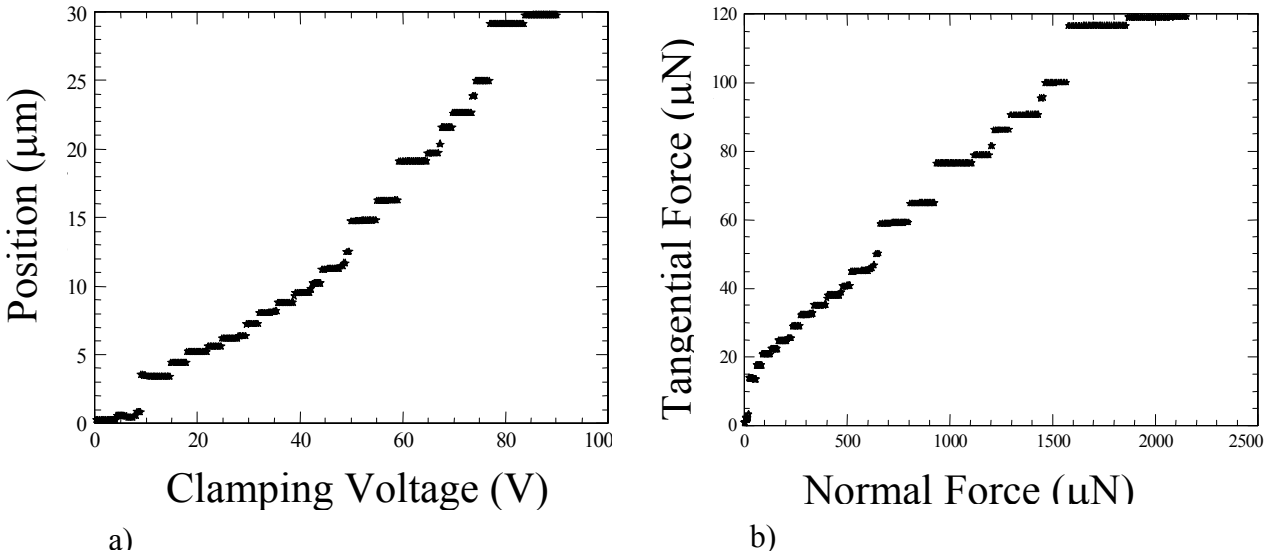

Fig. 2.20 Equilibrium position static friction test data. a) Position as a function of voltage. b) Tangential force as a function of normal force.

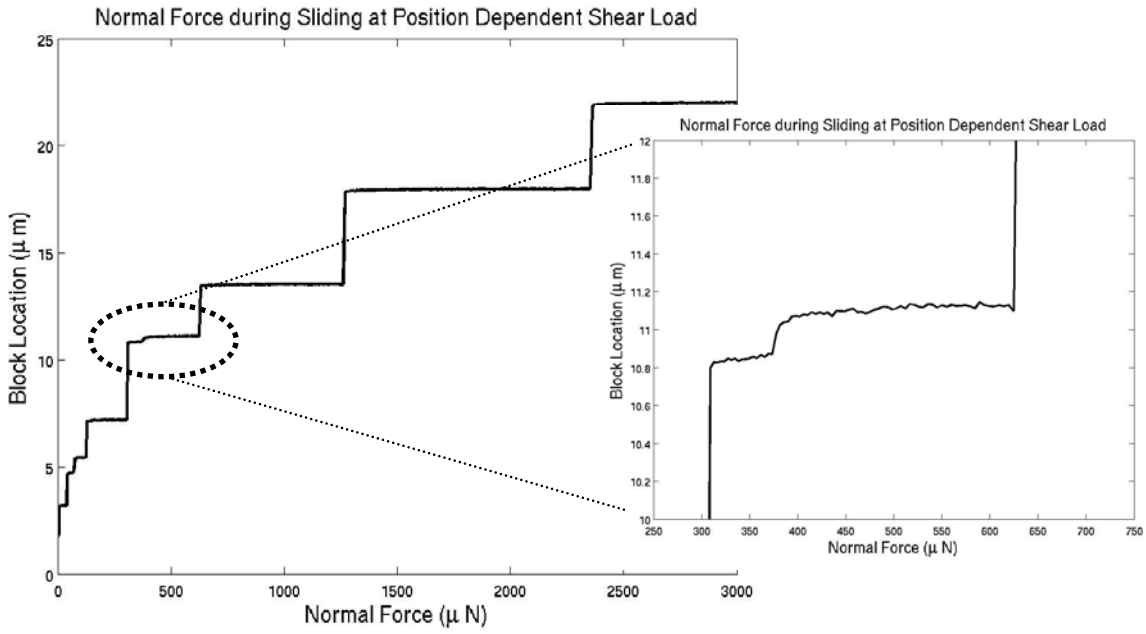

Fig. 2.21. During a friction experiment, the normal clamping force is measured as a function of the location of the contacting counterface. The inset shows an instance of pre-sliding tangential deflection (PSTD), wherein the counterface displaces in a quasi-static manner over a distance significantly larger than an individual asperity contact radius.

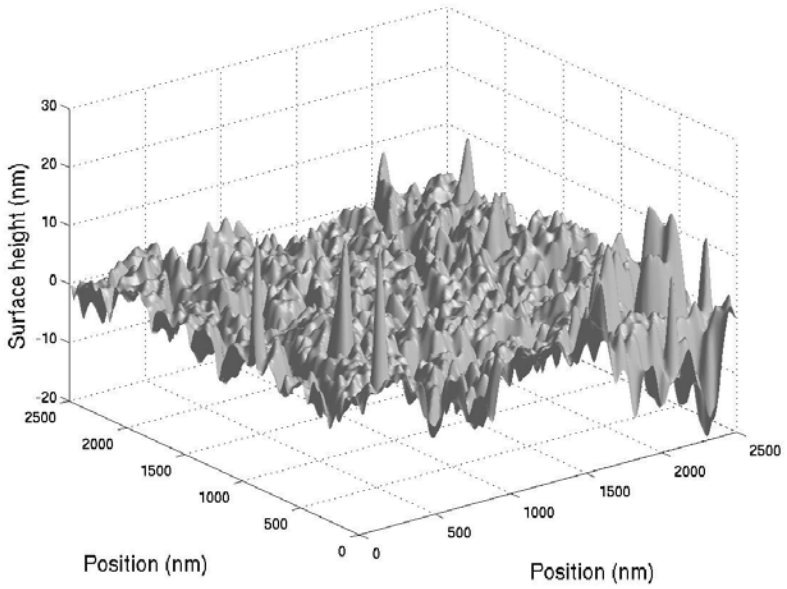

Fig. 2.22. Height profile of the AFM scan from which the contacting nanotractor surfaces were sam μm scan with 2.7 nm rms rou

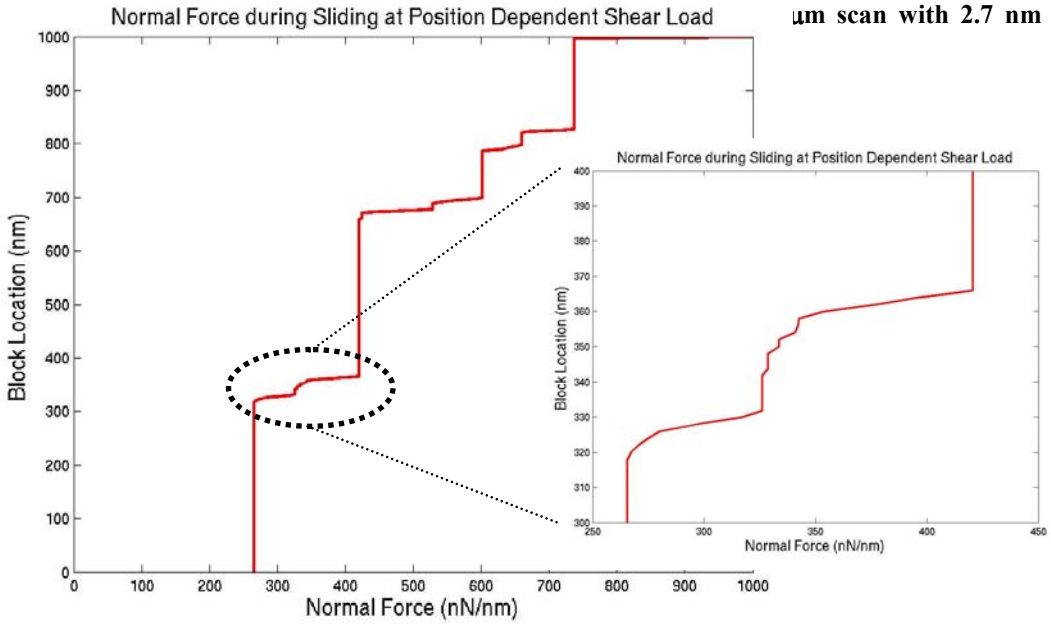

Fig. 2.23. A model simulation apparently produces an effect that looks like PSTD. The inset shows details of the simulated PSTD that have a deflection length scale off the same as order as that seen experimentally.

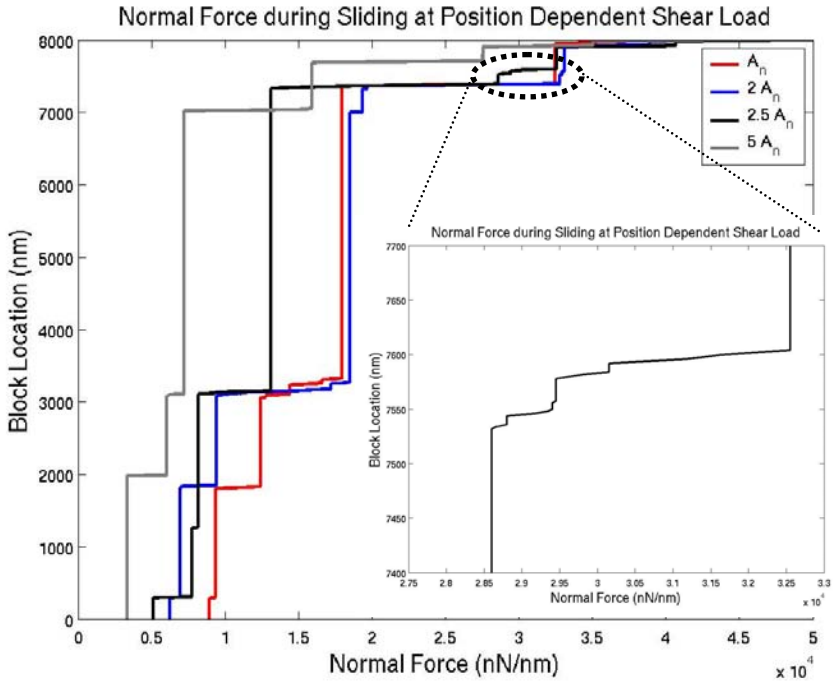

Fig. 2.24. A model simulation was performed in which the effective contact area was increased while applying the same initial normal and tangential forces. The appearance of PSTD in only one of the cases implies a complex dependence of the effect on surface topography and local contact mechanics.

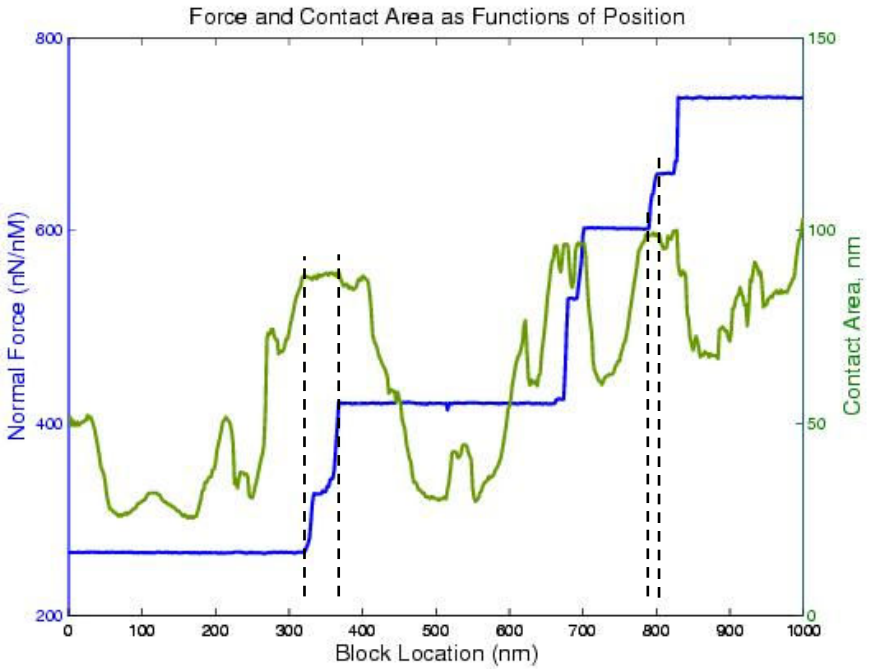

Fig. 2.25. During a simulated PSTD event, the contact area remains constant. The two significant PSTD events from this simulation are indicated by the dashed lines.

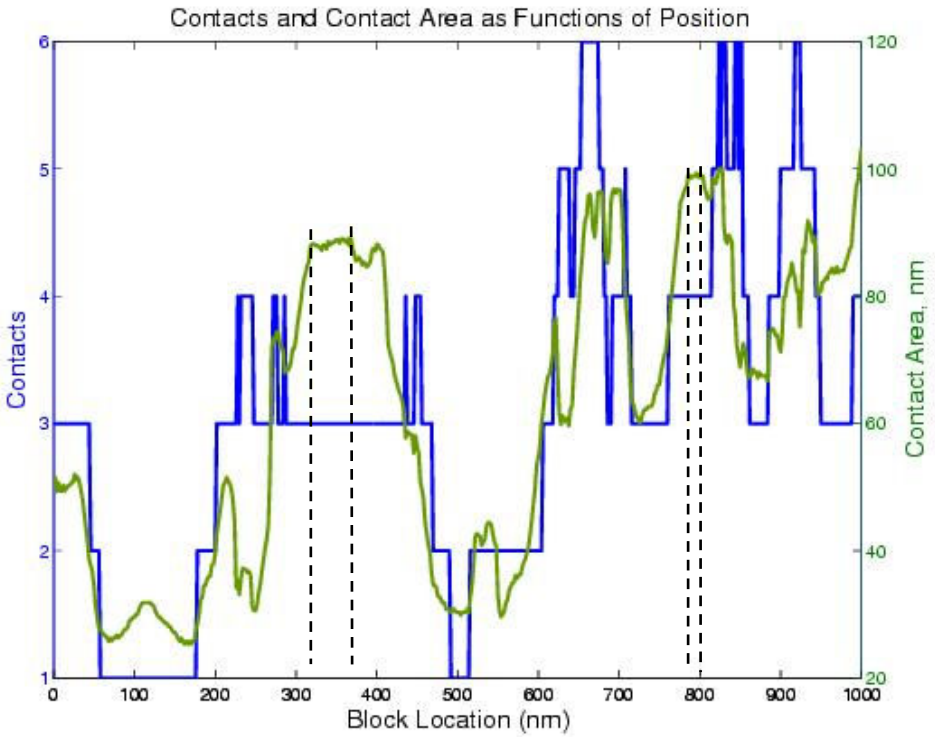

Fig. 2.26. During a simulated PSTD event, the number of contacts remains constant. The two significant PSTD events from this simulation are indicated by the dashed lines.

3. Asperity-level finite element simulations

3.1. Background

We have seen in Section 2 that the nanotractor can be used to make detailed friction measurements of MEMS surfaces. One of the major goals of this project is to develop a high fidelity, mechanics-based finite element simulation capability that can be used to establish a fundamental understanding of the experimental data. In this section, we describe an initial capability to perform asperity-level finite element simulations. These simulations include asperity-level adhesional and frictional surface interactions and use a mesh generated directly from an atomic force microscope (AFM) image to produce a detailed description of surface topography. This capability enables a thorough investigation of asperity interactions. For example, one can investigate to what extent small-scale features in the relatively complex polysilicon topography influence frictional response. This capability can also provide a more fundamental understanding of the effect of surface coatings on asperity contact and frictional forces and the origin and mechanisms of wear in contacting and sliding polysilicon surfaces. Such detailed information is also useful when formulating grid-scale, homogenized models that do not explicitly model individual asperities. Key aspects of this asperity-level modeling capability are discussed below and an illustrative example demonstrating its application is presented.

3.2. Surface interaction models

Two surface interaction models have been implemented into Sandia's three-dimensional, transient dynamics, PRESTO finite element code [3.1] to enable the asperity-level calculations. The Adhesion Model combines frictionless contact with an adhesive traction that scales with the relative normal distance between opposing surfaces. The Junction Model enhances the adhesion model with a velocity-dependent shear traction (junction strength) that opposes the relative tangential motion of the surface when it is in contact. This latter model was motivated by previously published work that suggests that AFM friction test data can be simulated with a pressure and velocity independent shear junction strength [3.2, 3.3]. Contact capabilities in PRESTO are provided by ACME (*Algorithms for Contact in a Multiphysics Environment* [3.4]), and the Adhesion and Junction Models were implemented via ACME. Figure 3.1 presents results that demonstrate PRESTO's ability to accurately simulate contact and the effect of adhesion. These results are for a cylindrical polysilicon asperity with a 27-nm spherical tip contacting the flat surface of a cylindrical polysilicon substrate (Fig. 3.2). The polysilicon is treated as a linear elastic material with a Young's modulus, E, of 161 GPa and a Poisson's ratio, ν, of 0.23. The adhesion vs. separation model is based upon a Lennard-Jones potential and corresponds to the adhesive force/unit area between two half-spaces [3.5]. Also note that in the simulations the tip is pushed at a sufficiently slow velocity (~ 1-m/s) to produce a quasi-static repsonse. Figure 3.1 shows that when there is no adhesion (the work of adhesion, W, equals 0.00 J/m^2) the PRESTO analysis accurately reproduces the Hertz solution for an elastic silicon sphere contacting an elastic silicon

plane. When there is adhesion (W= 0.05 J/m^2), the calculated results are in excellent agreement with the DMT-like limit solution as determined by Maugis for a Dugdale adhesive zone model [3.5]. This solution applies to hard solids with small radii of curvature and low work of adhesion----as is the case of the problem analyzed (Fig. 3.2). According to this theory, the contact stress distribution is Hertzian, but the integral of the stress distribution equals $P+2\pi WR$, where P is the applied load and R is the radius of curvature of the asperity.

3.3. Determining parameters for surface interaction models

One of the key issues in the modeling effort is to define the values of the Junction Model parameters (W and the junction strength, τ^*), since these values specify the magnitude of asperity-level adhesional and frictional surface interactions. One potentially promising approach for deducing these parameter values is to use AFM friction and adhesion test data. In an AFM friction test, lateral force (friction) is measured as a function of applied normal force as the AFM tip scans along a line on the surface. The values of W and τ^* are not measured directly in this test, but must then be inferred from a contact mechanics analysis. To illustrate this approach, consider the case of AFM friction test data for a silicon tip sliding over an OTS-SAM coated silicon substrate. The contact problem of interest is that of a 25-35 nm radius, silicon asperity (the AFM tip, whose radius can be determined independently) contacting a roughly 2-nm thick, SAM-coated substrate. Both the tip and the substrate are linear elastic and have the same Young's modulus, E, of 161 GPa, and the same Poisson's ration, ν, of 0.23. Simple, analytic solutions (e.g., Dugdale-DMT) might be applicable if the relatively compliant, but thin SAM coating could be ignored. For this reason, a series of preliminary calculations were performed to evaluate the effect of a SAM coating. These calculations ignore adhesion and use the same geometry as that shown in Fig. 3.2. The OTS-SAM coating is assumed to be an isotropic, linear-elastic material (undoubtedly an oversimplification), and a range of polymer-like Young's modulus, E_c, is considered (coating Poisson's ratio, ν_c, is fixed at 0.4). Figure 3.3 indicates that the SAM coating has a significant effect on contact; it reduces contact pressure and increases contact area. Consequently, any finite element contact analysis must explicitly include the relatively compliant SAM coating. The effect of adhesion was considered next. Results for 3 adhesion levels are plotted in Fig. 3.4 for a 2-nm thick SAM coating (E_c = 8 GPa, ν_c = 0.4). Interestingly, even when a relatively compliant coating is present, the results are DMT-like: using an effective load $P + 2\pi RW$ collapses the results (Fig. 3.5). This greatly simplifies the required analysis since one does not need to perform separate calculations for each adhesion level of interest; adhesion can be taken into account simply through the effective load.

What is required is a relationship between friction force and effective load in terms of the two free parameters, W and τ^*. Note, however, that friction force is equal to the product of contact area and τ^*, which is assumed to be a constant for a given pair of surfaces. Consequently, the finite element contact analysis only needs to determine the relationship between contact area and applied load. This must be done for each combination of SAM and asperity material properties (e.g., various E_c) and geometric parameters (e.g., R and SAM layer thickness, h_c) of interest. Figure 3.6 shows the

calculated relationship for one set of such properties: a 27-nm radius of curvature silicon tip indenting a 2-nm thick SAM coating on a silicon substrate with E_c = 8 GPa, ν_c = 0.4. For the range of applied loads relevant to our AFM friction tests, the contact area vs. applied load relationship can be fit quite well by a simple power-law relation. Using this fact, and based upon nondimensional considerations, the following relationship was determined

$$\text{Friction Force} = \tau^* \pi \left(\frac{3PR\left(1+\frac{\overline{E}}{\overline{E}_c}\right)}{4\overline{E}} \right)^{2/3} A\left(\frac{P}{\overline{E}_c h_c^2}\right)^b \qquad (3.1)$$

where $\overline{E} = E/(1-\nu^2)$ and $\overline{E}_c = E_c/(1-\nu_c^{\,2})$. The parameters A and b have been determined from a series of finite element calculations, and depend on elastic and geometric properties. See Appendix B for further details. Table 3.1 lists current estimated values for these parameters. Note that these parameters are thought to be applicable when h_c/R values between 0.057 and 0.074, for $P/\overline{E}_c h_c^2$ values between 0.02 and about 2, and for ν = 0.23 and ν_c = 0.4.

Table 3.1. Parameters used in Friction Force vs. Applied Load relationship (Eq. 3.1)

E_c/E	*A*	*b*
0.014	0.65	-0.11
0.028	0.66	-0.11
0.056	0.66	-0.09
0.112	0.73	-0.08

Figure 3.7 demonstrates the use of the Friction Force vs. Applied Load relationship (Eq. 3.1) to determine the τ^* and W values corresponding to two different sets of AFM friction test data. As an aside, the plotted experimental results are for two nominally identical tests, indicating current issues with day-to-day variability in AFM-friction test data (see Appendix C for more details on the AFM-testing along with preliminary test results). The analytic relation closely matches the experimental data for the indicated τ^* and W values. These fits assume E_c = 8 GPa. It must be emphasized that the fits assume that the values of R, h_c, E, ν, E_c, and ν_c are independently known. There are any number of equally good fits when the ratio $\tau^*/E_c^{2/3}$ is held fixed (follows from Eq. 3.1 and the fact that A and b are a weak function of E/E_c for the range of values considered, Table 3.1). This presents some difficulty since E_c, and ν_c are difficult to measure. There are some potential approaches for experimentally determining E_c, but these are difficult measurements [3.3]. One may also be able to make estimates of SAM properties from the results of molecular dynamic simulations of SAMs [3.6].

3.4. Generating finite element meshes from AFM images

One further aspect of the asperity-level modeling effort is the development of an automated method for generating a finite element mesh directly from an AFM image. A finite element mesh script was developed which takes surface height information in the form of a matrix and creates an interpolated sheet body that can be operated on in a finite element meshing package such as CUBIT. The script accepts user arguments that define the number of pixels in each planar direction and the physical size of the pixelized scan in each planar direction. After assigning each pixel a physical location, a spline is fit to each line of pixels in one coordinate direction. Then a spline is fit to each line of pixels in the orthogonal direction. The intersecting mesh of spline fit lines is used to generate an interpolated two-dimensional representation of the AFM scan height profile.

3.5. Illustrative example

A demonstration of the capabilities of PRESTO and the Junction Model will be described in this section. PRESTO was used to predict the friction force generated when an asperity slides over a portion of a surface whose topography was defined by an AFM image. Comparisons are also made for the cases of simulated silicon-on-silicon contact and silicon-on-SAM. In this instance, the SAM layer is a CH_3-thiol with an experimentally calculated junction strength of $\tau^* \approx 194$ MPa, elastic modulus E = 8 GPa, and Poisson's ratio $\nu = 0.4$.

In order to capture Hertzian contact mechanics and still have a finite element problem that was tenable, only a portion of a full 10 μm x 10 μm AFM scan was sampled for use as the substrate over which a spherical asperity is displaced. A 100 nm x 100 nm region of the full image was sampled and the surface topography was interpolated within CUBIT using the script described in the previous section. From this region, a 35 nm x 100 nm track was sampled to serve as a representative portion of the image. A spherical asperity with radius of curvature of 50 nm was created. From this sphere a die was removed such that its width was completely contained within the width of the track. A representative mesh of this geometry is shown in Fig. 3.8. The figure shows the mesh employed in analysis. The mesh consists of approximately 250,000 elements and the elements in the contacting surfaces are no larger than 0.5 nm x 0.5 nm in the plane of contact. The die was pressed into the substrate with a force of 500 nN and then slide tangentially across the surface at a rate of approximately 7.5 m/s.

Because a transient dynamics code was employed in the analysis, silent boundary conditions were employed to allow stress waves to pass freely through the free surfaces. The substrate and asperity were therefore essentially infinite bodies and the impact of boundaries in the near vicinity of the contacting surfaces was minimized. Figure 3.9 shows the results of a set of simulations using the geometry pictured in Figure 3.8. The figure shows how the contact radius evolves as a function of the position of the die as it slides over the substrate. It is clear that local features of the substrate will strongly dictate the calculated contact radius. The information given in this figure for the SAM-coated substrate was calculated using values for shear force as a function of position that were

provided directly from the finite element simulation. The contact radius value was calculated directly using the junction strength of silicon-on-SAM. The contact radius for silicon-on-silicon simulation was approximated through a discrete interrogation of the local element contact forces. It is interesting to note that the much compliant SAM-layer yields a substantially higher contact radius as would be expected

3.6 References

3.1. J.R. Koteras and A.S. Gullerud, *Presto User's Guide Version 1.05 (SAND2003-1089)*. 2003, Sandia National Laboratories: Albuquerque, NM.

3.2. A.R. Burns, et al., *Molecular Level Friction as Revealed with a Novel Scanning Probe.* Langmuir, 1999. **15**: p. 2922-2930.

3.3. R.W. Carpick, et al., *Making, Breaking and Sliding of Nanometer-Scale Contacts.* Material Research Society Symposium Proceedings, 1999. **539**: p. 93-103.

3.4. K.H. Brown, et al., *ACME: Algorithms for Contact in a Multiphysics Environment API version 1.3 (SAND2003-1470)*. 2003, Sandia National Laboratories: Albuquerque, NM.

3.5. D. Maugis, *Contact, Adhesion and Rupture of Elastic Solids*. Solid-State Sciences, ed. H. Strormer. 2000, Berlin: Springer.

3.6. M. Chandross, G.S. Grest, and M.J. Stevens, *Friction between Alkylsilane Monolayers: Molecular Simulation of Ordered Monolayers.* Langmuir, 2002. **18**: p. 8392-8399.

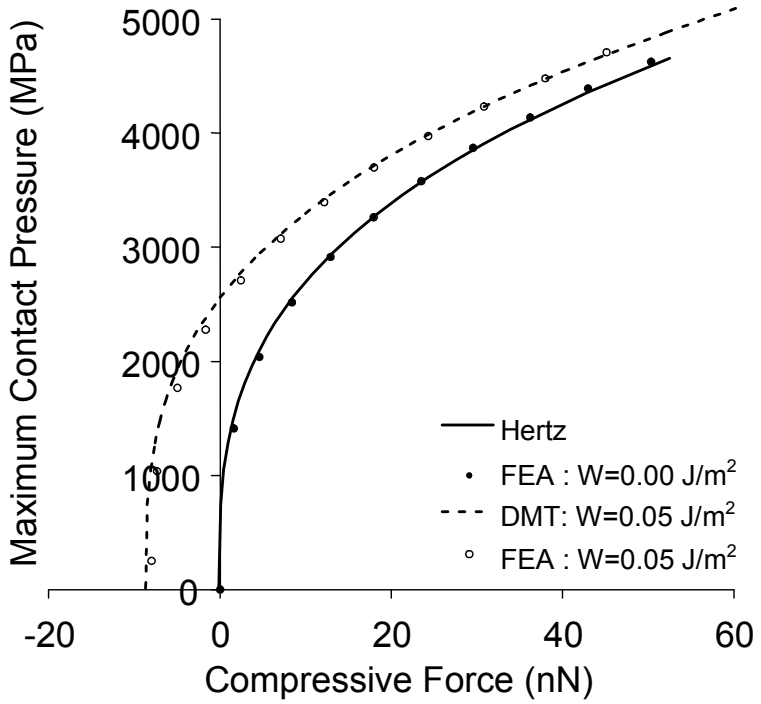

Fig. 3.1. PRESTO finite element analysis (FEA) solutions compared with analytic Hertz (no adhesion) and DMT (W=0.05 J/m^2) solutions.

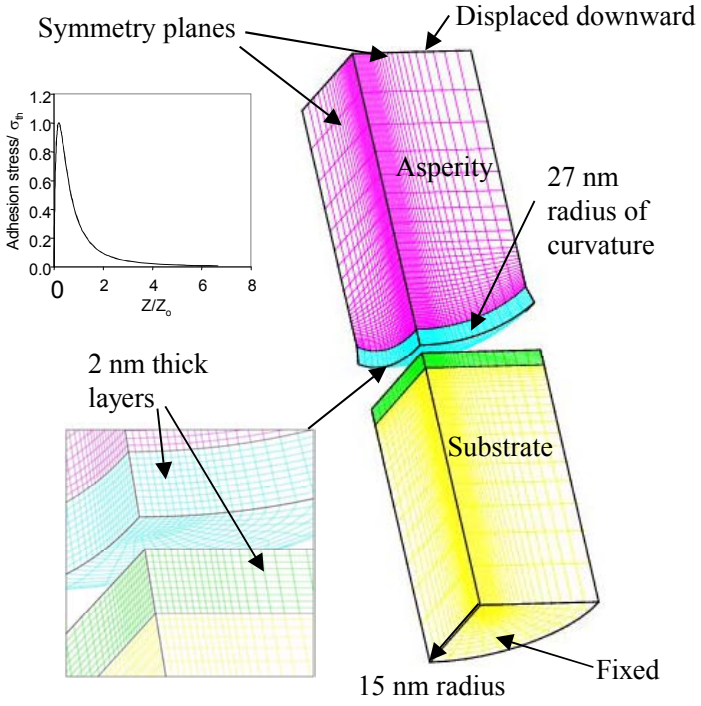

Fig. 3.2. Example of the finite element mesh used in PRESTO simulations of a cylindrical asperity with a truncated spherical tip contacting the flat surface of a cylindrical substrate.

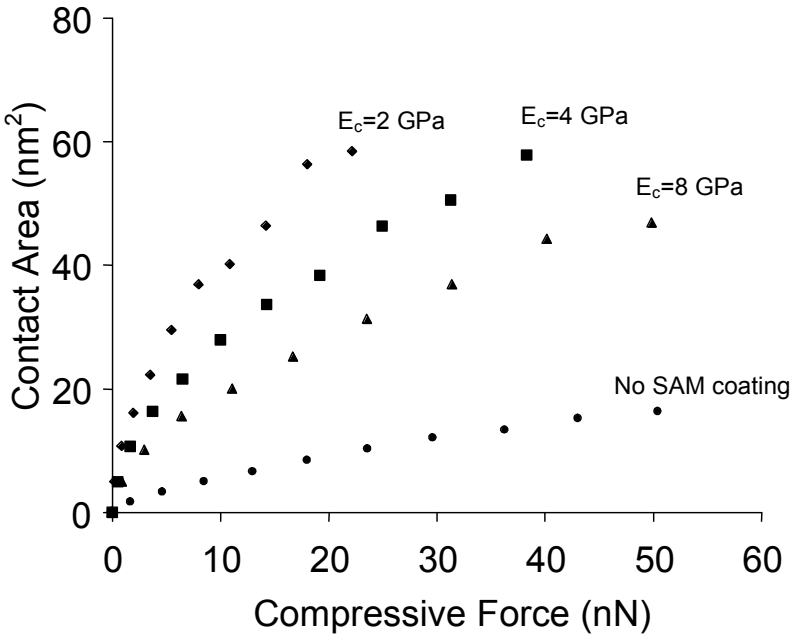

Fig. 3.3. Calculated contact area as a function of the SAM's Young's modulus for a 27-nm radius of curvature silicon tip indenting a 2-nm thick SAM coating on a silicon substrate (ν_c = 0.4).

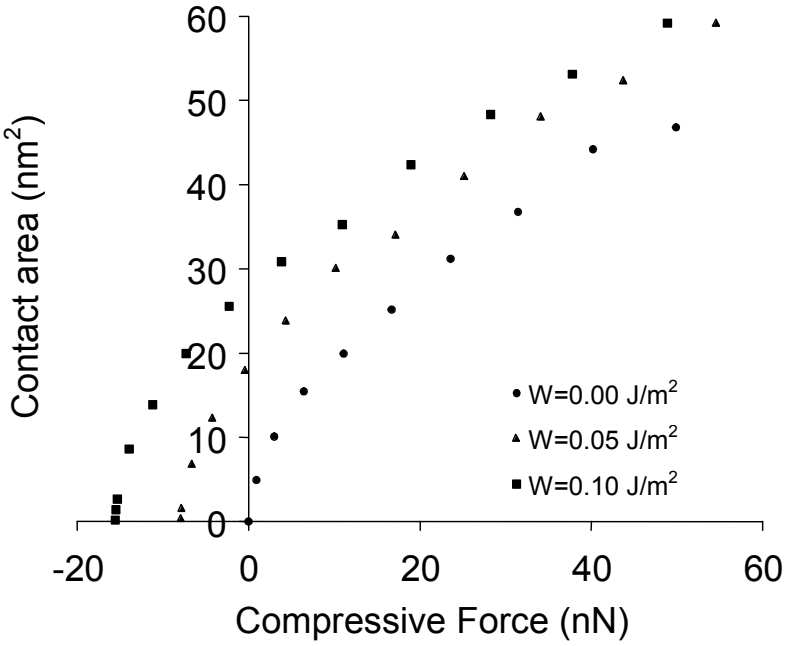

Fig. 3.4. Calculated contact area as a function of the work of adhesion, W, for a 27-nm radius of curvature silicon tip indenting a 2-nm thick SAM-coated silicon substrate (E_c = 8 GPa, ν_c = 0.4).

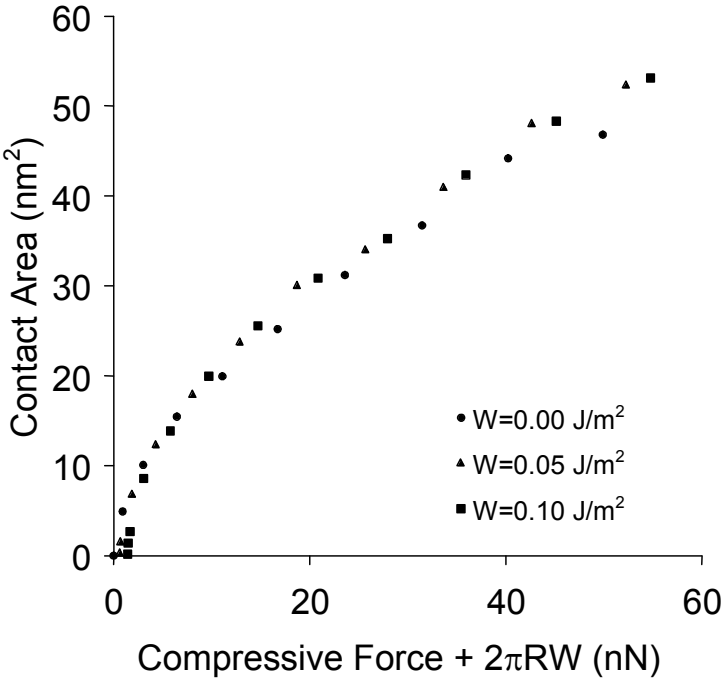

Fig. 3.5. Calculated contact area as a function of the DMT-like effective load for a 27-nm radius of curvature silicon tip indenting a 2-nm thick SAM coating on a silicon substrate (E_c = 8 GPa, ν_c = 0.4).

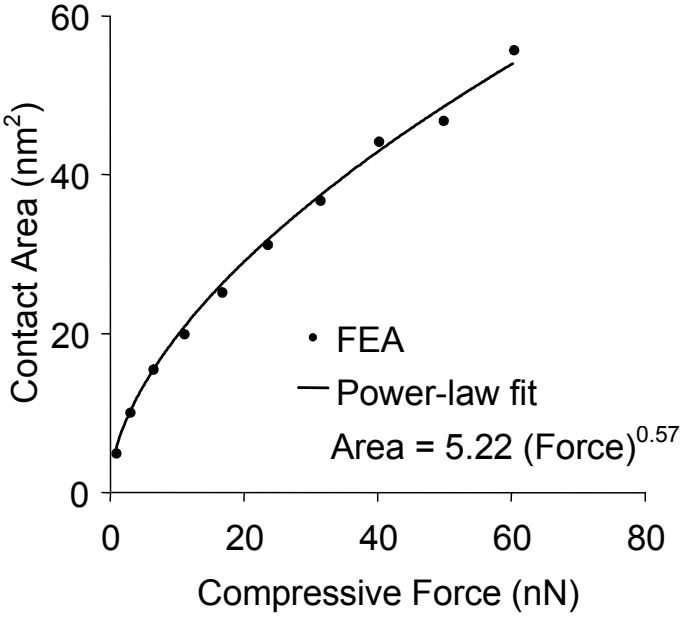

Fig. 3.6. Power-law fit of the calculated contact area vs. effective compressive force for a 27-nm radius of curvature silicon tip indenting a 2-nm thick SAM coating on a silicon substrate (E_c = 8 GPa, ν_c = 0.4).

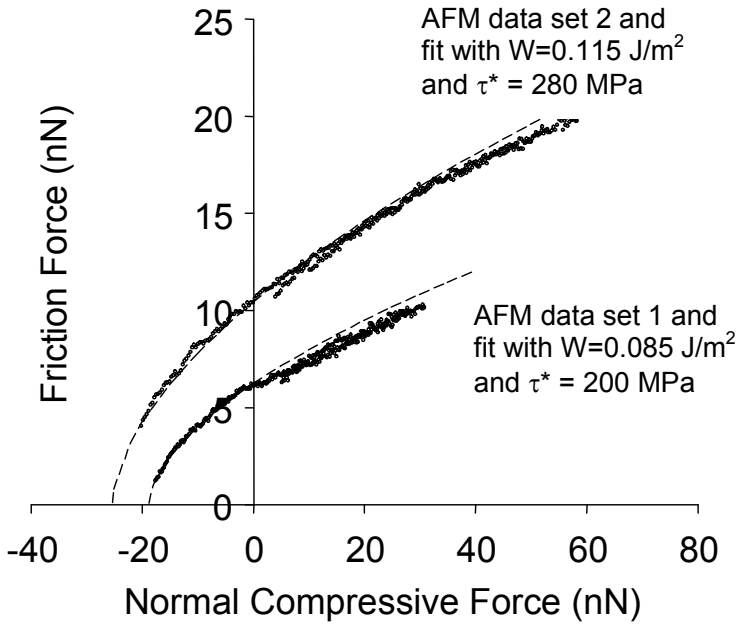

Fig. 3.7. Values of work of adhesion, W, and shear junction strength, τ*, parameters in the analytic relationship for Friction vs. Normal Force that produce a good fit to AFM friction test data (E_c = 8 GPa, ν_c = 0.4)

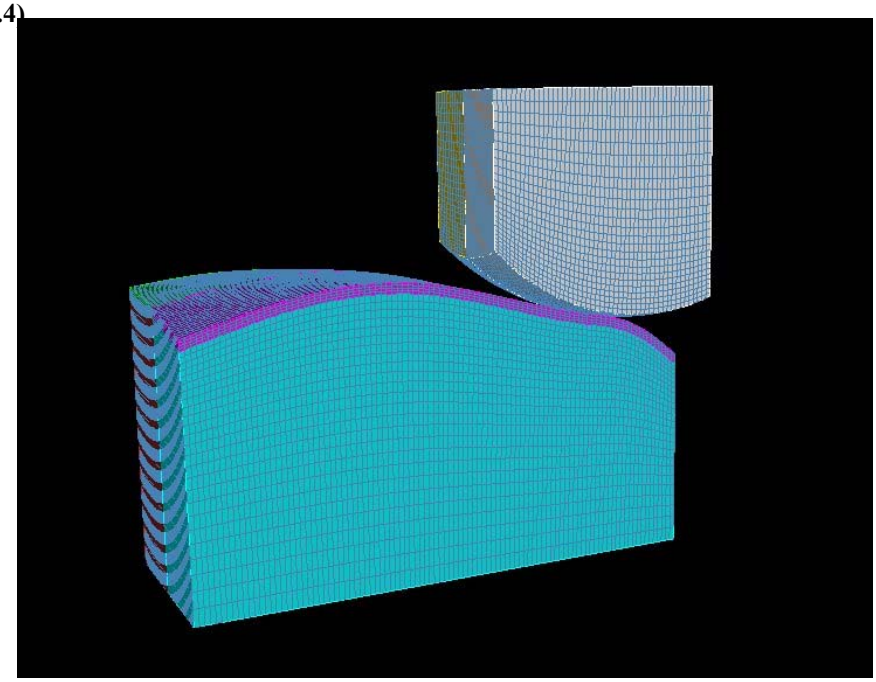

Fig. 3.8. Mesh of a 35 nm x 100 nm track sampled from an AFM scan of a polysilicon surface. The substrate is covered with a CH_3-thiol SAM layer 2 nm in thickness. A spherical asperity with 50 nm radius of curvature is pressed into the substrate and displaced along its length.

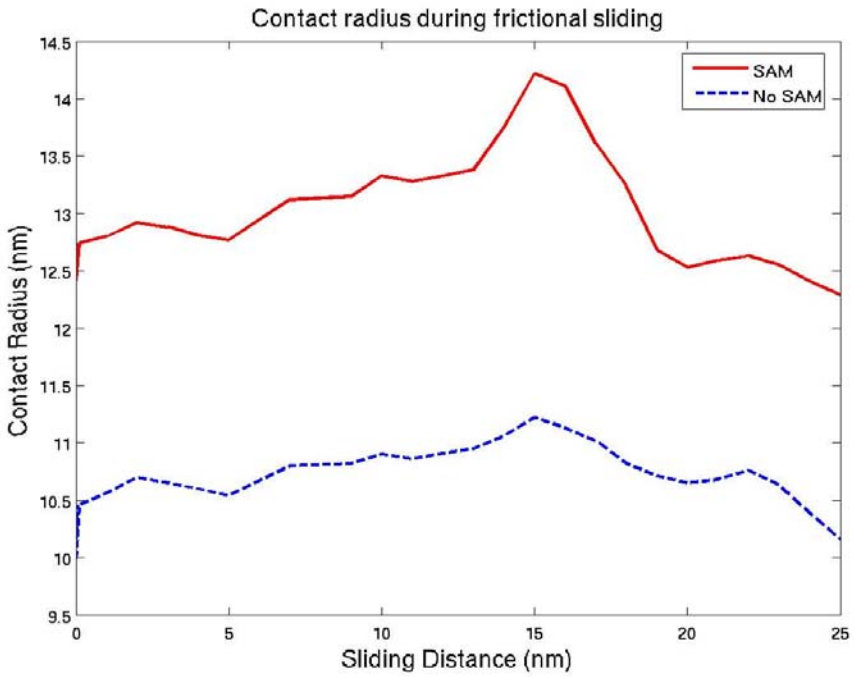

Fig. 3.9. The friction force calculated using the junction model for the geometry pictured in Figure 3.8 is shown as a function of sliding location.

4. Grid-scale Friction Model for Polysilicon MEMS

4.1 Background

Section 3 described our efforts to perform detailed asperity-level simulations in which asperities are modeled explicitly. When analyzing MEMS components, however, one would like to mesh nominally flat surfaces and then include the effect of roughness by using homogenized contact and friction models that depend only on a few input parameters. This is the motivation for the work presented in the present section. This section begins with a description of a detailed AFM characterization of polysilicon surface topography for surfaces with different nominal roughness. This data is then used to determine statistical information for input into the classical Greenwood and Williamson model for multi-asperity contacts. Extensions of the Greenwood and Williamson model are also discussed: one incorporates the effect of adhesion while the other modifies the theory so that it applies to the case of relatively few contacting asperities.

4.2 Polysilicon Surface Roughness

Surface roughness is a critical parameter that affects the frictional and wear properties of bulk materials [4.1]. Because of the planar deposition technology, horizontal (*i.e.* as-deposited or annealed) polysilicon surfaces are quite smooth, with typical root mean square (RMS) surface roughness values of just a few nanometers. If surface textures are properly tailored and pressures are well controlled, it is conceivable that deformations will be largely elastic, and hence wear can be minimized. On the other hand, polysilicon asperities are highly curved, and so it may be difficult to avoid locally exceeding the hardness of polysilicon, 11 GPa [4.2]. Although surface roughness in MEMS has been discussed to some extent [4.3], until our work, no other studies have integrated detailed topography measurements of MEMS surfaces to model true pressures.

To address this, MEMS surfaces were studied with AFM to evaluate their geometry in detail. The surface topography was measured using a Digital Instruments Nanoscope IV AFM with a silicon nitride AFM cantilever. The tip shape was tested before and after the measurements using *in-situ* tip imaging samples to ensure that it started and remained a sharp, single protrusion so as to minimize the effect of convolution of tip shape [4.4]. Numerous tips with blunt (>40 nm curvature radius), multiple, or asymmetric terminations were rejected.

We used existing MEMS cantilever structures as samples to study the surface roughness. Such samples consist of the same surfaces that are used in MEMS test structure friction studies, but could be fabricated in a much shorter time. Those surfaces are the top of a lower lying ground plane polysilicon, and the bottom of an upper polysilicon cantilever. The cantilevers were fabricated according to a three mask level

process. Texturing of the lower layer of polysilicon (300 nm thickness, called "Poly0") was accomplished by thermal oxidation in dry O_2 at 900 °C for increasing times. Table 4.1 indicates the times and the RMS roughness as measured by several 10x10 μm^2 AFM images of the samples. The texturing occurs because the grains are randomly oriented, and dry oxidation in the linear regime proceeds at different rates on different orientations of silicon [4.5]. Also, the grain boundaries are enhanced at increasing oxidation times, giving rise to grooves. These do not contribute significantly to the desired texturing because they comprise a small percentage of the surface area, and extend below the surface. A wet chemical etching process whereby the oxide is removed follows the oxidation step, exposing the textured surfaces.

Standard deposition, lithography and etch techniques were used to fabricate the cantilevers, to form the upper layer of polysilicon (2500 nm thickness, called "Poly 1/2"). They are supported on one side by a step-up support post, formed by filling a hole etched into the sacrificial oxide layer. A critical step is the release and drying of the cantilevers. We used two procedures: (1) supercritical carbon dioxide drying [4.6], and (2) a solvent-based coating in which a self-assembled monolayer of perfluorodecyltrichlorosilane (FDTS, $C_8F_{17}C_2H_4SiCl_3$) is applied, similar to ref. [4.7]. Surfaces produced using both types of finishing steps were examined and unless otherwise noted, results did not exhibit any significant dependence on the choice of release and drying procedure.

For measurements of Poly0 regions, the AFM tip was positioned over an exposed Poly0 region. Beams were then peeled off using an adhesive and placed facing underside up on an AFM sample holder to examine the underside of the Poly1/2 cantilever beams. Figs. 4.1 and 4.2 are topographic AFM images of the Poly0 layer for the two extreme cases of no oxidation and 400 minutes of oxidation respectively. Dark/bright correspond to low/high regions. The grain boundaries are clearly seen and reveal that the grains typically range in size from 50-500 nm laterally, with irregular boundaries. The oxidized sample exhibits deeper, wider grain boundaries as expected. The tops of grains have some intrinsic roughness, but overall roughness results from height differences between the grains, particularly for the oxidized sample.

The height range of the tops of the grains is approximately 30 nm for the unoxidized sample and 80 nm for the oxidized sample. To characterize this more generally, the RMS roughness R_q was measured at different length scales for all four oxidation times (Table 4.1). For a 10x10 μm^2 area, R_q depends nearly linearly on oxidation time, indicating the roughening effect of the oxidation and etching process. However, at the 100x100 nm^2 scale with roughness measured on top of an individual grain, R_q had no dependence on oxidation time, being ~0.8 nm. The highest grains will obviously be the ones that first come into contact with the countersurface, although if wear occurs, lower grains may eventually come into contact. Therefore, we measured the intragranular roughness on both high and low grains to check for any changes as a function of grain height. Three of the

Table 4.1

Oxidation Time (min)	RMS Roughness (nm)
0	3.06
20	5.11
136	6.72
400	11.5

highest and lowest grains were selected from the sample oxidized for 400 minutes to examine the extreme case. For each grain a series of images was acquired and roughness measurements carried out. The roughness was measured to be 0.75±0.12 nm and 0.87±0.39 nm for the highest and lowest grains respectively, where the error is given by the standard deviation of the measurements. Therefore, within error, the roughness on high and low grains is indistinguishable. The Poly1/2 layers were observed to have substantially different topographic features. Figs. 4.3 and 4.4 are topographic AFM images of the Poly1/2 underside, again for the two extreme cases of no oxidation and 400 minutes of oxidation respectively. The topography consists of two predominant features: small grains that are apparently the intrinsic grain structure of the Poly1/2, and larger pits that appear to be a result of a conformal growth process. The pronounced nature of these latter features was not expected. The Poly0 grain roughness has been partially transferred through the sacrificial oxide, upon which the Poly1/2 layer was grown. Consistent with this, the pits in the Poly1/2 layer become larger with increasing oxidation time as seen by comparing Figs. 4.3 and 4.4. As well, the pits are seen to have a distribution that is similar in nature to the grain height distribution seen in Figs. 4.1 and 4.2 respectively. The pits in the Poly1/2 surface are more rounded than the grains of the Poly0 surface, which is a natural consequence of the expected reduction in feature definition that would occur when the oxide is grown on the Poly0. The underside of the cantilevers is therefore quasi-conformal with the Poly0, with these quasi-conformal surfaces separated by a 2-μm gap.

4.3 Discrete GW model and application to AFM images

In treating contacting rough surfaces in a computationally efficient manner, the classical method described by Greenwood and Williamson [4.8] is quite attractive as a homogenization technique. Essentially, if there are enough contact asperities to define an asperity density and the population is spatially sparse enough to act independently then their response to normal displacement can be given by a GW model. Specifically, the individual asperity's force response, f, can be integrated over the contacting sub-population of the asperity height distribution, $\phi(h)$, to obtain a normal pressure value, $p(d)$, over a nominal area, A:

$$p(d) = \frac{1}{A} \int f(h-d)\phi(h)dh, \tag{4.1}$$

as a function of the nominal gap, d, or approach of the two surfaces (Fig. 4.5). In a similar manner, true area of contact for the ensemble can be calculated from the response of a single asperity, $a(d)$, to contact with an approaching surface, for example. If the assumptions embedded in the model are valid then all that is required to simulate the contact of rough surfaces on the MEMS component is a representative characterization of the distribution, $\phi(h)$, and the individual asperity response. No other spatial information is required.

Besides the basic difficulty of identifying "asperities" from surface data, the assumption that the distribution is populous enough to be continuous breaks down in typical MEMS devices, where the (nominal) area of contact and/or nominal pressure are small. This can also happen if there are a few tall asperities that dominate contact and

show up as "outliers" in the measured asperity height distribution. In these cases, the discrete nature of the contacting population is apparent and the preceding expression becomes:

$$p(d) = \frac{1}{A}\sum_i f(h_i - d). \tag{4.2}$$

Figure 4.6 illustrates that as the sample population of a Gaussian $\phi(h)$ grows, the response, in this case the (non-dimensional) real area of contact versus the (non-dimensional) pressure, tends to the response of a continuous distribution of asperities (the uppermost curve) and away from the response of a single asperity (the lowest curve). Here it takes only takes tens to hundreds of *contacting* asperities for the discrete results to start to match the continuous one. This figure also supports the common belief that the GW model is consistent with Coulomb's law. Specifically, the nearly linear relationship between real contact area, A_c, and pressure shown in the figure, with the assumption that each asperity can only support a shear force proportional to its contact area, leads to the simple relationship:

$$\tau = kA_c(p) = \mu p, \tag{4.3}$$

known as Coulomb's law. Here the asperities are assumed to behave in a Hertzian manner:

$$f = \frac{4}{3}E\sqrt{R}d^{\frac{3}{2}} \quad \text{and} \quad a = \pi R d, \tag{4.4}$$

where E is an elastic modulus and the radius of curvature, R, is assumed to be the same for all the asperities. Note that in the figures the contact area is non-dimensionalized by $\pi R\sigma N$ and that the normal force is non-dimensionalized by $\frac{4}{3}E\sqrt{R}\sigma^{3/2}N$, where N is the total number of asperities in the nominal contact area and σ is a characteristic length for the distribution $\phi(h)$, i.e., the standard deviation.

We have applied the GW model to the MEMS surface topographies presented in Section 4.1 as an example of applying the most basic assumptions of rough contact. The surfaces shown in Figs. 4.1-4.4 are the two faces that will come into contact when the cantilever makes contact with the surface underneath, such as in an adhesion or friction test. To carry out this analysis we follow the treatment of McCool [4.9], who showed how to convert surface topographic measurements to appropriate input parameters for the GW model (as modified by Nayak [4.10]).

As stated above, the GW model assumes that the surface is composed of spheres with a random (Gaussian) distribution of summit heights but with a common radius. This is pushed into contact with a rigid flat surface and the number of contacts, total contact area, total load and asperity pressure ranges (including the fraction of asperities beyond a yield pressure) are calculated. However, some adjustments to the GW model are required. Longuet-Higgins [4.11] showed that for a Gaussian distribution of *surface* heights, the distribution of *summit* heights is not itself Gaussian. Furthermore, the curvature of higher

summits is generally higher (*i.e.* sharper) than for lower summits. Nayak [4.10] provided a model that takes these factors into account including the fact that asperities may be elliptical in nature. Finally, having both surfaces be rough and elastic instead of just one can be taken into account by simply adding the spectral moments of both surfaces together [4.9, 4.12]. The effect of all these corrections is succinctly described by McCool [4.9]. To summarize, the analysis requires calculation of the three spectral moments of the surface topograph *z(x,y)* as follows:

$$m_0 = \langle z^2 \rangle,\ m_2 = \left\langle \frac{dz}{dx} \right\rangle,\ m_4 = \left\langle \frac{d^2 z}{dx^2} \right\rangle \tag{4.5}$$

where x is an arbitrary direction and $\langle\ \rangle$ denotes a statistical average. m_0 is the mean square surface height, and so the RMS roughness $R_q = \sqrt{m_0}$. From this one calculates the "bandwidth parameter" $\alpha = m_0 m_4 / {m_2}^2$, which is related to the asperity density. The true contact area A_c and total load P with respect to the apparent contact area A_0 are calculated from the following equations provided by McCool [4.9]:

$$\frac{A_c}{A_0} = 0.0640(\alpha - 0.8968)^{1/2} \cdot F_1\left(\frac{d}{\sigma_s}\right) \tag{4.6}$$

$$\frac{P}{A_0} = 0.0333 E^* {m_2}^{1/2} (\alpha - 0.8968)^{3/4} \cdot F_{3/2}\left(\frac{d}{\sigma_s}\right) \tag{4.7}$$

where

$$E^* = \left(\frac{1-\nu_1^2}{E_1} + \frac{1-\nu_2^2}{E_2} \right)^{-1} \tag{4.8}$$

is a combination of the Poisson's ratios and Young's moduli of the two surfaces. For the calculations we use E=164 GPa and ν=0.23 for the two polysilicon surfaces. As well,

$$F_n(t) = \frac{1}{\sqrt{2\pi}} \int_t^\infty (x-t)^n e^{-x^2/2} dx\ . \tag{4.9}$$

which comes about from integrating the various quantities in the Hertz theory of contact over a Gaussian height distribution. The ratio d/σ_s is the summit mean plane separation d divided by the RMS summit height variation σ_s. As the surfaces approach, d decreases. With the adjustments made above, McCool [4.9] asserts that the GW formalism should provide at least an order of magnitude estimate, if not better, for a wide range of rough surfaces.

In order to evaluate the spectral moments from our images, the following procedure was used. Images were recorded with at least 256 x 256 pixel resolution. Using SPM32 software from RHK Technology (Troy, MI) the RMS value was calculated and then

squared to provide the value of m_0. Each image was then expanded to 1024x1024 pixels with the new pixel values calculated by interpolation. This reduced the amount of errors in derivative images that are inherently generated due to pixelation and noise. To reduce errors due to noise fluctuations, the images were smoothed using a modest pair of median filtering and smoothing algorithms. The median filter takes high and low pixel values and replaces them with the median value of neighboring pixels. After this step the image is smoothed using a two-dimensional weighted average of the adjacent pixels. The first and second derivatives of the image with respect to the scan direction were then calculated from this expanded smoothed image, and the RMS values of these derivative images were found. The square of these RMS values provided the values of m_2 and m_4 respectively. The above formulae were then used to predict the properties of these MEMS surfaces in contact. 10 x 10 μm^2 images were chosen for this analysis as they provided a larger sample size of the features. For the calculations, we imposed a surface separation equal to one standard deviation of the combined summit height distribution σ_s. This was chosen to ensure that the calculations represented a substantial but not severe interaction between the surfaces, and it should be noted that this value is different for the two interfaces.

Table 4.2

Parameter (units)	**Unoxidized sample**	**Maximally oxidized sample**
summit density (/μm^2)	4510	4160
average summit radius (nm)	2320	806
σ_s, standard deviation of summit height distribution (nm)	0.173	1.62
number of contact points for a 10x100 μm^2 cantilever	1.53×10^5	4.24×10^4
ratio of true to apparent contact area	0.031	0.0065
true contact area for a 10x100 μm^2 cantilever (μm^2)	30.7	6.48
load for a 10x100 μm^2 cantilever (mN)	15.1	8.23
average contact pressure (MPa)	493	1270

The results are summarized in Table 4.2. All values here were calculated from the GW analysis. We see a strong contrast between the unoxidized and maximally oxidized surfaces. The oxidation produces rougher surfaces, yet there are slightly fewer summits per unit area. This is likely a result of the increased size of the grain boundaries. The average summit radius is smaller by a factor of ~3 for the roughened surfaces. These values are averages of all summits, and are clearly much larger than the smallest asperities present on the

surface. Therefore, it is likely that this simulation will underestimate the fraction of plastically deformed asperities.

The roughened surfaces show nearly an order of magnitude larger standard deviation in summit heights. In combination with the smaller summit density, this leads to a smaller contact point density by a factor of three. The ratio of true to apparent contact area is small for both interfaces, which is a typical and important result for rough surfaces. As expected, the roughening leads to a much smaller contact area fraction, by about a factor of 5 compared with no roughening.

For the separations imposed, the unoxidized surface supports more load. This is simply due to the fact that the contact area is higher for the given separation. More importantly, the average contact pressure, despite the lower load, is nearly three times higher for the roughened interface. This is due to the fact that the asperities are smaller. The average pressure is significant, and suggests that in combination with shear stresses (which are not considered in this model), wear of the asperities is likely for both cases, but far more likely for the roughened interfaces. Using a hardness of 11 GPa for silicon [4.2], the model predicts vanishingly small fractions of "plastically" deformed asperities. We believe this is an underestimate due to the aforementioned averaging of the asperity radius.

4.4 Model incorporating adhesion

The first basic phenomenon that distinguishes MEMS-scale friction from macroscopic tribological behavior is the effects of adhesion are significant and apparent. As results in Section 3.3 have shown, the assumed adhesion behavior is more DMT-like, i.e. diffuse adhesion with stiff elastic bodies, than JKR-like, i.e. concentrated adhesion regions on relatively soft elastic bodies. With this in hand, the appropriate extension of GW's original model [4.13] involves another term

$$p(d) = \frac{1}{A}\int \frac{4}{3} E\sqrt{R}(h-d)^{\frac{3}{2}}\phi(h)dh + \frac{1}{A}\int 2\pi wR\phi(h)dh \qquad (4.10)$$

which is a direct result of the Deryaguin, Muller, Toporov (DMT) solution [4.14]

$$f = \frac{4}{3} E\sqrt{R}d^{\frac{3}{2}} + 2\pi wR. \qquad (4.11)$$

In this equation w is the characteristic work of adhesion. Since in the DMT solution area of contact has the same dependence on the displacement, d, the real area of contact, which is related to friction, is still given by the Hertzian result:

$$A(d) = \int \pi R(h-d)\phi(h)dh. \qquad (4.12)$$

The effective applied normal load is the only affected observable, as shown in Fig. 4.7, where the lower curve is a non-dimensionalized GW model with a Hertzian interaction and the upper curve is GW with a DMT interaction. This leads directly to the real contact area not going to zero as the *applied* normal load goes to zero. Hence the following graph (Fig. 4.8) shows that the ratio of the real area of contact (which is

proportional to the slipping limit of a force tangential to the surface) to the normal applied load becomes unbounded for the DMT based model (upper) versus the (nearly) constant value expected from Coulomb's law for the Hertz based model (lower). Using textbook values of the material properties of silicon (e.g. w = 0.1 J/m^2) and a 100 μm^2 sample area where the height distribution is nearly Gaussian with high outliers (see Fig. 4.9), Fig. 4.10 shows the small but significant effect of adhesion, which diminishes as more asperities come into contact. For coated asperities, the corresponding GW model is complicated by the fact that layer compliance affects the contact area, but the model follows in a similar fashion.

4.5 Thoughts on modeling PSTD

The second phenomenon that distinguishes the tribology of small devices is a significant pre-sliding tangential deflection (PSTD), whereas the Coulomb model has a sharp transition from stick to slip. It is possible to generate a GW-like model of friction that has a transition region due to changing populations of sticking and slipping asperities as the Fig. 4.11 demonstrates. Here, the upper curve is generated by a model based on a continuous distribution, and the lower curve from a model with a discrete distribution of asperities. Currently, however, the length-scale of this transition region is tied to roughness length-scale, whereas the observed PSTD events can be hundreds of times as large as the RMS roughness of the surfaces. Furthermore, from the direct simulations described in Section 2.1.9, it is clear that small asperity population and serendipitous alignment play a crucial role in the PSTD behavior seen in our devices. If there is truly a need to know details of geometry, then (deterministic) homogenization will fail to be predictive. If a clear mechanism can be identified perhaps progress can be made in this area. Even finding a characteristic length-scale to the PSTD events could lead to a simple phenomenological model with response similar to Fig. 4.11.

4.6 References

4.1. E. Rabinowicz, *Friction and Wear of Materials*. 2nd ed. 1995, New York: Wiley.

4.2. G.M. Pharr, W.C. Oliver, and D.R. Clarke, *New evidence for a pressure-induced phase-transformation during the indentation of silicon.* Journal of Materials Research, 1991. **6**(6): p. 1129.

4.3. K. Komvopoulos and W. Yan, *A fractal analysis of stiction in microelectromechanical systems.* Transactions of the ASME. Journal of Tribology, 1997. **119**(3): p. 391-400.

4.4. J.S. Villarrubia, *Morphological estimation of tip geometry for scanned probe microscopy.* Surface Science, 1994. **321**(3): p. 287-300.

4.5. S.M. Sze, ed. *VLSI Technology*. 1983, McGraw-Hill: New York.

4.6. G.T. Mulhern, D.S. Soane, and R.T. Howe. *Supercritical carbon dioxide drying of microstructures*. in *Proc. 7th Int. Conf. Solid-State Sensors and Actuators, Transducers '93*. 1993. Yokohama, Japan.

4.7. U. Srinivasan, et al., *Alkyltrichlorosilane-based self-assembled monolayer films for stiction reduction in silicon micromachines.* Journal of Microelectromechanical Systems, 1998. **7**(2): p. 252-60.

4.8. J.A. Greenwood and J.B.P. Williamson, *Contact of nominally flat surfaces.* Proc. Roy. Soc. Lond. A, 1966. **295**: p. 300.
4.9. J.I. McCool, *Comparison of models for the contact of rough surfaces.* Wear, 1986. **107**(1): p. 37-60.
4.10. P.R. Nayak, *Random process model of rough surfaces in plastic contact.* Wear, 1973. **26**(3): p. 305-33.
4.11. M.S. Longuet-Higgins, *The statistical analysis of a random, moving surface.* Phios. Trans. R. Soc. London, Ser. A, 1957. **249**: p. 321-387.
4.12. M. O'Callaghan and M.A. Cameron, *Static contact under load between nominally flat surfaces in which deformation is purely elastic.* Wear, 1976. **36**(79-97).
4.13. N.R. Tas, C. Gui, and M. Elwenspoek, *Static friction in elastic adhesion contacts in MEMS.* Journal of Adhesion Science and Technology, 2003. **17**(4): p. 547-61.
4.14. B.V. Derjaguin, V.M. Muller, and Y.P. Toporov, *Effect of contact deformations on the adhesion of particles.* J. Colloid Interface Sci., 1975. **53**(2): p. 314-26.

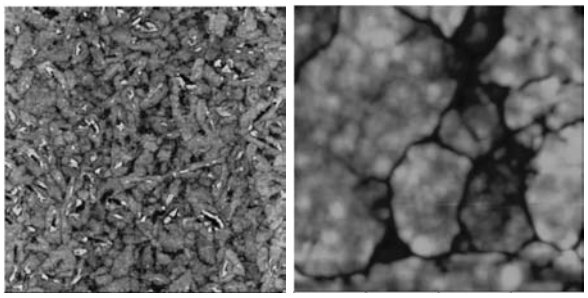

(a) (b)

Figure 4.1. 10 x 10 μm^2 (a) and 1 x 1 μm^2 (b) topographic images of the Poly0 surface. The z-height range is 35 and 20 nm, respectively.

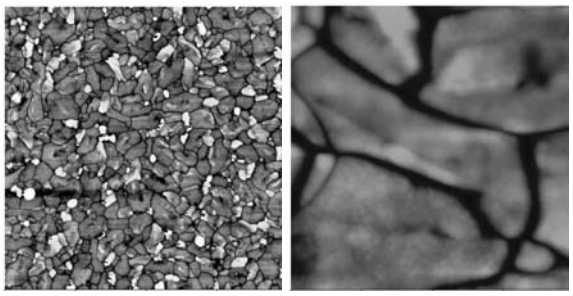

(a) (b)

Figure 4.2. 10 x 10 μm^2 (a) and 1 x 1 μm^2 (b) topographic images of the oxidized and etched Poly0 surface. The z-height ranges are 100 and 50 nm, respectively.

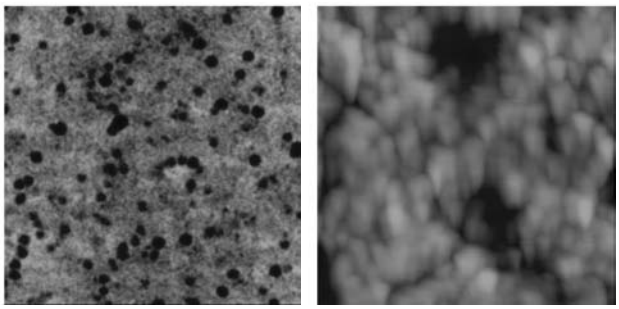

(a) (b)

Figure 4.3. 10 x 10 µm^2 (a) and 1 x 1 µm^2 (b) topographic images of the Poly1/2 surface counterpart to the unoxidized Poly0.

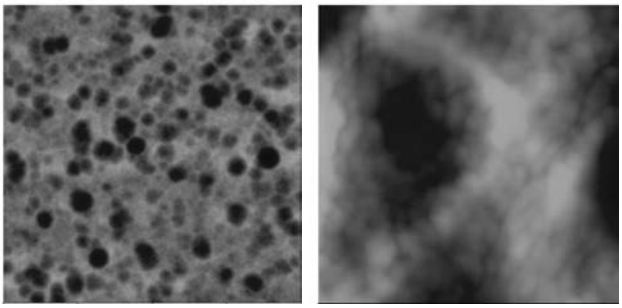

(a) (b)

Figure 4.4. 10 x 10 µm^2 (a) and 1 x 1 µm^2 (b) topographic images of the Poly1/2 surface counterpart to the oxidized and etched Poly0. The z-height ranges are 100 and 50 nm, respectively.

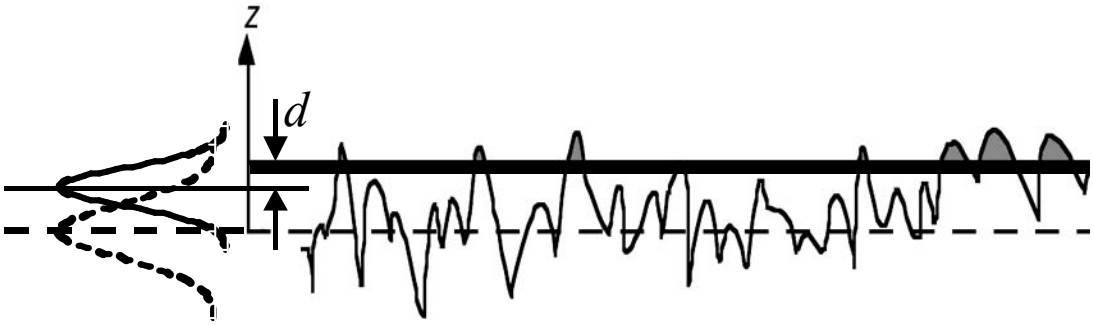

Figure 4.5. A rough surface (*z*-scale greatly exaggerated) with a flat rigid surface approaching from above (thick solid line). The undeformed surface is shown, where the shaded asperities would be deformed. At left is the height distribution function for the summits (solid line) and for the entire surface (dashed line). *d* represents the spacing between the summit mean plane and the approaching surface. The rigid surface is replaced by a rough deformable surface for our analysis.

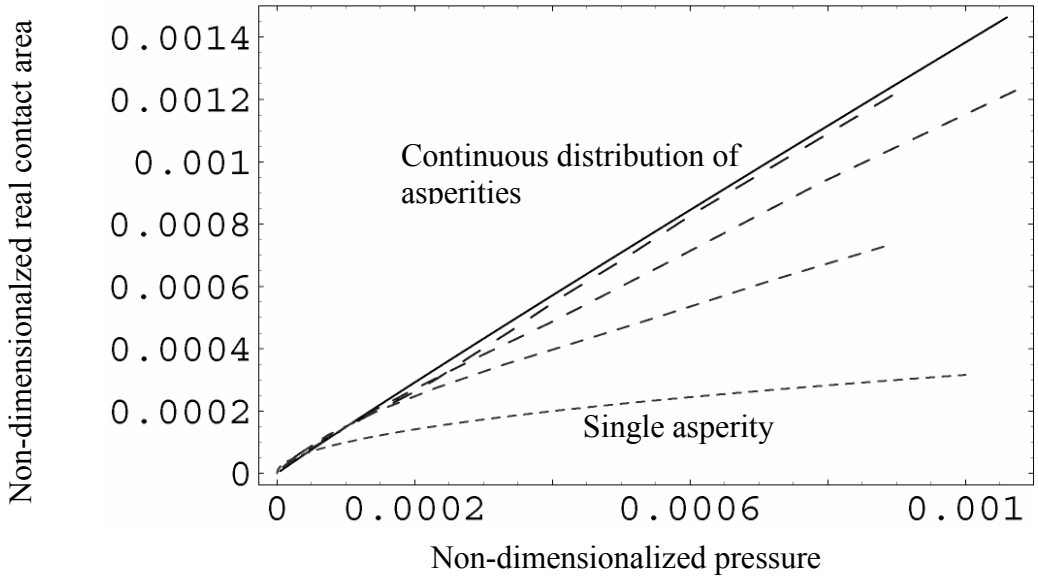

Figure 4.6. Non-dimensionalized real contact area vs. non-dimensionalized pressure.

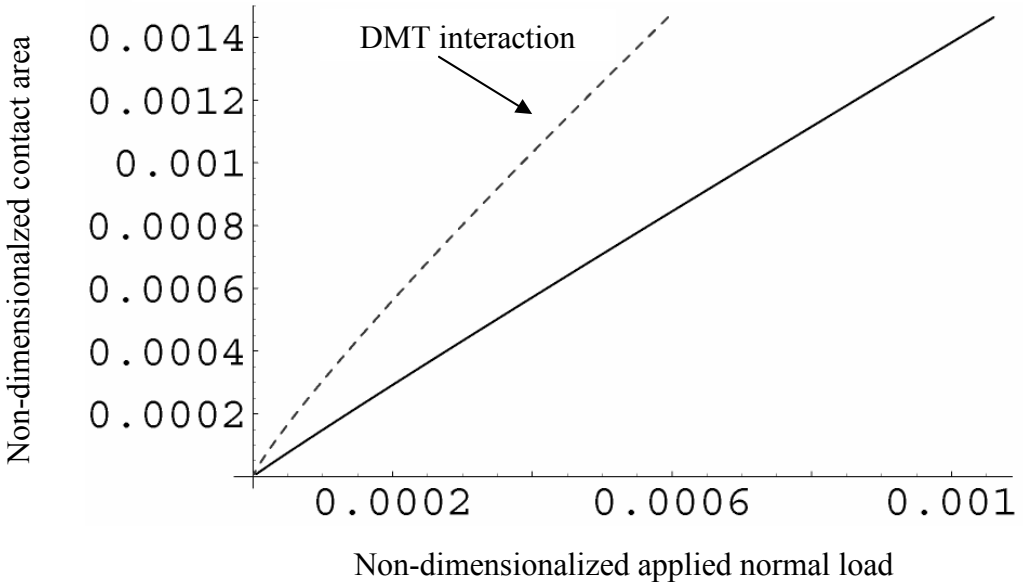

Figure 4.7. Non-dimensionalized contact area versus non-dimensionalized normal load.

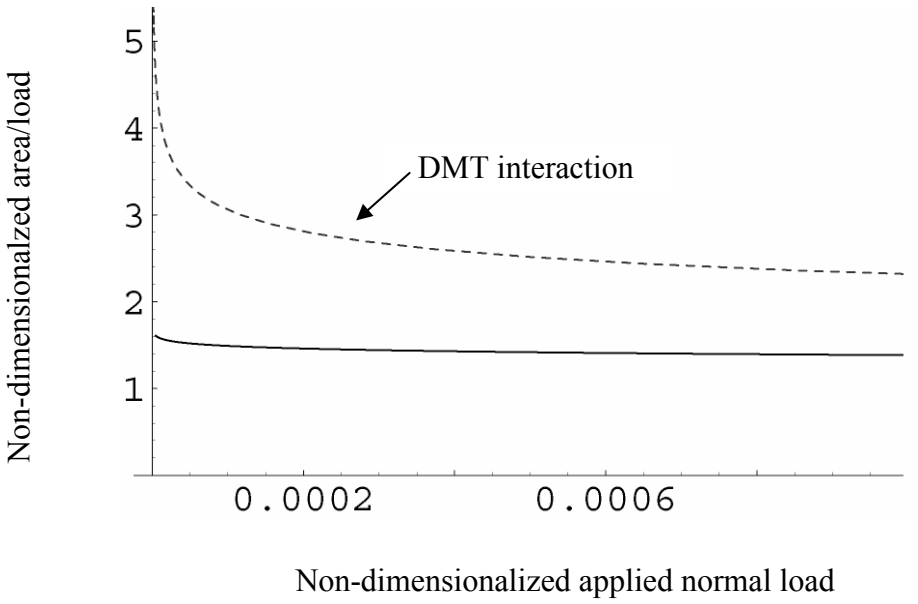

Figure 4.8. Non-dimensionalized area/load versus non-dimensionalized normal load.

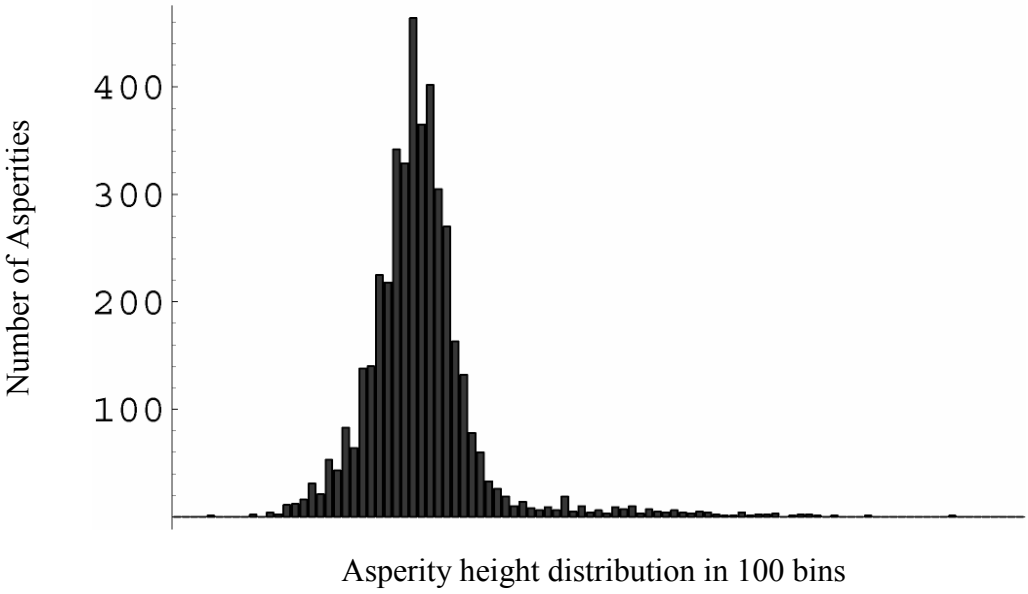

Figure 4.9. Height distribution sorted into 100 bins.

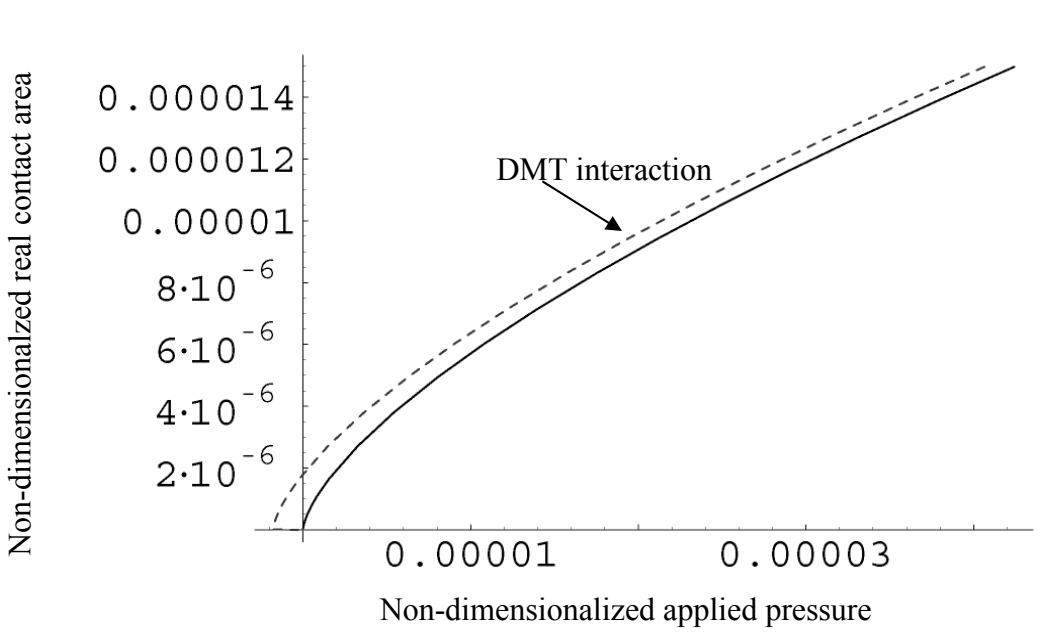

Figure 4.10. Non-dimensionalized real area of contact versus applied pressure.

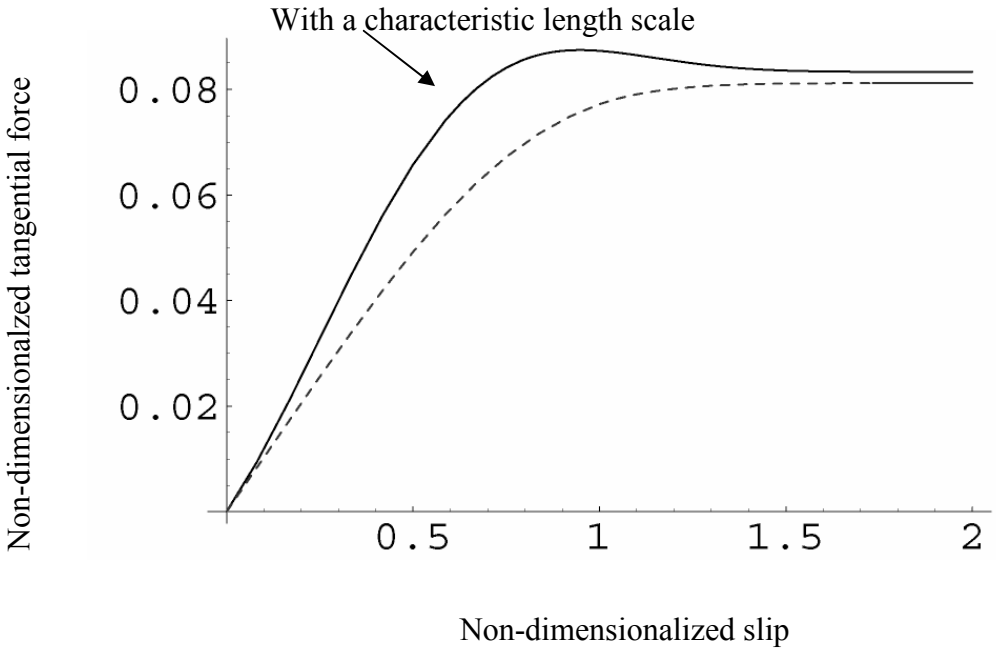

Figure 4.11. Non-dimesionalized tangential force versus slip.

5. Summary

We did not anticipate the discovery of the Pre-sliding Tangential Displacement (PSTD) phenomenon when this study began. This phenomenon cannot be described by a classical coefficient of friction, and for small nano-scale sliding distances Amontons' law does not apply. This is our most important finding. PSTD can determine the operation of some MEMS devices. For example, the operation of the nanotractor, with its 40 nm step size, cannot be predicted on the basis of measured static and dynamic friction coefficients. We have developed a simple 2-D model to help us understand the mechanics of PSTD. This model suggests that PSTD is a cascade of small-scale slips with a roughly constant number of contacts equilibrating the applied normal load. PSTD appears to depend not only on the specific spatial features of the contacting surfaces, but also on load level. We do not yet fully understand this phenomenon. It depends on the nature of the contacting surfaces (i.e., OTS-coated vs. FOTAS-coated), and there are indications of time-dependent behavior for OTS-coated materials.

We also had a number of other significant accomplishments during this three-year study. Below are listed some of these.

- Developed and used a nanotractor friction test device to measure static and dynamic MEMS-level friction data for a variety of SAM-coated polysilicon surfaces and also measured the effect of adhesion at low loads.

- Used the nanotractor to characterize the wear of polysilicon surfaces.

- Developed a routine method for ± 1 nm in-plane measurements.

- Developed a software scripting language (MEMScript) to enable automatic data logging and a wide range of actuation/measurement in MEMS.

- For the first time, measured single asperity-level data defining the resistance of SAM-coated silicon/silicon junctions to slip.

- Performed asperity-scale finite element simulations of friction using AFM-measured polysilicon surface topography and nano-scale adhesion and shear junction strengths inferred from AFM friction tests.

- Performed a detailed characterization of polysilicon topography and, for the first time, used this data as input to multi-asperity contact models. Revealed that roughening surfaces, while reducing total contact area moderately (good for stiction) increases the tendency toward damage dramatically (bad for friction).

- Developed grid-level models for friction in polysilicon micromachines.

Appendix A. Publications

1. R.W. Carpick, E.E. Flater, J.R. Van Langendon, and M.P. de Boer, *Friction in MEMS: From Single to Multiple Asperity Contact*. in *2002 SEM Annual Conference on Experimental Mechanics*. 2002. Milwaukee, WI.
2. A.D. Corwin and M.P. de Boer, *Effect of adhesion on dynamic and static friction in surface micromachining.* Applied Physics Letters, 2004. **84**: p. 2451-2453.
3. M.P. de Boer, D.L. Luck, J.A. Walraven, and J.M. Redmond, *Characterization of an inchworm actuator fabricated by polysilicon surface micromachining*. in *Reliability, Testing and Characterization of MEMS/MOEM*. 2001. San Francisco, CA.
4. M.P. de Boer, D.L. Luck, W.R. Ashurst, R. Maboudian, A.D. Corwin, J.A. Walraven, and J.M. Redmond, *High-Performance Surface-Micromachined Inchworm Actuator.* Journal of Microelectromechanical Systems, 2004. **13**: p. 63-74.
5. E.E. Flater, A.D. Corwin, M.P. de Boer, and R.W. Carpick, *In-situ wear studies of surface micromachined interfaces subject to controlled loading.* Wear, 2004.
6. R.E. Jones, *Models for Contact Loading and Unloading of Rough Surfaces.* International Journal of Engineering Science, 2003.
7. R.E. Jones and D. Zeigler, *A Method for Determining the Asperity Distribution of Contacting Rough Surface.* ASME Journal of Tribology, 2003.
8. R.E. Jones and D. Zeigler, *A Two-scale Treatment of Contact between Rough Surfaces.* Computer Methods in Applied Mechanics and Engineering, 2003.
9. D.L. Luck, M.P. de Boer, W.R. Ashurst, and M.S. Baker, *Evidence for pre-sliding tangential deflections in MEMS friction*. in *TRANSDUCERS'03, 12th International Conference on Solid-State Sensors and Actuators*. 2003. Boston, MA.
10. M.J. Starr, H. Sumali, J.M. Redmond, E.E. Flater, and R.W. Carpick, *Analysis of Contact Forces Using AFM Data of Polycrystalline Silicon Surfaces*. in *SEM X*. 2004. Costa Mesa, CA.

Appendix B. Analysis of a SAM-Coated Silicon Substrate by a Spherical-tipped Silicon Indenter

Consider the problem shown schematically in Figure B.1.

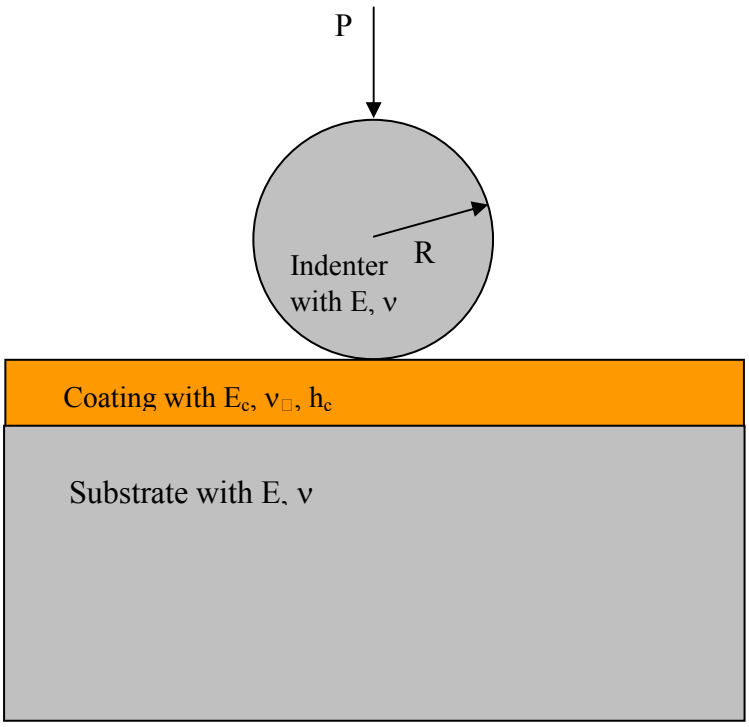

Fig. B.1. A spherical indenter-tip contacting a coated, semi-infinite substrate.

Based upon dimensional analysis considerations, the contact area will depend on variables *P, R, E, ν, E_c, ν_c*, and h_c in the following manner:

$$Area = \pi \left(\frac{3PR\left(1+\frac{\overline{E}}{\overline{E}_c}\right)}{4\overline{E}} \right)^{2/3} f\left(\frac{P}{\overline{E}_c h_c^2}, \frac{\overline{E}_c}{\overline{E}}, \frac{h_c}{R}, \nu, \nu_c\right) \qquad \text{(B.1)}$$

where $\overline{E} = E/(1-\nu^2)$ and $\overline{E}_c = E_c/(1-\nu_c^2)$.

Note that with this definition, the function *f* equals *1* when the nominal penetration distance is very small relative to the coating thickness (i.e., the substrate does not influence contact). When the penetration distance is large, the coating will have negligible affect on contact, and the function *f* will have the value $\left(2/\left(1+\overline{E}/\overline{E}_c\right)\right)^{2/3}$.

The finite element results indicate that for the range of penetration distances considered (maximum of 0.4 nm relative to the coating thickness of 2 nm generates a maximum nominal coating strain of 0.2) the function *f* can be approximated by a power law relationship with respect to the variable $P/\overline{E}_c h_c^2$.

$$f\left(\frac{P}{\overline{E}_c h_c^2}, \frac{\overline{E}_c}{\overline{E}}, \frac{h_c}{R}, \nu, \nu_c\right) = A\left(\frac{P}{\overline{E}_c h_c^2}\right)^b \tag{B.2}$$

Figure B.2 shows one example of a power-law fit for the function *f*.

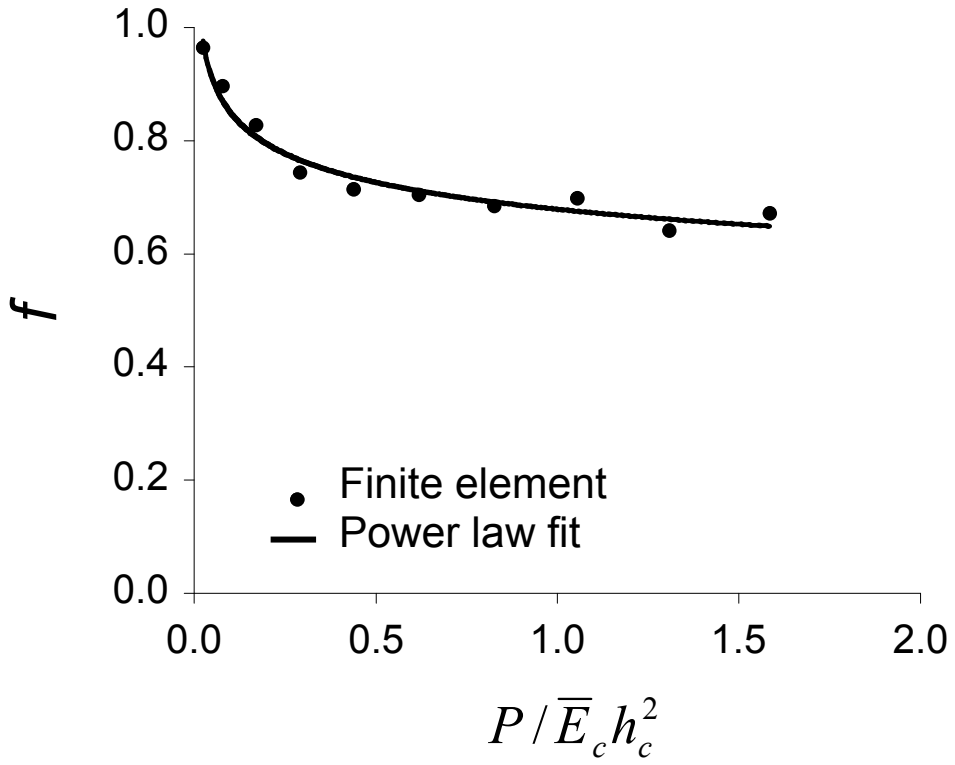

Fig. B.2. Function *f* as determined by a finite element analysis for *R=27 nm, E=161 GPa, ν= 0.23, E_c=8 GPa, ν_c=0.4*, and h_c= 2 nm and the associated power-law fit.

Table B.1 lists values of the parameters A and b, for the specified nondimensional parameters (Eq. B.2). Note that the maximum value of $P/\overline{E}_c h_c^2$ used in a data fit is also

indicated (care must be taken when extrapolating beyond this value). Also recall that as $P/\overline{E}_c h_c^2$ approaches zero, the function f approaches a value of 1. Consequently, the power-law fit is not valid when small $P/\overline{E}_c h_c^2$ generate f values greater than 1. When this occurs, f should be set equal to 1.

Table B.1. Values of the parameters A and b defining the power-law fit for the function f as determined from the finite element analysis.

Case	R (nm)	E_c (GPa)	$\overline{E}_c/\overline{E}$	h_c/R	ν	ν_c	Maximum $P/\overline{E}_c h_c^2$	A	b
1	27	8	0.0560	0.0741	0.23	0.40	1.59	0.679	-0.097
2	30	8	0.0560	0.0667	0.23	0.40	1.74	0.662	-0.084
3	35	8	0.0560	0.0571	0.23	0.40	1.97	0.643	-0.089
4	27	2	0.0140	0.0741	0.23	0.40	2.33	0.646	-0.109
5	27	4	0.0280	0.0741	0.23	0.40	2.01	0.656	-0.110
6	27	16	0.1120	0.0741	0.23	0.40	1.12	0.727	-0.078
7	27	16	0.0560	0.0741	0.23	0.40	1.59	0.667	-0.099

When there is no coating on the substrate, the Hertz solution predicts that contact area and contact load are related by a power-law with an exponent of 2/3. Note, however, that when there is a compliant coating on the substrate, a negative exponent b gives rise to a power law relationship between contact area and contact load that has an exponent that differs from 2/3 (Eqs. B.1 and B.2). The first 3 entries in Table 1 examine the affect of varying the indenter-tip radius. The variations in the A and b parameters are thought to be within the accuracy of the analysis. Note that the ~0.2-nm element in the contact region limits the precision for determining the contact radius (the maximum contact radius is typically ~ 4 nm). A reasonable common choice for the parameters for Cases 1-3 are A = 0.66 and b = –0.09. Cases 1, 4, 5, and 6 examine the effect of varying the modulus of the coating. It appears that there may be a modest increase in the parameter A and a modest decrease in the exponent b as $\overline{E}_c/\overline{E}$ increases.

Case 7's modulus values are twice those of Case 1, but the nondimensional parameter $\overline{E}_c/\overline{E}$ is unchanged. This calculation was performed to check the presumed nondimensional form of the function f. As anticipated, the A and b parameters are essentially the same (Eq. B.2).

Appendix C. AFM friction testing

AFM methodology

The Atomic Force Microscope (AFM) is a useful tool for understanding micro- to nano-scale features of a surface, as described in Section 4.1, as well as frictional properties at the nano-scale. The AFM consists of a flexible cantilever in contact with a sample. A laser beam is reflected from the backside of the cantilever beam and its relative motion is recorded using a position sensitive photodiode. In this manner the AFM is sensitive to normal and lateral displacements of the cantilever as it scans across the surface. An AFM cantilever can be scanned so that the direction of motion is perpendicular to the long axis of the cantilever. The lever twists due to the frictional resistance experienced by the tip, and the laser spot reflected from the back of the cantilever moves laterally on the photodetector. Friction is determined by taking half the difference of the forward and backward scans along a given line on the surface. Normally, in feedback control, the cantilever is scanned at a constant applied load. This load can then be varied in a controlled manner as described below. We refer to this type of experiment as determining friction as a function of load, or more simply "friction versus load".

Friction versus load curves can be obtained by the following procedure. First, the AFM system needs to be able to vary the applied load on the cantilever while simultaneously monitoring and recording the normal and lateral signals during scanning. We accomplished this by applying an external signal to the AFM via a breakout box to change the set-point value, or the applied normal load, in the feedback control. This method allows for feedback control while the load is varied during scanning, which permits for measurements on rough or sloped surfaces. Friction and load are continuously measured by monitoring the position of the laser reflection on the photodetector in the normal and lateral directions, respectively. A continuously varying voltage signal is applied, so it should be noted that the load continuously varies during the experiment, even during one scan line. To account for this, the load is varied slowly, and the load and friction variation on one line are averaged to obtain one data point of load and friction for each scan line. This is reasonable since the variation in voltage during one scan line is small compared to the range of voltages applied during the experiment. To monitor the reproducibility of the data the applied load is started at a high load, ramped down until pull-off occurs, and then increased back to the starting load. This way the same normal applied load is measured twice within a short span of time, for both increasing and decreasing load. If the data is the same in both cases the data has been reproduced. This can be checked by repeating the friction measurements at different locations on the sample surface to check for any variation.

For consistent friction results, friction versus load data was obtained on a small area (100 nm x 100 nm) to minimize the effects of possible sample topographic and chemical inhomogeneity. However, this scanned area is large enough to ensure that the AFM tip overcomes the static friction and actually slides across the surface, which is easily verified by confirming that the friction loops contain a steady-state sliding regime. When

analyzing the friction data, only the portion of the friction traces that corresponds to this steady state sliding situation should be considered, thereby excluding the static friction regimes.

Relation between contact area and friction

Several studies have shown that the friction force in solid-solid nanocontacts below the wear threshold is often proportional to the true contact area, *i.e.* the number of interfacial atoms [C.1-C.6]. This was demonstrated by measuring both friction and the nano-scale contact area experimentally. In other words, friction F_f for a single asperity contact is given by:

$$F_f = \tau^* A \tag{C.1}$$

where A is the interfacial contact area, and $\tau*$ is the interfacial shear strength. As it represents the friction force per unit area of a pair of materials, one can also consider τ^* as representing the intrinsic frictional dissipation per interfacial atom.

The shear strength is not necessarily constant, and may be more generally described as a constant plus a pressure-dependent term:

$$\tau^* = \tau_o^* + \alpha p \tag{C.2}$$

where p is the nominal contact pressure and α is a dimensionless coefficient. The magnitude and pressure dependence of the shear strength will depend on the materials and the sliding conditions (environment and temperature), and determining its behavior is a key goal in nanotribology – as is the determination of the general validity of Eq. (C.1), which may break down for sufficiently small contacts. Eq. (C.2) has been shown to apply very well to systems involving molecular films in contact in the SFA [C.7], for some soft solids in macroscopic contact [C.8], and for some systems measured with the AFM [C.9]. For bare solid interfaces, the majority of studies report that α is negligible [C.1-C.6, C.9-C.19], but the range of materials for which this has been tested is still somewhat limited.

Brief intro to molecular organic monolayers

Several different molecular precursors were used to create organic hydrophobic monolayer coatings for silicon MEMS surfaces. Their chemistry is briefly introduced here. Three different molecular films were used in these studies: octadecyltrichlorosilane (OTS, sometimes called ODTS), octadecene, and (tridecafluoro-1,1,2,2-tetrahydrodecyl)tris(dimethylamino)silane (FOTAS). Fig. C.1 gives the chemical structure of each of these molecules and how they might attach to either a SiO_2 or Si surface. As can be seen from Fig. C.1, the OTS and octadecene are similar molecules, except for their head groups that bind to the surface. This allows for distinct bonding mechanisms of this precursor to a substrate. The OTS molecule bonds to a silicon oxide surface via a Si-O bond, while the octadecene bonds to a silicon surface with a direct C-Si bond. This will influence their frictional properties, as will be discussed later. The

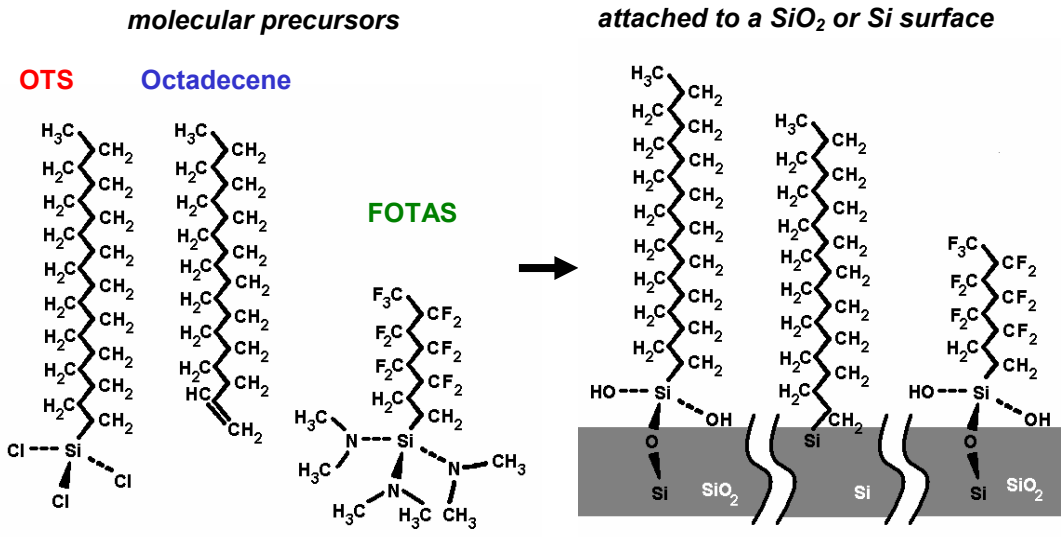

Fig. C.1. Chemical schematics of the molecular precursors and the most probable attachment of these molecules to their respective substrates.

FOTAS molecule is a much shorter chain, terminated in F instead of H. This also will influence its frictional and adhesive properties.

Uncoated tip experiments:

All AFM data shown in this report were taken using a Digital Instruments Nanoscope IV MultiMode AFM (Santa Barbara, CA). The sample was a silicon substrate coated with a thin organic film. The tip was either a commercial silicon tip with its native oxide termination, or the same type of tip coated with an organic monolayer, just like the substrates. This second case mimics the conditions of the MEMS interfaces, where both surfaces are coated with the SAM. The data were acquired according to the procedure outlined above, where a ramped voltage was applied to AFM electronics to continuously vary the set-point. Note that the normal load axis is defined such that zero corresponds to zero externally applied load. That is, a normal load of zero corresponds to the signal the lever possesses when out of contact with the sample, and no load is acting.

The first experiments were performed using a Si tip with its native oxide sliding on the OTS and octadecene monolayers. A representative set of data is shown in Fig. C.2. We obtain distinct types of behavior depending on the substrate during the friction versus load tests. The first obvious observation is that for the majority of the loads tested, the OTS has larger friction than the octadecene. We also see that the trends in the two sets of data are distinct: the octadecene data is fairly linear, at least at low loads, and the OTS is non-linear. We can discover several things by fitting this data using a contact mechanics model that takes into account a range of possible surface adhesion and material deformation behaviors. (For more details on this, refer to [C.1].) As a preliminary step, we fit the data assuming that the material is completely homogeneous (*i.e.* ignoring the monolayer coating). Fitting using Eqs. (C.1) and (C.2) we find that OTS has a constant

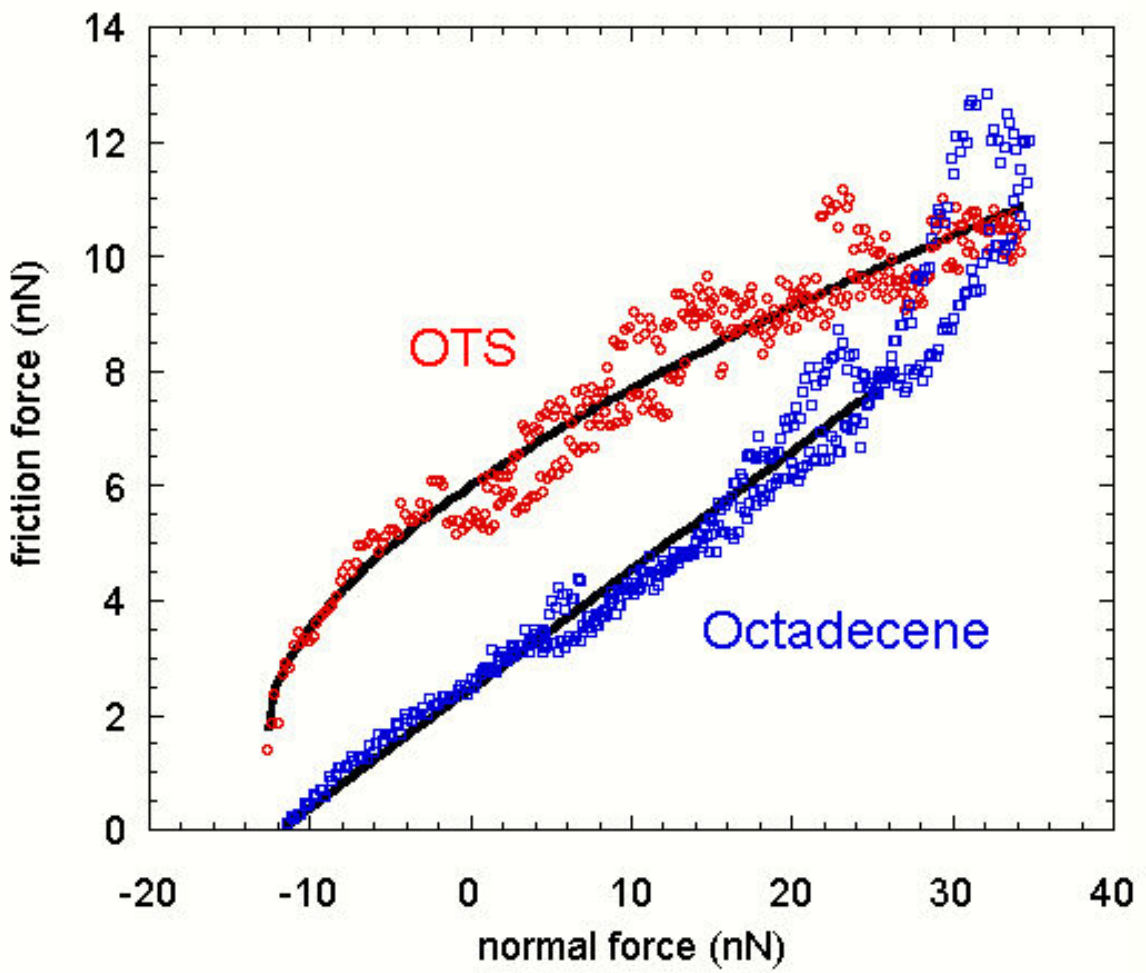

Fig. C.2. Comparison of friction versus load curves for a silicon tip sliding on OTS and octadecene.

shear strength and octadecene has a pressure dependent shear strength. So even though OTS has higher friction at the nanoscale up to approximately 25 nN,(corresponding to approximately 2 GPa of normal contact pressure), we find that at higher loads the octadecene appears to have higher friction. Certainly, extrapolating the trend would show friction for octadecene continuing to increase beyond OTS. This allows us to account for the trend in behavior at the microscale with the nanotractor, where octadecene has higher friction than the OTS (see Fig. 2.7).

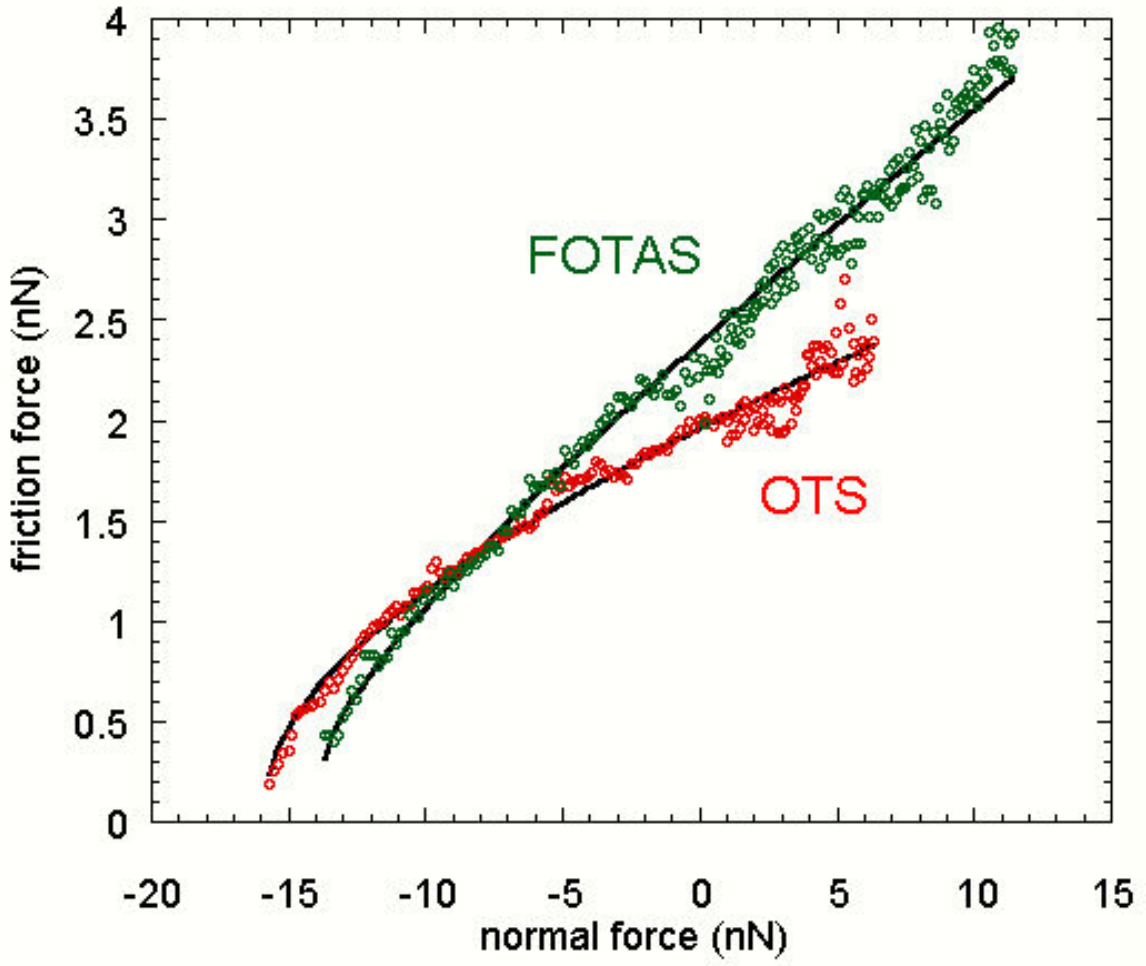

Fig. C.3. Comparison of the frictional properties of OTS and FOTAS under a silicon AFM tip.

A comparison was also made between the FOTAS and OTS monolayer by scanning both of these materials with the same uncoated silicon tip. As seen in Fig. C.3, the OTS monolayer displays similar behavior as in Fig. C.2, where OTS can be found to have a constant shear strength. One may note that the absolute values of friction and pull-off force (and the resultant shear strength and adhesion energy) are different for the OTS on Figs.C.2 and C.3. Variability from day to day and from tip to tip was often seen for the OTS experiments, and may be attributed to variable tip chemistry due to the hydrophilic nature of a silicon tip terminated with its native oxide. The FOTAS frictional properties are seen to be similar to those of octadecene, in that the shear strength has a pressure dependence.

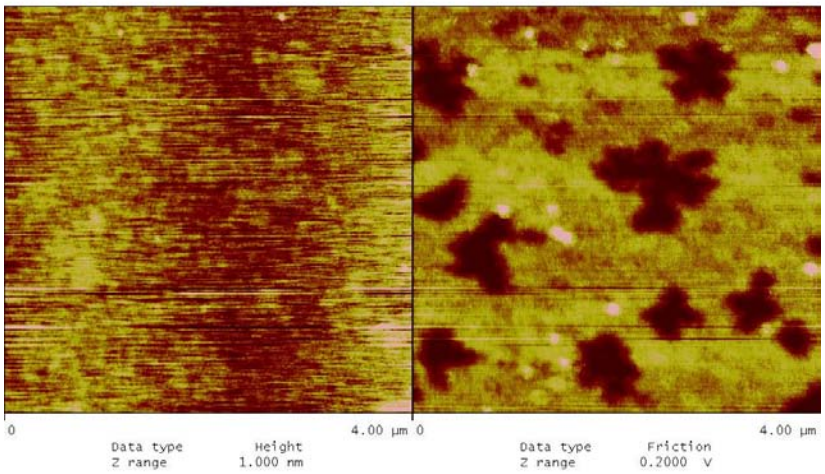

Fig C.4. AFM images of topography (left) and friction (right) that show the different phases present in an OTS-coated silicon surface. Light colors indication high values of height or friction, and dark colors indicate low values.

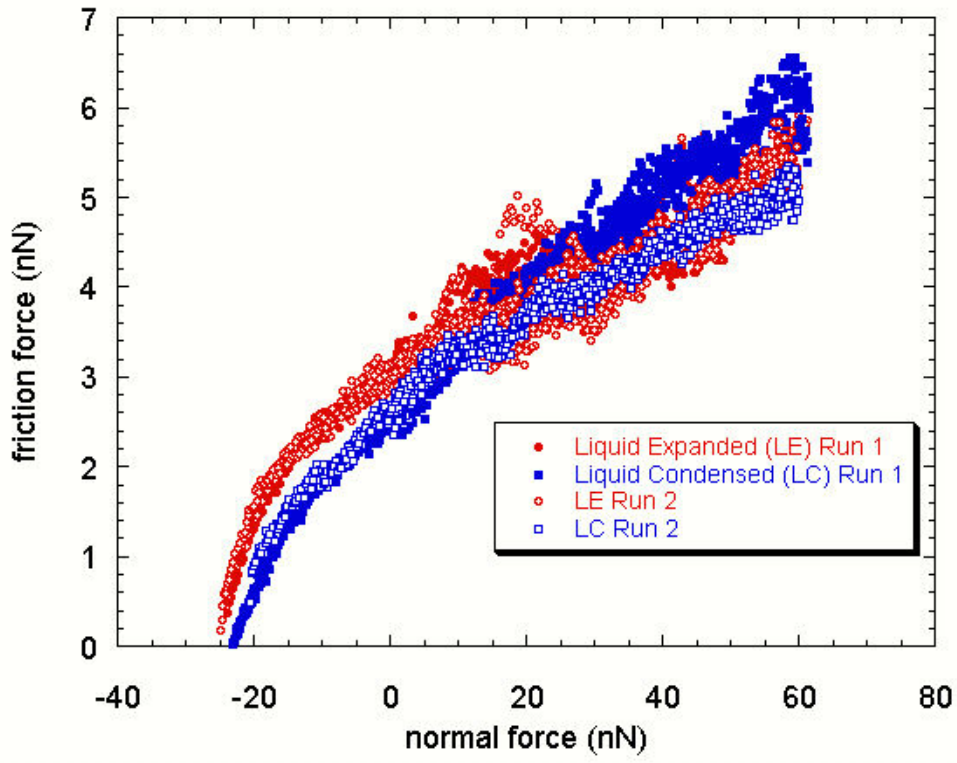

Fig. C.5. Friction versus load experiments on the LC and LE phases of the OTS monolayer. Two runs are shown for each phase, which indicate tests performed on the same phase in different locations. The LE and LC friction versus load plots overlap at the high loads, but separate at the low loads, indicating different deformation or frictional mechanisms in this load regime.

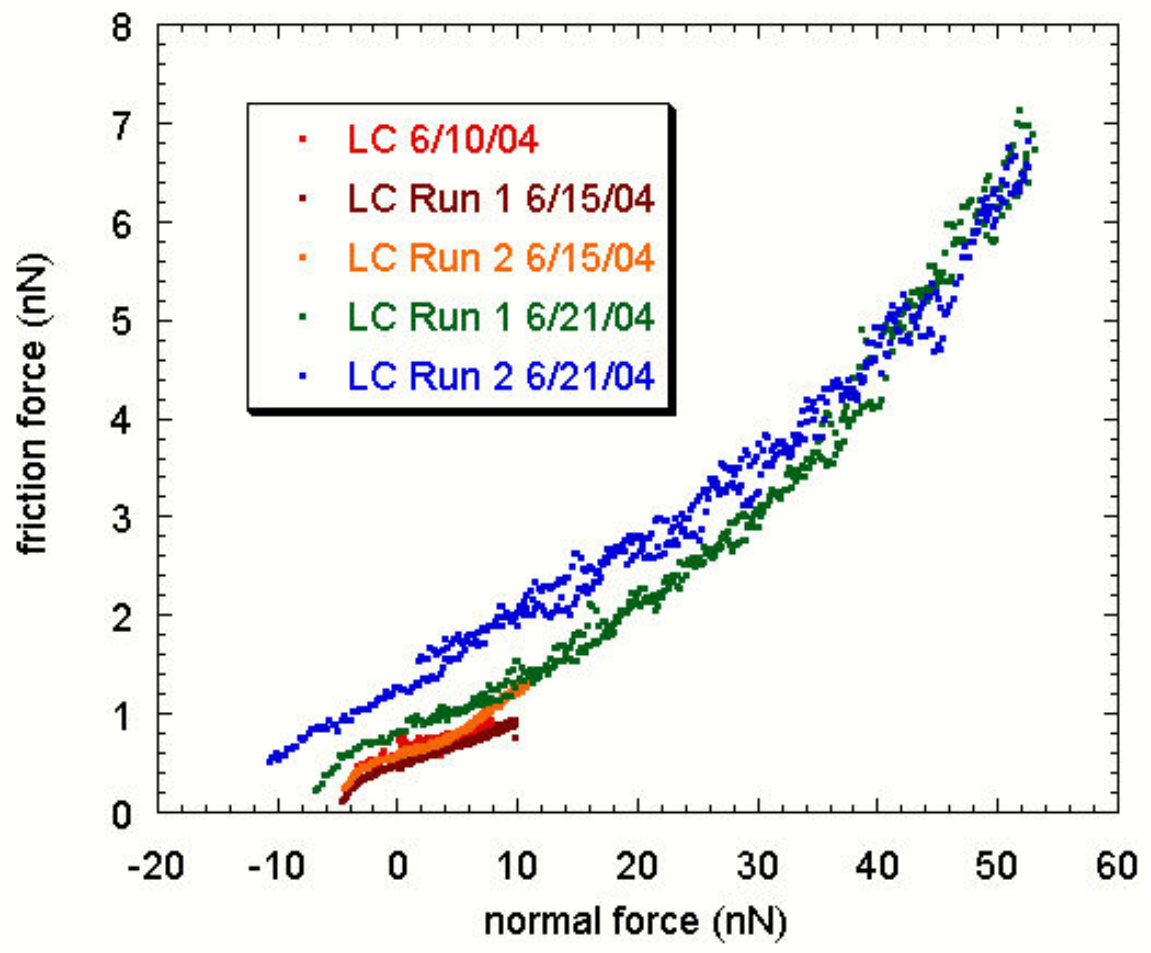

Fig. C.6. Comparison of friction versus load experiments using a single OTS-coated Si tip sliding on OTS-coated Si substrate. The data show good consistency for the first three trials, but friction tends to increase with time, suggesting progressive damage of the tip monolayer.

It has been seen previously that the OTS film exhibits different phases on the silicon surface, as shown in Fig. C.4. The kinetics of these phases has been determined previously [C.20]. The two phases observed on our samples include a well-packed phase, called the Liquid Condensed (LC) phase, and less ordered phase, the Liquid Expanded (LE) phase. These phases are evident when an AFM image is taken of the surfaces, simultaneously recording topography and friction, as in Fig. C.4. The LC phase appears on the surface as flower patterns in both images, where these phases are slightly raised above the other phase (~0.2-0.5 nm higher) and have lower friction. This phenomenon was studied more in detail by performing friction versus load experiments on each phases separately. This result is shown in Fig C.5. Two runs were performed for each phase in different locations, but the data is consistent between runs on the same monolayer. In

addition, the LE and LC friction versus load plots overlap at the high loads, but separate at the low loads, indicating different deformation or frictional mechanisms in this load regime.

Coated tip experiments

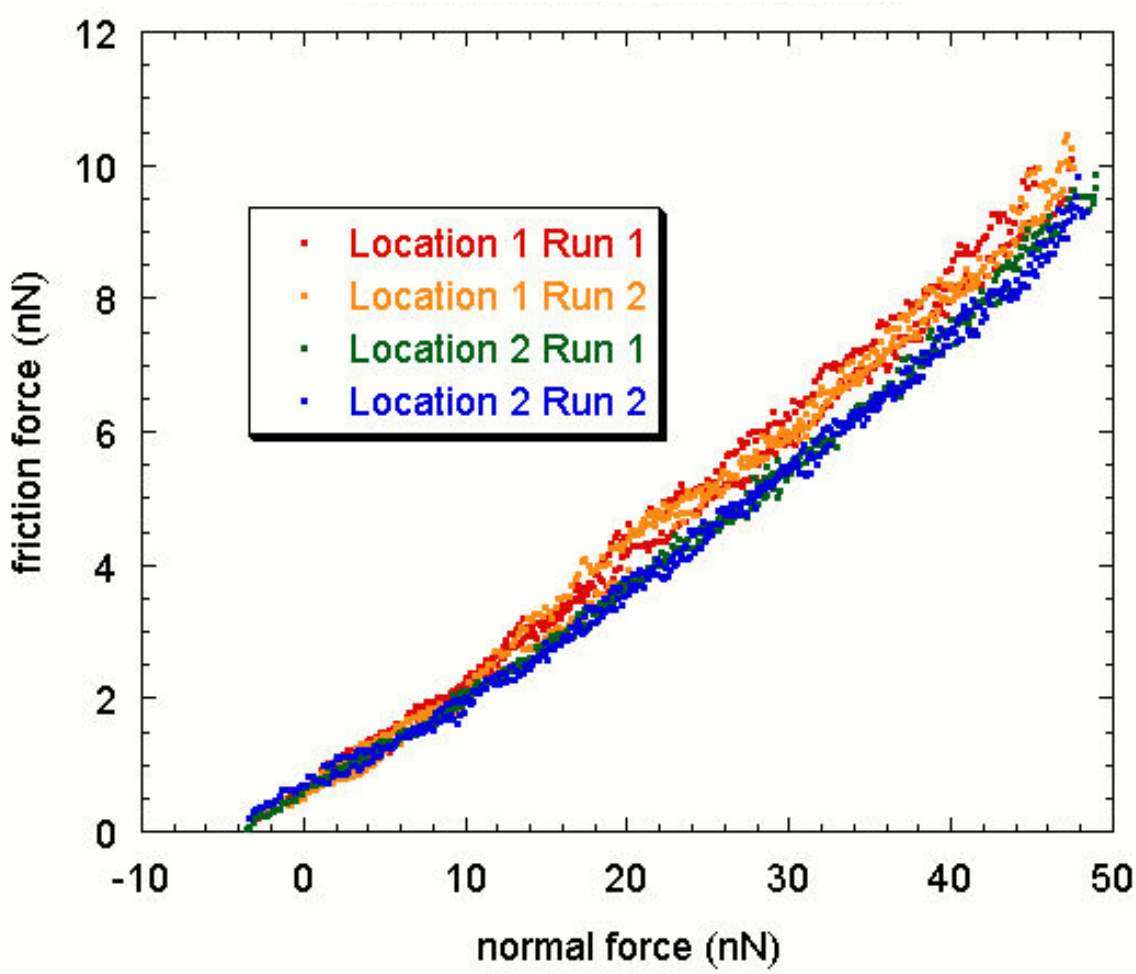

Fig. C.7 shows data for FOTAS-on-FOTAS. This data is quite linear, and is quite consistent from run to run and location-to-location on this experiment date, except for a slight overall decrease in friction, which may be due to run-in effects.

Silicon AFM tips were also coated with the molecular coatings using an identical process as for coating the flat silicon substrates. This allows us to better understand the MEMS interface of the nanotractor, since both surfaces are coated with the hydrophobic molecules. A study of OTS sliding on OTS is shown in Fig.C.6. We see that the appearance of these friction versus load curves are much more linear compared to the Si-on-OTS curves shown in Figs. C.2 and C.3. Even in some cases, (*e.g.* the orange curve) there even appear to be multiple linear regions of behavior. Also at higher loads there tends to be a turning up of the curves, possibly indicating a stiffening behavior of the

molecules. The data show good consistency for the first three trials, but friction tends to increase with time, suggesting progressive damage of the tip monolayer. This frictional interface has shown increased reproducibility compared to the Si-on-OTS interface. We believe this is due to the better-controlled interface created by the molecular surface layers. This is an important point that may have impact throughout the entire nanotribology community: measurements of friction with the AFM may be irreproducible as the norm, not the exception, unless the tip is treated to be chemically inert.

Coated vs Uncoated

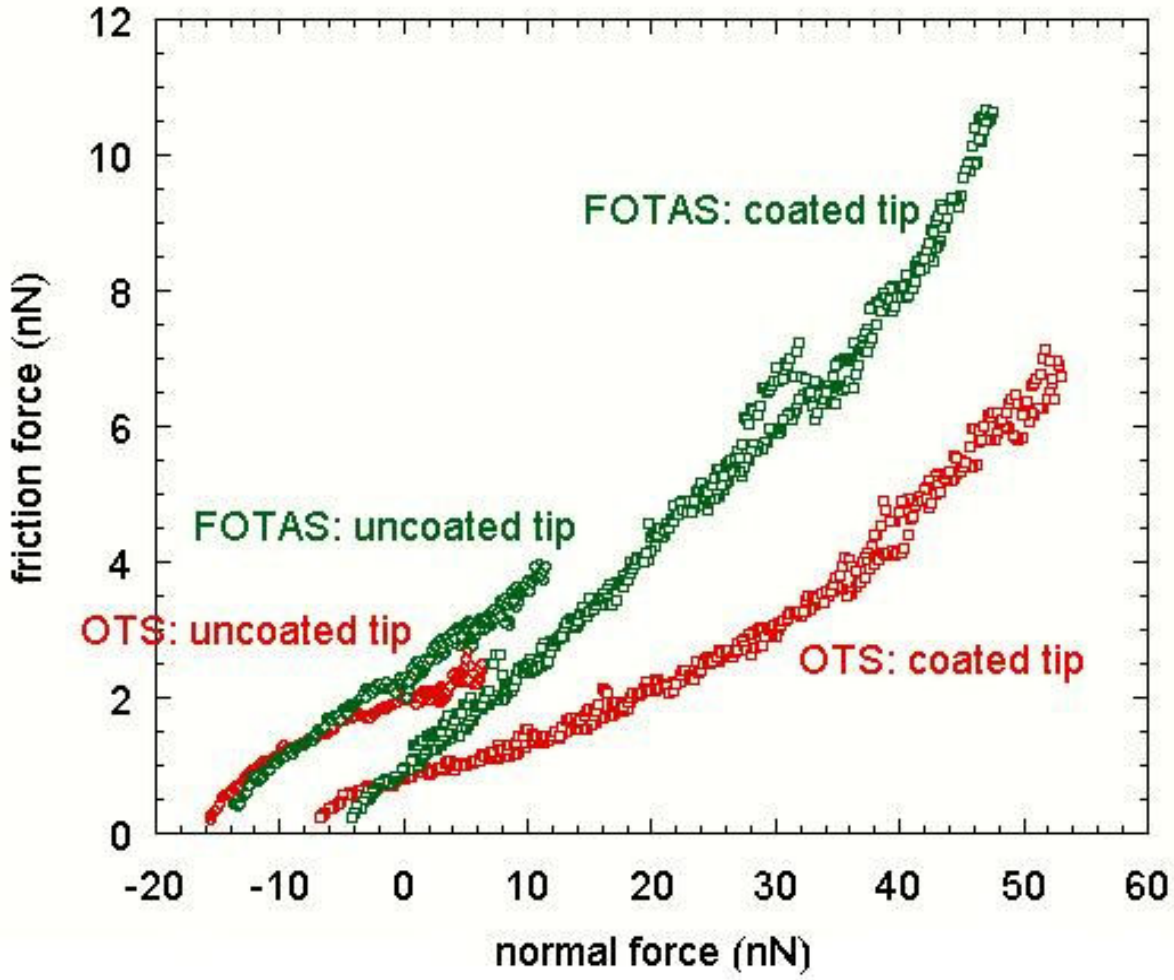

Fig. C.8. Comparison of experiments using coated and uncoated silicon tips, as indicated on the plot.

If we compare data between the friction versus load experiment performed using an uncoated silicon tip and performed using a monolayer-coated silicon tip, there are several observations (Fig. C.8.). First we see that for the loading from initial contact up to around

10 nN for these tips, friction is reduced by using a monolayer-on-monolayer tribopair as compared with silicon-on-monolayer. This is expected due to the hydrophilic and friction-reducing nature of these films. We also see that the trends between the different types of monolayer are similar. For instance, measuring friction with the uncoated tip shows a crossover of the behavior at around –8nN, where likewise there is a crossover point for the coated tip experiments at around –2nN. This is apparently due to the pressure-dependent nature of shear strength for the FOTAS interface, which allows for much lower friction at lower loads, with a steeper increase in friction with load.

Preliminary conclusions from these initial studies are as follows:

- Chemical modification of uncoated AFM tips greatly modifies the frictional response.
- It is critical to check for reproducibility of AFM friction measurements.
- Coating tips with SAMs enhances the stability of AFM tips for friction measurements, although slow degradation of the monolayer on the tip occurs and leads to increases in friction with time.
- It is critical to determine the pressure-dependence of both the contact area and the shear strength of the interface to unravel what determines friction, and to be able to apply the results over wide pressure ranges.
- OTS exhibits a pressure-independent shear strength, while FOTAS and octadecene exhibit pressure-dependent responses. This leads to the result that OTS exhibits higher friction than octadecene and FOTAS only at low loads; at high loads, the pressure-dependent shear strength causes friction for FOTAS and octadecene to increase more rapidly with load.
- The pressure-dependent responses may be due to the different packing densities and short-range order in the film. OTS may be the densest phase. Compared with FOTAS, it has a smaller lateral van der Waals radius of its methylene chains, and its backbone is more linear. Compared with octadecene, the film may be denser and more uniform because OTS has some mobility as it is deposited on the substrate, whereas the octadecene will tend to react directly with the silicon and stay in place, thus preventing the film to re-organize to increase its density. Although these statements are speculative, this work points toward future experiments that can unravel the many contributions to friction at the nanoscale for monolayer films, which is a critical aspect to a wide range of nanoscience and nanotechnology applications.

REFERENCES

C.1. Carpick, R.W. and M. Salmeron, *Scratching the surface: Fundamental investigations of tribology with atomic force microscopy.* Chemical Reviews, 1997. **97**(4): p. 1163-1194.

C.2. Carpick, R.W., et al., *Measurement of interfacial shear (friction) with an ultrahigh vacuum atomic force microscope.* Journal of Vacuum Science & Technology B, 1996. **14**(2): p. 1289-1295.

C.3. Carpick, R.W., et al., *Variation of the interfacial shear strength and adhesion of a nanometer-sized contact.* Langmuir, 1996. **12**(13): p. 3334-3340.

C.4. Carpick, R.W., D.F. Ogletree, and M. Salmeron, *Lateral stiffness: A new nanomechanical measurement with friction force microscopy.* Applied Physics Letters, 1997. **70**(12): p. 1548-1550.

C.5. Carpick, R.W., et al., *Making, breaking, and sliding of nanometer-scale contacts*, in *Fracture and Ductile vs. Brittle Behavior - Theory, Modeling and Experiment.*, G. Beltz, K.-S. Kim, and R.L. Selinger, Editors. 1999, Mater. Res. Soc.: Warrendale, PA, USA. p. 93-103.

C.6. Enachescu, M., et al., *Observation of proportionality between friction and contact area at the nanometer scale.* Tribology Letters, 1999. **7**(2-3): p. 73-78.

C.7. Briscoe, B.J. and D.C.B. Evans, *The shear properties of Langmuir-Blodgett Layers.* Proc. Roy. Soc. Lond. A, 1982. **380**(1779): p. 389-407.

C.8. Singer, I.L., et al., *Hertzian stress contribution to low friction behavior of thin MoS_2 coatings.* Applied Physics Letters, 1990. **57**(10): p. 995.

C.9. Pietrement, O. and M. Troyon, *Study of the interfacial shear strength on carbon fibers surface at the nanometer scale.* Surface Science, 2001. **490**(1-2): p. L592-6.

C.10. Lantz, M.A., et al., *Atomic-force-microscope study of contact area and friction on $NbSe_2$.* Physical Review B (Condensed Matter), 1997. **55**(16): p. 10776-85.

C.11. Johnson, K.L., *Adhesion and friction between a smooth elastic asperity and a plane surface.* Proc. Roy. Soc. Lond. A, 1997. **453**(1956): p. 163.

C.12. Pietrement, O. and M. Troyon, *Study of the interfacial shear strength pressure dependence by modulated lateral force microscopy.* Langmuir, 2001. **17**(21): p. 6540-6.

C.13. Burns, A.R., et al., *Molecular level friction as revealed with a novel scanning probe.* Langmuir, 1999. **15**(8): p. 2922-2930.

C.14. Burns, A.R., et al., *Friction and molecular deformation in the tensile regime.* Physical Review Letters, 1999. **82**(6): p. 1181.

C.15. Enachescu, M., et al., *An AFM study of an ideally hard contact: The diamond(111)/tungsten-carbide interface.* Physical Review Letters, 1998. **81**(9): p. 1877-1880.

C.16. Lüthi, R., et al., *Friction on the atomic scale: an ultrahigh vacuum atomic force microscopy study on ionic crystals.* Journal of Vacuum Science & Technology B, 1996. **14**(2): p. 1280.

C.17. Lantz, M.A., et al., *Lateral stiffness of the tip and tip-sample contact in frictional force microscopy.* Applied Physics Letters, 1997. **70**(8): p. 970-972.

C.18. Wei, Z., C. Wang, and C. Bai, *Investigation of nanoscale frictional contact by friction force microscopy.* Langmuir, 2001. **17**(13): p. 3945-51.

C.19. Singer, I.L. and H.M. Pollock, eds. *Fundamentals of Friction: Macroscopic and Microscopic Processes*. NATO ASI Series. 1992, Kluwer: Dordrecht.
C.20. Carraro, C., et al., *Observation of three growth mechanisms in self-assembled monolayers.* Journal of Physical Chemistry B, 1998. **102**(23): p. 4441.

Acknowledgements.

We would like to acknowledge the contributions of David L. Luck (Dept. 1769, MEMS Device Technologies), whose work in partial fulfillment of his Master's Thesis at the University of Colorado at Boulder, is described in Section 2.1.7.

This study was funded by the Sandia's Laboratory Research and Development (LDRD) program. Sandia is a multiprogram laboratory operated by Sandia Corporation, a Lockheed Martin Company, for the United States Department of Energy's National Nuclear Security Administration under Contract DE-AC04-94AL85000.

Distribution:

1	MS 0123	C. L. Chavez, LDRD office, 1011
1	MS 0824	W. L. Hermina, 9110
1	MS 0826	S. N. Kempka, 9113
1	MS 0835	K. F Alvin, 9142
1	MS 0847	P. J. Wilson, 9120
5	MS 0847	J. M. Redmond, 9124
5	MS 0847	F. Bitsie, 9124
5	MS 0847	M. J. Starr, 9124
1	MS 0893	P. Chaplya, 9123
1	MS 0893	J. V. Cox, 9123
1	MS 0893	D. Hammerand, 9123
1	MS 0893	C. A. Lavin, 9123
1	MS 0893	M. K. Neilsen, 9123
1	MS 0893	J. Pott, 9123
10	MS 0893	E. D. Reedy, Jr., 9123
1	MS 0893	Day file, 9123
1	MS 0889	J. S. Custer, 1851
1	MS 0889	M. T. Dugger, 1851
1	MS 0889	S. V. Prasad, 1851
2	MS 0899	Technical Library, 9616
1	MS 1080	D. R. Sandison, 1762
1	MS 1080	D. L. Luck, 1762
1	MS 1080	H. D. Stewart, 1749
5	MS 1310	M. P. de Boer, 1762
5	MS 1310	A. D. Corwin, 1762
1	MS 1411	M. J. Stevens, 1834
1	MS 1411	M. E. Chandross, 1834
1	MS 1415	J. E. Houston, 1114
1	MS 1415	G. S. Grest, 1114
1	MS 1415	J. C. Barbour, 1110
1	MS 1415	N. D. Shinn, 1114
1	MS 1415	D. E. Peebles, 1112
1	MS 1413	T. A. Michalske, 1040
1	MS 1427	J. M. Phillips, 1100
1	MS 9018	Central Technical Files, 8945-1
1	MS 9161	E-P Chen, 8763
1	MS 9161	P. A. Klein, 8763
1	MS 9409	J. R. Garcia, 8754
5	MS 9405	R. E. Jones, 8763
5	MS 9042	B. R. Antoun, 8754
1	MS 9409	N. R. Moody, 8754

1 G. Subhash
Mechanical Engineering - Engineering Mechanics Department
Michigan Technological Institute
Houghton, MI 49931

1 R. W. Carpick
University of Wisconsin
543 Engineering Research Building
1500 Engineering Drive
Madison, WI 53706-1687

1 E. E. Flater
University of Wisconsin
543 Engineering Research Building
1500 Engineering Drive
Madison, WI 53706-1687

1 M. D. Street
University of Wisconsin
543 Engineering Research Building
1500 Engineering Drive
Madison, WI 53706-1687

1 W. R. Ashurst
Auburn University
248 Ross Hall
Auburn, AL 36849

1 Professor Kenneth Liechti
University of Texas at Austin
Aerospace Engineering & Engineering Mechanics
210 E. 24th Street, WRW 110C
1 University Station C0600
Austin, TX 78712-0235